Activity-based automatic ROI generation (AARG) analysis of dendritic spine calcium transients reveals distance-dependent activity of voltage-gated calcium channels

Dissertation

for the award of the degree

“Doctor of Philosophy”

Division of Mathematics and Natural Sciences

of the Georg-August-Universität Göttingen

within the doctoral program:

Molecular Physiology of the Brain

of the Georg-August University School of Science

(GAUSS)

submitted by

Charlie Jonathan Gilbride

from Sheffield, England

Thesis Committee

Dr. Camin Dean	European Neuroscience Institute, Göttingen
Prof. Dr. Dr. Detlev Schild	Institute of Neurophysiology and Cellular Biophysics University Medical Centre, Göttingen
Dr. Oliver Schlüter	European Neuroscience Institute, Göttingen
Dr. Jeongseop Rhee	Max Planck Institute for Experimental Medicine, Göttingen

Members of the Examination Board

Dr. Camin Dean	European Neuroscience Institute, Göttingen
Prof. Dr. Dr. Detlev Schild	Institute of Neurophysiology and Cellular Biophysics University Medical Centre, Göttingen

Further members of the Examination Board

Dr. Jeongseop Rhee	Max Planck Institute for Experimental Medicine
Prof. Dr. Michael Hörner	European Neuroscience Institute, Göttingen
Prof. Dr. Thomas Dresbach	Department of Anatomy and Embryology University Medical Centre, Göttingen

Declaration

I confirm that the doctoral thesis entitled: “Activity-based automatic ROI generation (AARG) analysis of dendritic spine calcium transients reveals distance-dependent activity of voltage-gated calcium channels” is my own and I have relied on no other sources other than those specified.

Göttingen 29.11.2017

Charlie J Gilbride

Table of Contents

Abstract

Imaging synaptic activity in the form of calcium transients occurring in dendritic spines is advancing our understanding of nerve cell function beyond what can be achieved using electrophysiological methods alone. I have developed an analytical approach (which I name Activity-based Automatic Region of interest Generation (AARG) analysis) that facilitates the analysis of synaptic events simultaneously imaged across many dendritic spines. The approach automatically assigns regions of interest (ROIs) based on patterns of compartmentalized calcium transients in spines and generally emphasizes automation such that minimal user input is required. I demonstrate two ways in which this analysis can be applied to relevant questions in neuroscience. First, neurons are exposed to a recombinant neurotrophic compound – brain-derived neurotrophic factor (BDNF) – and then spontaneous spine calcium transients (SSCTs) are collected by washing magnesium out of the bath solution. Imaging SSCTs is required by AARG to automatically assign ROIs. With this approach, the effect of BDNF (or other compounds known to act on dendritic spines) can be analysed. Second, I have assessed the contribution of different voltage-gated calcium channels to SSCTs with a range of pharmacological agents. I find that specific blockers for channels mediating R-type and T-type currents contribute differently to SSCT depending upon distance of the current branch from the soma. These findings fit into an emerging picture of ion channel expression across the dendritic tree that appears well suited to support non-linear membrane potential fluctuations in dendrites. In addition to these imaging studies I have attempted to induce potentiation between pairs of synaptically connected neurons in dissociated hippocampal neurons. I was not able to induce stable potentiation under these conditions. Given the favourable experimental design I implemented (e.g. using perforated patch-clamp experiments) and based on a sound understanding of the relevant literature, signs of stable potentiation should have been more apparent. After thorough re-appraisal of the literature, I conclude that stable potentiation may require a more substantial input cooperativity than I initially envisaged.

Introduction

(1.1) Neuronal synapses

(1.1.1) Fundamental properties of neurons

The mature human central nervous system (CNS) is composed of billions of neurons that form trillions of chemical synapses (Pakkenberg *et al.*, 2003). Transmission of electrical signals along neuronal processes and between neurons across these synapses enables the CNS to carry out basic functions as well as support more complex tasks involving learning and memory. Despite being involved in a diverse range of functions and exhibiting a vast range of morphologies, neurons share some basic structural features and functional characteristics.

At neuronal plasma membranes, sodium/potassium ATPases actively pump three sodium ions out of the cytosol in exchange for two potassium ions from the extracellular space against their concentration gradients (Clausen *et al.*, 2017). This activity is essential in generating the resting membrane potential between -40 to -95mV (Hille, 2001). Also, all neurons are electrically excitable using the electrochemical gradient established by active transport of sodium and potassium ions to propagate sharp, all-or-none depolarizations – known as action potentials or somatic spikes – along the cell's axon (Hille, 2001). The axon of the mammalian CNS is a thin process extending from the base of the soma towards its target.

A single spike is composed of an inward sodium conductance in the rising phase and an outward potassium conductance in the falling phase (Hille, 2001). Voltage-gated sodium channels (VGSCs) mediate the sodium conductance with many of these channels opening at the spiking threshold (~-50mV for CA1 pyramidal neurons; Bean, 2007). These channels are highly expressed at the axon initial segment and at the nodes of Ranvier, which facilitates spike initiation and propagation along the axonal membrane (Hille, 2001; Bean, 2007; Vacher *et al.*, 2008). After 0mV, VGSCs begin to inactivate and require the membrane potential to repolarize for many milliseconds before they can once again allow sodium ions to pass (Hille, 2001; Bean, 2007). While VGSCs are highly expressed at nodes of Ranvier along myelinated axons, voltage-gated potassium channels are clustered in the juxtaparanodal zones near the axon-glia junctions (Rasband & Shrager, 2000). These properties make neuronal spikes fast, large and discrete membrane potential fluctuations as they propagate along the axon from their initiation point at the axon initial segment to the axon terminals.

(1.1.2) The axon terminal

At the axon terminal, neurotransmitters are loaded into synaptic vesicles (SVs). Glutamate is the principle neurotransmitter loaded into SVs at excitatory neurons of the CNS, while CNS inhibitory neurons load SVs with gamma-aminobutyric acid (GABA). SVs fall into three pools (reserve, recycling and readily-releasable) depending on the strength of stimulation required to trigger fusion of the vesicular and presynaptic membranes (Chamberland & Tóth, 2016). This fusion is controlled by a cycle of association and dissociation between SNARE proteins ("**s**oluble **N**SF **a**ttachment **re**ceptor proteins") and SM proteins ("**S**ec1/**M**unc18-like proteins").

Prior to fusion, a protein complex forms between vesicular (synaptobrevin/VAMP) and plasma membrane (syntaxin-1 and SNAP25) SNAREs (Dulubova *et al.*, 1999; Südhof, 2013). This step requires the participation of SM proteins (such as the neuronal SM protein, Munc18-1) and brings the SV in close proximity to the plasma membrane (Südhof, 2013). This brings the vesicle into a primed state. At this point, the vesicle is situated close to presynaptic voltage-gated calcium channels (VGCCs). Upon opening of VGCCs, local intracellular calcium concentrations increase and calcium binds to synaptotagmin-1, which triggers fusion pore opening (Südhof, 2013). Once fusion has taken place, SNARE/SM complexes disassemble and are recycled for further use (Südhof & Rothman, 2009).

Action potential depolarization opens presynaptic VGCCs leading to fast, calcium-dependent SV fusion. However, SV fusion can also proceed independently of action potential activity and it is likely that distinct pools of vesicles exist within the terminal that are susceptible to either spike-triggered release or spontaneous release (Truckenbrodt & Rizzoli, 2014; Chamberland & Tóth, 2016). At excitatory synapses, SVs fuse with the presynaptic plasma membrane to release glutamate into the synaptic cleft, which binds to glutamate-gated receptors on the postsynaptic membrane.

(1.1.3) The postsynaptic membrane

The postsynaptic membrane of a mature synapse contains a postsynaptic density (PSD)-95 protein. PSD-95 is stabilized at the postsynaptic membrane (Sturgill *et al.*, 2009) and anchors α-amino-3-hydroxy-5-methyl-4-isoxazolepropionic acid receptors (AMPARs), kainate receptors and N-methyl-D-aspartate receptors (NMDARs), among other synaptic proteins at the postsynaptic membrane (Kim & Sheng, 2004). In general, AMPARs are permeable to monovalent cations (sodium and potassium) while NMDARs are also permeable to calcium ions (Dingledine *et al.*, 1999; Hille, 2001) with electrochemical gradients favouring movement of sodium ions into the cell upon channel opening (Hille, 2001). Both AMPARs and NMDARs form as a tetrameric complex of

subunits (Laube *et al.* 1998; Traynelis *et al.*, 2010). AMPARs have four subunits (GluA1-GluA4) (Traynelis *et al.*, 2010) and are expressed predominantly as GluA1-GluA2 tetramers in the adult brain (Isaac *et al.*, 2007; Traynelis *et al.*, 2010). Assembly of functional NMDARs requires two GluN1 subunits with two GluN2 subunits or a combination of GluN2 and GluN3 subunits. GluN2 subunits have four isoforms (GluN2A-GluN2D) while there are two isoforms for GluN3 (GluN3A, GluN3B) (Traynelis *et al.*, 2010; Lohmann & Kessel, 2014).

As the main glutamate-sensitive ionotropic receptors of the synapse, NMDARs and AMPARs are critical for the induction of synaptic plasticity. A crucial feature of NMDARs, in addition to their calcium permeability, is their voltage-dependent block by magnesium (Jahr & Stevens, 1990) and slow deactivation kinetics (Cull-Candy *et al.*, 2001). These properties have led to the widely held view that NMDARs act as coincidence detectors because activation of NMDARs by glutamate must happen concomitantly with depolarization that is strong enough to relieve magnesium block of the pore (Collingridge, 1987; Bliss & Collingridge, 1993; Tabone & Ramaswami, 2012; Volianskis *et al.*, 2015). Influx of calcium through NMDAR pores is widely acknowledged to be the critical early step in NMDAR-dependent LTP induction (Perkel *et al.*, 1993; Sjöström *et al.*, 2008; Volianskis *et al.*, 2015).

Postsynaptic density protein (PSD)-95 is the best characterized PDZ domain protein and is important for organizing postsynaptic proteins (including AMPARs and NMDARs) and making AMPAR subunits available for phosphorylation – in particular, the GluA1 subunit is phosphorylated after LTP induction (Lee *et al.*, 2000), which is thought to be an important step in stabilizing LTP (Lee *et al.*, 2010). AMPARs also bind to transmembrane AMPA regulatory proteins (TARPs). TARPs, such as stargazin, through their interaction with AMPAR subunits and other postsynaptic proteins, control the lateral diffusion of AMPARs between the synapse and the extrasynaptic compartment (Bats *et al.*, 2007; Constals *et al.*, 2015). Trafficking of AMPARs between synaptic and extrasynaptic sites is thought to be an important mechanism through which changes in synaptic strength are expressed (Lohmann & Kessels, 2014).

(1.1.4) Dendritic spines

Postsynaptic compartments on most principal neurons are usually located on dendritic membrane protrusions called spines (Nishiyama & Yasuda, 2015). These structures contain postsynaptic protein assemblies and exist in several distinct morphological classes (Bourne & Harris, 2008; Chen & Sabatini, 2012). Spine heads have diameters at or below the diffraction limit of light, which has always made analysis of spine images taken using conventional light microscopy techniques somewhat prone to error and misclassification. Tønnesen *et al.* (2014) used super-resolution

microscopy to accurately measure spine head and neck parameters. Their results suggest that almost all spines have necks that help to electrochemically compartmentalize the spine head. Diffusional coupling between the spine head and parent dendrite has been measured using fluorescence recovery after photobleaching (FRAP) experiments, which suggest that spines are biochemically compartmentalized (Svoboda *et al.*, 1996; Bloodgood & Sabatini, 2005). Sabatini *et al.* (2002) used optical fluctuation analysis to show that this biochemical compartmentalization extends to calcium as well as larger fluorescent molecules. Indeed, calcium is expelled from the spine through membrane-bound ion exchangers before calcium ions can enter the dendritic compartment (Sabatini *et al.*, 2002; Chen & Sabatini, 2012). Initial estimates for electrical resistances of the spine neck were thought to be too low to suggest that spine heads are electrically compartmentalized (Svoboda *et al.*, 1996), but more recent findings suggest that increasing spine neck resistance increases AMPAR-mediated depolarization in the respective spine (Grunditz *et al.*, 2008). Furthermore, Holbro *et al.*, (2010) showed that calcium elevations in spines were increased in peak amplitude by AMPAR activation. In addition, they showed that spines with narrow necks (measured indirectly by FRAP) displayed larger calcium transients (and resembled those that were partly driven by AMPAR activation). These results support the view that constricted spine necks create greater impedance for incoming synaptic signals and promote larger AMPAR-mediated depolarizations within the spine.

Harnett *et al.* (2012) indirectly measured the voltage drop across spine necks by recording dendritic excitatory postsynaptic potentials (EPSPs) in apical dendrites of hippocampal CA1 neurons while simultaneously imaging calcium transients evoked by glutamate uncaging at a single spine (in the presence of NMDAR and VGSC inhibitors to measure the calcium transient delivered solely by VGCCs). Harnett *et al.* (2012) then elicited a calcium elevation in the same spine by injecting different sized excitatory postsynaptic current (EPSC)-shaped currents to depolarize the spine. Using this approach, a current injection (via a dendritic patch pipette) would eventually be found that elicited a calcium transient matching the one evoked by glutamate uncaging. The amplitude of the current injection required to mimic the original calcium transient is an accurate measure of the original current arising in the spine because high impedance of the spine head limits the voltage drop across the neck when current flows from dendrite to spine. For thinner oblique dendrites, not accessible with a patching pipette, the authors performed simultaneous glutamate uncaging in neighboring spines until the calcium transient reached the same amplitude as a single uncaging event at that spine. Harnett et al used their estimates of spine neck resistances to model the effects of removing spine neck resistances on NMDAR conductance and supralinear input summation. Their model predicts that both would be significantly reduced by the absence of high impedance spine necks.

Supralinear summation of synaptic inputs is measured by increasing the number of synchronously stimulated synapses (with the preferred method being synchronous two photon glutamate uncaging; Losonczy & Magee, 2006) and measuring the EPSP at the soma. The amplitude of the EPSP increases linearly until a critical number of stimulations is reached (which varies depending on the location along the dendritic branch). At this point the EPSP amplitude shows a larger than linear increase. Weber *et al.* (2016) have used synchronous two-photon glutamate uncaging to demonstrate a form of LTP dependent on supralinear summation of synaptic inputs.

In summary, the evidence available at this time supports the view that electrochemical compartmentalization of spines enables dendritic processing of synaptic inputs (i.e. supralinear summation), which is probably an important component in many instances, *in vivo* and *in vitro*, for the induction of long-term potentiation (LTP).

(1.2) Synaptic function

(1.2.1) Basic principles of synaptic plasticity

Synaptic plasticity refers to the ability of synapses to increase or decrease their synaptic strength – that is, the extent to which a given synapse can influence the postsynaptic membrane potential. Long-term potentiation (LTP) is an enduring gain of synaptic strength, which was first measured in the hippocampus of the anaesthetized rabbit (Bliss & Lomo, 1973) and is now widely considered neurobiological basis of memory formation (Bliss & Collingridge, 1993; Malenka & Bear, 2004). Since the experimental LTP paradigm was first described, it has been frequently studied at the Schaffer collateral connections between the CA3 and CA1 pyramidal cell layers of the hippocampus (Bliss *et al.*, 2006). Thus, much of the current understanding of LTP is derived from the mechanisms driving it in this particular region. In CA1 neurons, LTP depends on NMDAR activation and, with appropriate stimulation protocols, can be sustained for days in vivo (Bliss & Collingridge, 1993).

Before dendrites started to be widely understood as computational units of the nervous system (Schiller *et al.*, 2000; Branco & Häusser, 2010), the need for multiple inputs to drive potentiation was already recognized as one of the core principles defining LTP (Bliss & Collingridge, 1993). Input cooperativity is the recruitment of multiple synapses by sufficiently strong stimulation to drive postsynaptic depolarization. Depolarization of the synapse summed with more widespread depolarization of the postsynaptic membrane delivers the necessary voltage change to drive local calcium elevations (Schiller *et al.*, 1998), which are required for LTP induction (Malenka & Bear, 2004). Another core feature of LTP – input specificity – is partially achieved through coincident

depolarization. Only synapses active within a time window determined by the more widespread depolarization will be potentiated. For long lasting, transcription-dependent LTP, additional mechanisms need to account for input specificity (see description of early and late LTP below). Associativity is the final principle of LTP, which is an extension of both input specificity and input cooperativity (Volianskis *et al.*, 2015) and is neurobiologically analogous to classical conditioning (Bliss & Collingridge, 1993; Volianskis *et al.*, 2015). According to the principle of associativity, a weak stimulus, which alone would have no plasticity effect, can induce LTP – in an input-specific manner – when delivered with stronger stimulation converging on the same cell or cells, but on an independent input (Volianskis *et al.*, 2015). This associative component of LTP can be demonstrated experimentally in the hippocampal slice, which contains two sets of Schaffer collateral projections that can be stimulated independently. The pathway receiving weak stimulation will result in potentiation only when delivered concomitantly with a strong stimulus to the other pathway (Barrionuevo & Brown, 1983; Clark & Collingridge, 1996; Dudman *et al.*, 2007).

(1.2.2) Early and late LTP

LTP exists in at least two experimentally distinguishable forms: early- and late-LTP (E-LTP and L-LTP). In E-LTP, the slope of the field EPSP returns to baseline after one or two hours (Bliss *et al.*, 2006; Lu *et al.*, 2008), whereas L-LTP should persist for at least five to six hours (Frey *et al.*, 1988). E-LTP depends on modification and trafficking of existing proteins (Bliss & Collingridge, 1993; Lu *et al.*, 2008) and can be blocked by protein kinase inhibitors (Malinow *et al.*, 1988; Malenka *et al.*, 1989; Bliss & Collingridge, 1993), whereas late phases of LTP require new protein synthesis and gene transcription (Nguyen *et al.*, 1994; Malenka & Bear, 2004). In order to preserve input specificity when LTP depends on signalling between active synapses and the nucleus, Frey & Morris (1997) proposed the synaptic tagging and capture hypothesis. According to the original proposal, E-LTP establishes a tagging molecule that captures ‘plasticity related proteins’ (PRPs), which are transported throughout the dendritic tree in a non-directed manner. Capture of the necessary PRPs will lead to L-LTP at the tagged synapse to convert E-LTP into L-LTP. Frey & Morris (1997) tested the synaptic tagging hypothesis by independently stimulating and recording the two distinct input pathways along Schaffer collateral fibres. They applied one of two stimulation protocols to either pathway – a weak stimulation protocol that would trigger only E-LTP and a stronger stimulus that would induce L-LTP. Applying the protein synthesis blocker, anisomycin, prior to stimulation with the strong stimulus of either pathway blocked L-LTP. If anisomycin was applied 35 minutes after strong stimulation of the first pathway and just before weak stimulation of the second pathway, L-LTP was still evoked in the second pathway. This L-LTP arising from the second stimulus could be blocked if a cut was applied to the brain slice such that the plasticity related proteins generated by the first stimulus never reached dendrites where the second

recording electrode was inserted. A revised version of the synaptic tagging hypothesis states that a synaptic tag is unlikely to be defined by a small number of molecules, but more likely refers to a temporary structural state of the synapse, which can be consolidated by capture of PRPs (Redondo & Morris, 2011).

A number of molecules have been proposed to participate as either a tag or a PRP and thereby enable input specificity during L-LTP. Endogenous expression of brain-derived neurotrophic factor (BDNF) promotes complete expression of LTP (Patterson *et al.*, 1996; Figurov *et al.*, 1996; Korte *et al.*, 1996), while blocking activation of its receptor (Minichiello *et al.*, 2002) – tyrosine kinase B (TrkB) – disrupts LTP expression. Furthermore, recent findings suggest that BDNF-TrkB signalling could constitute part of the synaptic tag enabling L-LTP input specificity (Lu *et al.*, 2011). Lu *et al.* (2011) used the classic two-pathway protocol, in combination with transgenic knockin mice carrying a mutant form of TrkB, to test the role of BDNF in synaptic tagging. These mice carry a single base pair substitution in the TrkB gene, which results in the protein becoming unresponsive to BDNF binding upon exposure to an exogenous ligand - 1NMPP1 (Chen *et al.*, 2005). Lu *et al.* (2011) stimulated one pathway with a weak TBS protocol, which resulted only in E-LTP if applied in isolation, and the other pathway with a strong TBS protocol, which would elicit L-LTP. They found that weak TBS would evoke L-LTP if applied to the second pathway one hour after the first pathway received strong TBS. However, the weak TBS did not evoke L-LTP in mutant-TrkB brain slices in which TrkB activity was blocked by 1NMPP1 prior to stimulation of the second pathway. These findings suggest that BDNF-TrkB signalling could form at least part of the tag and capture mechanism to preserve input specificity during L-LTP induction.

(1.2.3) Backpropagating action potentials (bAPs) and LTP

The induction and maintenance of LTP is complex. It relies on different mechanisms depending on developmental time points and brain areas being studied (Malenka & Bear, 2004; Kim *et al.*, 2015; Volianskis *et al.*, 2015). However, coincident depolarization and local intracellular rises in calcium concentration seem to be universal requirements. Coincident depolarization is achieved either through input cooperativity or by somatic action potentials backpropagating through the dendrites (Volianskis *et al.*, 2015). VGSCs are expressed in dendrites (Magee & Johnston, 1995*a*) and spines (Magee & Johnston, 1995*b*; Bywalez *et al.*, 2015), which facilitate the propagation of somatic spikes into the dendrites (Stuart & Sakmann, 1994; Stuart & Häusser, 2001). If backpropagating action potentials (bAPs) invade dendrites they could partially overlap with the synaptic activity that initiated them and provide the necessary associative signal for LTP induction (Stuart & Häusser, 2001; Bliss *et al.*, 2006; Feldman, 2012). Glutamate and glycine unbind from NMDARs on the order of tens of milliseconds (Silver, 2010). During this time EPSPs can sum to

initiate a somatic spike from which a bAP can enter the dendritic compartments where activity originally triggered the spike. The additional bAP-supplemented depolarization in these compartments may then be sufficient to relieve magnesium blockade of activated NMDARs (Kampa *et al.*, 2004, 2006; Feldman, 2012).

Simultaneous publications by Bert Sakmann and Daniel Johnston showed that when dendritic depolarizations overlapped with bAPs, potentiation could be evoked in cortical neurons (Markram *et al.*, 1997) and CA1 neurons (Magee & Johnston, 1997). Markram *et al.* (1997) showed, in pairs of current-clamped cortical neurons, that pairing presynaptic spikes 5-10ms before postsynaptic spikes could induce stable potentiation of the recorded EPSP for 40-45 minutes. Markram *et al.* (1997) also showed that switching the order of events such that the presynaptic spike came after the postsynaptic spike, induced depotentiation. Magee & Johnston (1997) blocked VGSC in apical regions of CA1 dendrites by local application of 10µM tetrodotoxin just before applying their LTP induction protocol. Local blockade of VGSCs in this manner inhibited LTP induction. These results are consistent with the view that bAPs are mediated by dendritic VGSCs and sum with synaptic potentials leading to calcium concentration elevations that initiate the induction process for LTP.

LTP is an event underpinned by complex components, which may vary substantially in their complexity depending on the length of time LTP is being sustained. Furthermore, the mechanisms driving LTP might vary across brain regions for any definition of LTP that is sensitive to the length of time LTP has been sustained. However, coincident depolarization leading to calcium influx is a common factor necessary for successful LTP induction.

(1.2.4) Spine calcium transients and voltage-gated calcium channels

Subtype	**Alpha 1 subunit**	**Current**	**Antagonist**
CaV1 (HVA)			
CaV1.1	1S	L-type	nimodipine
CaV1.2	1C		
CaV1.3	1D		
CaV1.4	1F		
CaV2 (HVA)			
CaV2.1	1A	P/Q-type	Agatoxin-IVA
CaV2.2	1B	N-type	Conotoxin-GVIA
CaV2.3	1E	R-type	SNX-482

CaV3 (LVA)			
CaV3.1	1G	T-type	TTA-P2
CaV3.2	1H		
CaV3.3	1I		

Table 1: Summary of the voltage-gated calcium channel subtypes (Bloodgood & Sabatini, 2005; Dolphin, 2016).

With calcium entry through synaptic NMDARs initiating many interesting forms of potentiation, measuring spine calcium transients has garnered much experimental attention. Spine calcium transients can be evoked by bAPs (Yuste & Denk, 1995; Bloodgood & Sabatini, 2005) or by synaptic stimulation (Emptage *et al.*, 1999; Kovalchuk *et al.*, 2000; Sabatini & Svoboda, 2000). Voltage-gated calcium channels (VGCCs) are known to exist in dendritic spines and contribute to the overall amplitude of spine calcium transients (Yuste & Denk, 1995; Westenbroek *et al.*, 1995; Kovalchuk *et al.*, 2000; Bloodgood & Sabatini, 2007).

All VGCCs contain an alpha1 pore forming subunit of which there are 10 isoforms in the mammalian nervous system (Catterall, 2011; Dolphin, 2016). These isoforms give rise to three families of VGCCs – CaV1, CaV2 and CaV3 (see Table 1). Four CaV1 family members (CaV1.1-1.4) are sensitive to block by dihydropyridine antagonists such as nimodipine and conduct L-type currents. CaV2.1 channels conduct P- or Q-type calcium currents, which are inhibited by omega-agatoxin IVA, while CaV2.2 channels conduct N-type calcium currents, which are blocked by omega-conotoxin-GVIA. CaV2.3 channels conduct R-type calcium currents, which are resistant to block by dihydropyridines and toxin blockers specific for other CaV2 family members, but can be blocked by tarantula toxin, SNX-482. CaV3 channels produce T-type calcium currents and are blocked by mibefradil (Sabatini & Svoboda, 2000; Bloodgood & Sabatini, 2007) and more selectively by TTA-P2 (Shipe *et al.*, 2008).

As well as the alpha1 subunit, alpha2delta and beta subunits form part of the functional CaV1 and CaV2 channel complex (Dolphin, 2016). There are several distinct variants of alpha2delta and beta subunits emerging from different genes and alternative splicing (Catterall, 2011). These subunits substantially influence biophysical properties of these channels, but it is unknown what determines final subunit composition (Catterall, 2011; Dolphin, 2016).

CaV1 and CaV2 families belong to the class of high voltage activated (HVA) channels because they are activated by relatively large depolarizing voltage steps, while CaV3 channels are activated by smaller depolarizations and are thus low voltage activated (LVA) channels (Hille, 2001). In addition to a lower activation threshold from resting potentials, CaV3 channels inactivate during

prolonged depolarization steps and require membrane hyperpolarization before they can again enter the hyperpolarized state (Hille, 2001; Jaafari *et al.*, 2014).

Studies offering detailed insights into VGCC contributions to spine calcium transients used patch clamp techniques to fill neurons with synthetic calcium indicator and then applied current injections to trigger bAPs (Sabatini & Svoboda, 2000; Bloodgood & Sabatini, 2007). Calcium from depolarized dendrites does not immediately enter the spine head due to compartmentalization caused by narrow spine necks (Yuste & Denk, 1995; Sabatini & Svoboda, 2000; Sabatini *et al.*, 2002). By measuring peak amplitudes immediately after the fast rise of the calcium transient, it is possible to measure calcium contributions from spine VGCCs (Sabatini & Svoboda, 2000). Using this experimental design, Sabatini and colleagues found that CaV2.3 and CaV3 channels mediate most of the bAP-induced calcium transient (Sabatini & Svoboda, 2000; Bloodgood & Sabatini, 2007), while smaller contributions can be measured from CaV1 and CaV2.2 variants (Bloodgood & Sabatini, 2007).

Studying VGCC contributions to synaptically evoked calcium transients is problematic unless spines are activated using glutamate uncaging (e.g. Schiller *et al.*, 1998). Activation of presynaptic VGCCs might be inhibited by bath application of VGCC blockers intended for postsynaptic VGCCs, thereby complicating interpretation of the results. Another factor to consider is that NMDARs can contribute substantially to spine calcium transients when subthreshold stimulation is applied (Schiller *et al.*, 1998; Kovalchuk *et al.*, 2000). NMDARs are more permeable to monovalent cations than calcium (Dingledine *et al.*, 1999). So, these channels can contribute directly to the measured calcium signal, trigger calcium-induced calcium release (CICR) from internal calcium stores (Emptage *et al.*, 1999; Reese & Kavalali, 2015) and they can also contribute to depolarization of the spine, which promotes activation VGCCs.

Some studies suggest that CICR accounts for some (Reese & Kavalali, 2015) or even almost all spine calcium transients (Emptage *et al.*, 1999). However, most studies report no significant contribution from internal stores to spine calcium transients (Schiller *et al.*, 1998; Yuste *et al.*, 1999; Kovalchuk *et al.*, 2000; Sabatini & Svoboda, 2000; Sabatini *et al.*, 2002). Schiller *et al.* (1998) used two-photon glutamate uncaging to trigger calcium transients selectively in single spines. Applying 150-500uM cadmium (a non-specific VGCC antagonist) blocked 80% of the calcium transient while AP5 (a NMDAR specific antagonist) blocked the rest. Triggering glutamate uncaging and bAPs together changed the ratio of VGCC-NMDAR contribution from 80:20 to 40:60. Most likely, this result is explained by the additional depolarization from bAPs providing stronger unblock of magnesium ions in the NMDAR pores (Schiller *et al.*, 1998; Svoboda, 1998).

Spine calcium transients require activation of NMDARs (Kovalchuk *et al.*, 2000), which contributes directly to the measured calcium elevation, but also depolarizes the spine membrane leading to activation of CaV2.3 and/or CaV3 present in the spine. The level of direct contribution made by NMDARs depends on extracellular magnesium concentrations (Kovalchuk *et al.*, 2000) and type of stimulation applied.

(1.2.5) Voltage-gated calcium channels and LTP

Considering that VGCCs channels promote synaptic calcium signals (Schiller *et al.*, 1998; Sabatini & Svoboda, 2000; Bloodgood & Sabatini, 2007), it could reasonably be expected that activation of these channels is an important part of synaptic plasticity induction or maintenance. Numerous studies show that VGCCs are most likely involved in the induction and/or maintenance of LTP, although the use of non-specific blockers may complicate deducing which channel subtypes are involved.

Magee & Johnston (1997) found that LTP in CA1 pyramidal neurons was induced by pairing subthreshold synaptic stimulation with somatic action potentials. 50µM nickel reduced EPSP potentiation by approximately 30%, while 10µM nimodipine reduced potentiation by 70%. At 50µM, nickel blocks CaV3.2 channels (Lee *et al.*, 1999) and CaV2.3 channels (Metz *et al.*, 2005; Tai *et al.*, 2006), while nimodipine is a dihydropyridine targeting mainly CaV1 subtypes, but can also inhibit T-type channels at 10µM (Randall & Tsien, 1997). In addition, Yasuda *et al.* (2003) reported an impairment of EPSP potentiation in the presence of 50µM nickel in CA1 following application of an LTP-inducing pairing protocol.

Kampa *et al.* (2006) examined the role of postsynaptic spike bursting in pairing protocols similar to those used by previously mentioned studies (section 1.2.3). They paired single presynaptic action potentials with three postsynaptic spikes (delivered at 200Hz) from synaptically coupled L5 neurons. These experiments were carried out in layer 5 pyramidal neurons, which have the most elaborate dendritic tree of the pyramidal cell class and strongly attenuate bAPs (Stuart & Sakmann, 1994). The authors found that spike bursting at >100Hz is necessary to induce LTP at low pairing frequencies – presumably to overcome the attenuation of single spikes as they penetrate into the dendritic tree. Spike bursts trigger calcium spikes in layer 5 pyramidal dendrites (see also Larkum *et al.*, 1999), which Kampa *et al.* (2006) found to be impaired by 100µM nickel. Nickel also abolished LTP induced by their pairing protocol. The results from Kampa *et al.* (2006) are consistent with CaV2.3 or CaV3 channels supporting calcium spikes in L5 pyramidal neurons, which could provide part of the associative signal and be more essential for LTP induction at distal synapses.

CaV1 channels have been strongly implicated in late phases of LTP (L-LTP) (Impey *et al.*, 1996; Morgan & Teyler, 2001; Raymond & Redman, 2002). Morgan & Teyler (2001) used field recordings of CA3-CA1 Schaffer collateral synapses and different theta burst stimulation (TBS) protocols with different strengths. With a TBS protocol of middling strength, the authors reported that 30µM nifedipine significantly impaired LTP while AP5 completely blocked LTP expression. Their strongest TBS protocol produced a type of NMDAR-independent LTP that could be completely blocked by 30µM nifedipine application. Morgan & Teyler (2001) clearly show a VGCC-dependent component in a classic NMDAR-dependent LTP pathway and that, with stronger stimulation, LTP might become VGCC-dependent rather than NMDAR-dependent. One caveat of this study and others (Impey *et al.*, 1996; Raymond & Redman, 2002) is the use of nifedipine, which is one of the less specific dihydropyridines and at 10-30µM may also block CaV3 channels in addition to CaV1 (McDonald *et al.*, 1994). Nevertheless, these studies collectively confirm that CaV1 and CaV3 channels participate in LTP expression.

(1.2.6) Distance-dependent LTP induction rules

bAPs are thought to provide part of the depolarizing signal triggering stronger removal of magnesium block, which leads to higher calcium concentrations at synapses with coincident depolarization (Stuart & Sakmann, 1994; Schiller *et al.*, 1998; Stuart & Häusser, 2001). When delivered at low frequencies, pairing synaptic stimulation with bAP-inducing current injections fail to promote LTP unless bAPs occur in high frequency bursts of three or more spikes (Kampa *et al.*, 2006). This feature is thought to arise, at least in part, from the decrement of the bAP as it passes through the axial resistance and leak conductance present through the extent of the dendritic tree (Segev & London, 2000; Magee, 2000). Synapses further away from the soma would be exposed to a more attenuated bAP compared to proximal inputs resulting in distance-dependent learning rules being applied across the dendritic tree (Froemke *et al.*, 2005; Sjöström & Häusser, 2006; Letzkus *et al.*, 2006). Characteristic anti-Hebbian plasticity can be observed in distal inputs of L5 pyramidal neurons when bursts of at least three high-frequency spikes precede distal synaptic stimulation to produce LTP (Letzkus *et al.*, 2006) while pre-before-postsynaptic stimulation triggers LTD with high frequency trains of single action potentials (Sjöström & Häusser, 2006).

Studies investigating distance-dependent plasticity induction rules focus on L5 pyramidal neurons (Froemke *et al.*, 2005; Sjöström & Häusser, 2006; Letzkus *et al.*, 2006), which have the most extensive dendritic arborization of all pyramidal neurons and are therefore most likely to exhibit distance-dependent plasticity induction rules. Sjöström & Häusser (2006) made simultaneous L2/3-L5 and L5-L5 pyramidal neuron recordings while pairing spike-evoking current injections at 50Hz.

This stimulation pattern induced LTP in L5-L5 pairs, but LTD in L2/3-L5 pairs. L2/3 project to both distal and proximal locations along L5 dendrites, while L5 neurons project only to proximal regions of neighboring L5 neurons (Markram *et al.*, 1997; Thomson & Bannister, 1998).

Cable properties of dendrites that contribute to the attenuation of bAPs also increase the rise times of somatically recorded EPSPs or EPSCs (Rall, 1967). Sjöström & Häusser (2006) show that EPSPs with longer rise times tend to exhibit long-term depression (LTD) following application of their stimulation paradigm, which suggests that more distal synapses could be prone to induction of LTD, rather than LTP, during coincident synaptic stimulation and bAP-mediated depolarization in L5 pyramidal neurons. By applying weak extracellular stimulation of distal inputs, the authors could mimic the anti-Hebbian LTD detected at L2/3-L5 connections. Stronger extracellular stimulation resulted in the sign of plasticity being switched at distal synapses from LTD to LTP. Current injection through a dendritic, rather than somatic, patch pipette similarly altered the direction of plasticity at distal synapses. Presumably, distance-dependent attenuation of membrane depolarization at distal apical synapses is reduced by current injection in the apical branch compared to somatic current injection, while stronger extracellular stimulation increases input cooperativity, which increases local depolarization.

Interestingly, Sjöström & Häusser (2006) also reported that coupling strong synaptic stimulation with bAPs, evoked by somatic current injection, resulted in supralinear calcium signals, which showed an increasing peak amplitude with increasing distance from the soma. This is consistent with a report by Letzkus *et al.*, (2006), who found LTP at distal synapses of L5 pyramidal neurons when spike bursts preceded synaptic stimulation. This anti-Hebbian LTP at distal inputs was sensitive to 100µM nickel implying that VGCCs might play an important role in distance-dependent plasticity induction.

Distance-dependent plasticity induction rules might depend on differential expression of ion channels and other proteins involved in synaptic transmission and plasticity, although little experimental evidence exists to directly support this notion. Ideally, functional studies similar to those carried out by Svoboda and others would be applied to the question of distance-dependent distribution of VGCCs to synaptic calcium transients. However, the methods applied so far to the study of synaptic calcium transients loosely define locations where inputs were sampled along the dendritic tree and are not well suited to collection of data from large numbers of synapses.

(1.3) Experimental approaches for studying synaptic function

(1.3.1) Whole cell patch-clamp applied to neurons

Whole cell patch-clamp techniques have an essential role in the study of synaptic physiology (Spruston & Johnston, 2008). A major advantage of clamping membrane voltages using these techniques is that strong seals between the glass tip of the micropipette and the plasma membrane must first be established. A high resistance seal enables small synaptic currents and passive properties of the cell – such as the membrane resistance (Spruston *et al.*, 1994) – to be more accurately measured. Despite these advancements, whole cell patch-clamp does not link synaptic activity to a particular location along the neuronal membrane. Instead, activity across the entire dendritic tree is pooled together from all synapses belonging to the recorded neuron. In some experimental situations, this can be a limitation – for example, when input location is thought to determine the plasticity induction rules that apply to a given synapse (Froemke *et al.*, 2005; Sjöström & Häusser, 2006; Letzkus *et al.*, 2006).

Another disadvantage of patch-clamp techniques being applied to neurons is that high cytosolic resistivity along narrow dendrites distorts synaptic currents and membrane potential changes recorded with somatic patch pipettes. Modelling cable properties of dendrites suggest that amplitudes of synaptic currents are attenuated and the kinetics of these currents are delayed using realistic dendrite distances and axial resistance (Spruston, 2000). Williams & Mitchell (2008) have shown in dynamic patch-clamp (Sharp *et al.*, 1993) recordings that currents injected into the dendrites of L5 pyramidal neurons are recorded with heavy distortion at the soma. They also showed that measures taken to improve the space-clamp – in particular, cesium-based recording solutions and series resistance compensation – did little to improve the uniformity of voltage-clamp across the membrane.

Some studies have measured an increase in synaptic current amplitudes along the length of apical dendrites belonging to CA1 pyramidal neurons (Magee & Cook, 2000; Shipman *et al.*, 2013). In these studies, recording pipettes patch sections of the apical dendrite at different distances from the soma. The consensus from these studies is that average currents evoked with hyperosmotic solution are larger with increasing distance from the soma. It would seem that this effect is dependent upon expression of GluA2-containing AMPARs (Shipman *et al.*, 2013). This finding is consistent with another study applying non-stationary fluctuation analysis to recordings derived from combined glutamate uncaging at single spines and dendrite patch-clamp, which found that AMPAR density was increased at more distal CA1 synapses (Smith *et al.*, 2003).

Increasing functional AMPAR expression with increasing distance from the soma has been demonstrated only in large apical dendrites, which are accessible by patch pipettes. Most synaptic inputs occur on small caliber, un-patchable dendrites branching from the main apical dendrite. Menon *et al.* (2013) applied serial section electron microscopy and immunogold labelling of AMPARs to measure changes in expression along different compartments of oblique apical dendrites in CA1 neurons. They distinguished between two types of spine that could be readily identified in electron micrographs – perforated and non-perforated spines. Perforated spines have large, doughnut-shaped postsynaptic densities whereas non-perforated spines have smaller, concentric postsynaptic densities. Perforated spines had higher AMPAR particle numbers and densities in dendrite sections closer to the branch point, compared to medial and distal section of oblique apical dendrites. Menon *et al.* (2013) suggest that studies showing increases in miniature EPSCs (mEPSCs) with distance from the soma along main apical branches are recording synaptic activity principally at perforated spines. Currents from non-perforated spines (which are considerably more abundant than perforated spines) are expected to be smaller and more prone to be obscured by noise (Menon *et al.*, 2013).

Patch-clamp is an essential technique for the study of synaptic function, but this approach yields measurements prone to uneven distortions depending on the distance between the recording pipette and site of activity. These errors are still not completely understood. To gain insights into synaptic function without uneven distortion of the measured inputs and spatial information relating to those inputs, imaging approaches are required.

(1.3.2) Imaging tools: hardware

Without whole cell recording techniques much of synaptic physiology would be inaccessible to experimentation. Nevertheless, the absence of spatial information during whole cell recordings and the level of unknown distortion that may affect signals recorded by more distal sites on cells with complex dendrites, have encouraged the development of optical techniques to probe synaptic function.

Roger Tsien made synthetic calcium indicators more accessible to neuroscientists (Russell, 2011; Grienberger & Konnerth, 2012) and subsequently promoted the development of membrane permeable dyes (Grinvald, 2005) and genetically encoded calcium indicators (GECIs) (Miyawaki *et al.*, 1997). GECIs are advantageous because their expression can be limited to the genetic identity of the cells under study. Dyes must be applied to cells as AM-conjugated compounds (Tsien, 1983; Grinvald, 2005) in which case background signal from different cell populations will be high and hinder analysis, or dyes have to be delivered invasively through a patch pipette. Unless the

experimenter needs to record synaptic potentials while simultaneously imaging calcium transients, having to deliver dyes with a patch pipette is an inconvenience that will slow down data acquisition.

Prior to development of the latest generation of GCaMP calcium sensors (Chen *et al.*, 2013), no GECI was as sensitive as the most sensitive synthetic calcium indicator. Therefore, investigators had to choose between sensitive synthetic dyes applied using invasive physical or non-specific chemical methods or less sensitive GECIs applied using genetic methods. The latest GCaMP sensors – GCaMP6 variants – are at least as sensitive as the most sensitive fluorescent dyes. They also have large dynamic ranges, an absence of bleaching and very little phototoxicity (Chen *et al.*, 2013).

Many of the gains made in advancing calcium sensors would have limited utility without developments in camera technology to capture fluorescence intensity changes across large dynamic ranges and at high frame rates whilst keeping signal-to-noise levels acceptable. Digital charged-coupled device (CCD) cameras have been standard hardware in imaging for many years. More recently, electron-multiplying CCD (EMCCD) cameras reduce the impact of readout noise on the signal-to-noise ratio by amplifying the number of electrons produced per photon before the image is transferred from the detector (Rasnik *et al.*, 2013). Furthermore, for this operation to function, the camera must be cooled, which fortuitously reduces noise from other sources (Rasnik *et al.*, 2013).

Increased sensitivity of calcium sensors – particularly with the latest generation of GCaMP sensors – means that samples can be imaged with lower exposure times without losing too much signal. Together, technological advances in the imaging hardware, such as EMCCD cameras, and improvements in calcium sensors enable biological signals to be read out at faster frame rates across larger numbers of pixels. These developments have been crucial, but establishing adequate software tools that do not demand undue levels of manual input is another challenge.

(1.3.3) Imaging tools: software

Imaging calcium transients in spines is typically restricted to single spines using line scan confocal imaging (Emptage *et al.*, 1999; Sabatini & Svoboda, 2000; Bloodgood & Sabatini, 2007; Enoki *et al.*, 2009) or a small number of spines with two-photon microscopy (Losonczy & Magee, 2006; Weber *et al.*, 2016). In these studies, neither detection nor identifying regions of interest (ROIs) are likely to pose major challenges. Spine calcium transients are typically imaged simultaneously with electrophysiological recordings of synaptic activity while spine locations are predefined and few in

number. Thus, detecting whether or not transients occurred and isolating a small number of ROIs are simple tasks in such cases.

However, detection of calcium transients and identifying ROIs are potentially major challenges in calcium imaging experiments collecting many transients from many ROIs (Kleindienst *et al.*, 2011; Takahashi *et al.*, 2012; Reese & Kavalali, 2015). The rules for plasticity induction are likely to vary with distance form major points of synaptic integration – the cell body in particular (Froemke *et al.*, 2005; Sjöström & Häusser, 2006; Letzkus *et al.*, 2006). Voltage-gated channels and other synaptic proteins are likely to vary in their expression profiles to support these observed differences in functional properties of different spine populations. By imaging spontaneous calcium transients across all spines under the field of view, testing divergent sensitivities of different spine populations to various pharmacological agents or recombinant proteins becomes feasible.

Numerous software tools for analyzing calcium transients arising from gating internal store channels in cardiac myocytes exist (Francis *et al.*, 2012; Ellefsen *et al.*, 2014). These tools are designed to analyze transients emerging from subcellular structures – on the same scale as spines – but all require manual or semi-automated placement of ROIs during analysis. For measuring calcium transients across a multitude of synapses, this would be an unacceptably laborious task and open the procedure to user bias.

On the cell body scale many excellent procedures exist for isolating individual, tightly packed cells with complex morphologies, such as activity correlation imaging (ACI; Junek *et al.*, 2009). In this analysis strategy, small sections of the dendritic tree (that would be difficult if not impossible to isolate manually) can be extracted from background and surrounding structures belonging to other cells, by correlating calcium signals between a reference trace (derived from the easily identifiable cell body) and signals from other pixels. Activity in cellular compartments belonging to the same cell will be much more strongly correlated while activity in unconnected compartments will be uncorrelated. Other mathematical approaches taken include principal and independent components analysis. These can also be used to isolate single cells and their components from background (Mukamel *et al.*, 2009).

Although mesoscopic scale analytical approaches, such as ACI and principle components analysis, facilitate the identification of single cells and all connected compartments, they are less suited for pinning ROIs to individual spines. Currently, there is no well-defined strategy for accomplishing this. Reese & Kavalali, (2015) used overexpression of synaptobrevin tagged to a red fluorophore to identify ROIs. This is theoretically an elegant approach, but how well each synapse is optically segregated from tightly packed neighbours (using diffraction-limited imaging

techniques) is open to doubt. In the current study (section 3.2.1), the extent to which PSD95-RFP+ puncta could be individually resolved required increasing the fluorescence intensity threshold such that puncta with weaker expression would no longer be detected. Keeping lower thresholds to avoid this loss would likely result in merging of distinct puncta. Manually resolving merged puncta with lower thresholds leads to the aforementioned caveats of user bias and laboriousness.

As outlined in section 1.1.4, biochemical compartmentalization of the spine prevents calcium transients spreading far from their point of initiation (Sabatini *et al.*, 2002; Bloodgood & Sabatini, 2005; Nishiyama & Yasuda, 2015) and can thus be expected to have symmetrical shapes at the point of maximum event spread. These features make spine calcium transients themselves well suited for defining ROIs along dendritic branches.

Materials and Methods

(2.1) Animals

Pregnant Wistar rats were obtained from the Universitätsmedizin Göttingen animal facility at day 18-20 postcoitus, or embryonic day 19 (E19). In some cases, pregnant rats were also bought from Charles River International Laboratories.

Three male-female pairs of heterozygous floxed-TrkB mice were kindly provided by the Rüdiger Klein group at the Max Planck Institute of Neurobiology, Munich. The offspring from these breeding pairs were genotyped and homozygous floxed mice were selected to make additional breeding pairs. Homozygous floxed mice were used in all experiments.

Use of animals for experiments was carried out in accordance with the relevant institutional guidelines and German law.

(2.2) Cell Culture

All cell culture techniques have been adapted from previously established protocols. Details about the procedures used are described. A complete list of the medium components, working concentrations, suppliers and catalogue numbers used for the preparation of dissociated cultures is provided at the end of the Materials and Methods section.

(2.2.1) Preparation of dissociated hippocampal cultures from E19 embryos

Preparation of dissociated hippocampal cultures from E19 rat pups was performed based on the procedures laid out in Goslin *et al.*, (1998). Two or three 10cm petri dishes containing E19 dissection medium (see Table 2.1 for list of E19 media formulations) were placed on ice in a HERAguard ThermoScientific dissection hood. Approximately 14ml of E19 dissection medium was placed in a falcon tube to hold dissected hippocampi on ice while the dissection was ongoing. All tools (forceps, scissors) and work surfaces were sterilized with 70% ethanol. At least 2ml 0.05% or 0.25% Trypsin-EDTA (Gibco, #25300-054 and #25200-056) and 15ml of E19 dissection medium was set to warm to 37°C. A sufficient volume of E19 plating medium for all culture plates was placed into a 5% CO2 incubator to equilibrate.

E19 pregnant Wistar rats were killed by rising carbon dioxide levels. Prior to opening the abdominal cavity to retrieve the rat embryos, cervical dislocation was applied to the backbone of the asphyxiated rat. Embryos were removed from the abdominal cavity and placed in an empty

petri dish outside the dissection hood. Heads were removed from the embryos and placed in one of the petri dishes containing E19 dissection medium. Brains were removed by pinning the heads to the bottom of the dish using forceps and cutting open the back of the skull (approximately along the fissure between the cerebral cortex and the cerebellum) before gently pressing down on top of the skull (with slight pressure towards the back of the skull) to force the brain out of the opening created at the back of the skull.

A single pregnant Wistar rat yielded between 8-15 pups. With higher yields, brains were usually split between two petri dishes to avoid clumping of dissociated cells. One dish was kept on ice while the hippocampi were removed from the brains in the other dish. Hippocampi were removed with the aid of a standard light microscope. First the brain was hemisected and for each hemisphere the meninges were removed. Two forceps were used to remove the hippocampus - at least one of these had a fine tip suitable for cutting brain tissue. After hemisection, remaining midbrain tissue was removed and the hippocampus was cut out from the dorso-caudal region behind the cortex. After all hippocampi were collected, the tissue was chemically triturated in 0.05% or 0.25% Trypsin-EDTA (Gibco, #25300-054 and #25200-056) for 20 minutes. The remainder of the dissection was carried out under sterile conditions in a HERAsafe Thermo Scientific cell culture hood. The tissue was then gently washed three times with 5ml of prewarmed E19 dissection medium. After the final wash, most of the E19 dissection medium was removed and 1ml of plating medium was added to the tissue suspension. Mechanical trituration using a 1ml pipette tip was applied to the tissue in order to get a single cell suspension. Typically, 10 up and down motions were sufficient to completely break up clumps of tissue. The tip was kept submerged in the suspension during the procedure in order to avoid introducing bubbles, which can reduce cell yield. Any remaining tissue clumps were removed by straining the suspension through a 100µm cell strainer (Corning, Inc., #352360). For 10 or more pups, an additional 9ml of E19 plating medium was passed through the cell strainer. For fewer pups, 4ml was used. The cell density was estimated by mixing 10µl of cell suspension with 10µl of Trypan Blue (Sigma, #T8154) – to exclude dead cells – and counting cells in this Trypan Blue mix using a haemocytometer slide. The cell suspension was diluted with E19 plating medium to 120-160,000 cells/ml. To each well, in a 24-well plate containing poly-l-lysine-coated (0.5mg/ml) 12mm coverslips, 0.5ml of cell suspension was added, giving a final density of approximately 53,100 cells/cm^2.

(2.2.2) Maintenance of E19 hippocampal cell cultures

The freshly plated cells were left overnight and the following day, the plating medium was replaced by feeding medium. Serum factors present in the plating medium aide the growth of astrocytes (Michler-Stuke *et al.*, 1984; Kniss & Burry, 1988), which in turn promotes neuron survival (Banker,

1980). The feeding medium contains B27 supplement, which has been developed specifically to promote cell survival in serum-free medium (Brewer *et al.*, 1993) and GlutaMAX – a dipeptide form of glutamine, which is essential for cell survival. In order to avoid overgrowth of glia cells in this culture system, 5µM arabinofuranosyl cytidine was added after 7-8 days in vitro.

(2.2.3) Preparation of dissociated hippocampal cultures from postnatal day 0 (P0) mice

Although the standard P0 dissection protocol (based on the E19 dissection protocol) could produce viable cells that survived and grew under E19 culture conditions, on many occasions the cells would tend to cluster and not tolerate transfection protocols very well.

The dissection procedure was adapted based on previously published protocols (Huettner & Baughman, 1986; Bonnet *et al.*, 2013). Ankit Awasthi – a fellow PhD candidate in the lab – played an essential role in facilitating my adoption of this technique. He first started applying the protocol and after observing his cultures I decided to apply the protocol myself. See Table 2.2 for a complete list of the medium formulations relevant for P0 dissociated neuronal cell culture preparation.

Components of the enzyme solution and inactivation solution were prepared before the dissection day. For the enzyme solution, 2mg of L-cysteine was dissolved in 1ml of P0 dissection medium and stored at -20°C in 15ml falcon tubes. Similarly, 1ml aliquots of serum medium containing 25mg of bovine serum albumin (BSA) were stored at -20°C in 15ml falcon tubes. DNase I was prepared at a concentration ≥1500 units/ml and aliquoted to 0.2ml in 1.5ml eppendorf tubes.

Prior to beginning the dissection procedure for the P0 protocol, enzyme and inactivation solutions were prepared along with the necessary volumes of serum medium, P0 plating medium and P0 dissection medium. 1mM calcium chloride and 0.5mM Na-EDTA (pH8) was added to a 15ml falcon tube containing 2mg/ml L-cysteine. An additional 9ml of P0 dissection medium was added to the tube to reach a final volume of 10ml enzyme solution. The inactivation solution was prepared by adding 9ml to a 15ml falcon tube containing 25mg/ml of BSA. 1ml of P0 plating medium was added to each well of a 24-well plate containing 12mm coverslips coated with 0.5mg/ml poly-l-lysine. The enzyme solution, inactivation solution and 24-well plate were then placed in a 5% CO_2 incubator until required. In addition, about 10ml (10ml should be a sufficient volume for the trituration steps, cell counting and plating) of serum medium was stored in the incubator to equilibrate. A fire polished glass pipette was sterilized by spraying thoroughly with 70% ethanol and stored in the cell culture hood to dry.

Hippocampi were dissected from P0 mouse pups as follows: Each pup was rapidly decapitated using a pair of strong dissection scissors and the head was then semi-sterilized by rolling it in a thin film of 70% ethanol placed on the palm of a gloved-hand. After all the heads were collected in a petri dish containing P0 dissection medium, 0.1ml papain was added to the enzyme solution and the brains were removed. Initially, the skin was cut away with dissection scissors on the side of the head and peeled away before cutting along the side of the skull. At this point the brain could easily be pushed out of the skull cavity with forceps and into a petri dish containing cold E19 dissection medium. The brains were collected in this way from each P0 pup. To remove the hippocampi from the brain, two to three brains were placed in another petri dish containing the same medium and placed under the microscope, off-ice. The remaining part of the skull on top of the brain was peeled off and then the hippocampi could be removed as per the E19 protocol detailed above.

When all the hippocampi had been collected, most of the P0 dissection medium in the tube holding the hippocampi was removed in the cell culture hood and replaced with 0.22µm-filtered enzyme solution. The tissue was then left to chemically triturate at 37°C in a water bath. The enzyme solution was then removed and replaced with 0.22µm-filtered inactivation solution. The tissue was incubated with the inactivation solution for two minutes and then replaced with one glass pipette load (equivalent to 1-2ml) of equilibrated serum medium. The tissue was then mechanically triturated with the glass pipette. For optimal results, five pulls were initially made and then the remaining clumps allowed to settle for three minutes at the bottom of the tube. The supernatant was extracted and stored in a second tube before a second pipette-load of serum medium was added to the remaining clumps. The tissue was further triturated with additional 10-15 pulls. The suspension was again left to stand for three minutes and the supernatant added to the second tube. Any remaining clumps of tissue would likely not yield living cells and were discarded. The cell suspension was spun down at 500xg for five minutes and the supernatant was sucked off with a vacuum pump. This helped to remove dead cells and associated compounds from the suspension. The cells were re-suspended in equilibrated serum medium with a volume of 0.5ml x number of pups for dissection. Cells were counted as per the E19 dissection protocol and the suspension diluted to 1.2 million cells /ml. 0.1ml of the suspension was added to the 24-well plated containing 1ml of P0 plating medium. It was important to add the suspension dropwise directly over the centre of the well. Mixing the suspension with the plating medium too thoroughly would lead to cells not adhering to the coverslip and poor health of the cultures. The final cell density per coverslip was estimated to be 106,100 cells/cm^2.

(2.2.4) Maintenance of P0 hippocampal cell cultures

At DIV4 5µM arabinofuranosyl cytidine was added to each well to limit astrocyte growth. At DIV7 and DIV14 50% of the medium in the wells was exchanged for feeding medium (see Table 2.1).

(2.2.5) Calcium phosphate precipitate transfection for neuronal cell culture

Calcium phosphate transfection was carried out based on the procedures described in Dresbach *et al.* (2003) and Jiang & Chen (2006), but with some important modifications.

Washing the cells with slightly acidified Neurobasal medium reportedly facilitates the removal of excess calcium phosphate-DNA precipitate from the cultures (Jiang & Chen, 2006). So, I adopted the strategy of using Neurobasal medium that had been equilibrated for several hours or overnight in a 10% CO_2 incubator (Midi40 CO_2 Incubator, Thermo Scientific) to slightly reduce the pH of the washing medium.

For every well to be transfected, 1µg of DNA, 1.87µl of 2M $CaCl_2$ and 15µl of transfection buffer* were mixed together under sterile conditions in a cell culture hood. The final volume of undiluted transfection mix should be 30µl per well and was made up to this volume with autoclaved dH_2O. In preparing the transfection mix, the necessary volume of dH_2O was added to a 1.5ml eppendorf tube and mixed well with the appropriate volume of 2M $CaCl_2$. Then the necessary volume of DNA solution was added to the $CaCl_2$ and water, followed by 1/8 of the total transfection buffer volume at a time. I followed the recommendation of Jiang & Chen (2006) to gradually add the transfection buffer volume to the DNA-$CaCl_2$-water mix, by mixing 1/8 of the necessary volume at a time. This reportedly produces finer phosphate precipitate that is more likely to be endocytosed into the cells and thereby improves transfection efficiency. At no point was the transfection mix vortexed. This was found at an early stage to reduce transfection efficiency. Once the undiluted transfection mix was prepared, it was placed in the dark for 5-20 minutes. Meanwhile, the conditioned medium in each well, which was to receive transfection mix, was replaced with 0.75ml Neurobasal medium (equilibrated in a 5% CO_2 incubator). The conditioned medium was supplemented with 10-15% of its volume with fresh medium, passed through a 0.22µm filter and then stored in the 5% CO_2 incubator.

One approach that dramatically improved cell survival and transfection efficiency was to adjust the osmolality of the transfection mix to match that of the conditioned medium (approximately 240mOsm/kg). The osmolality of undiluted transfection mix reached >600mOsm/kg, but could be reduced to approximately 240mOsm/kg by adding 1.5x its volume in dH_2O. After the 5-20 minutes of incubation, the transfection mix was diluted with 1.5x its volume with dH_2O and then immediately

applied to the wells. The mix was diluted by gently mixing with water by pipetting up and down two or three times. 84µl was applied to each well for maximum transfection efficiency. This was done by adding the diluted mix, dropwise, to the centre of each well. The cells were returned to the incubator and care was taken to avoid shaking the dish. Cells were exposed to the mix for 45-60 minutes and then washed initially by removing 0.75ml medium/mix in the well and replacing it with Neurobasal medium equilibrated in the 10% CO_2 incubator and then by a 2x exchanging of 0.5ml in each well with fresh 10%-equilibrated Neurobasal. After the final washing step, the transfection procedure was completed by replacing the Neurobasal wash medium with the original 1ml volume of conditioned medium in each well. Neurons were transfected on DIV3 or DIV10 for GCaMP6s or on DIV8 for Cre recombinase and control plasmids.

*Transfection buffer composition in mM: 274 NaCl, 10 KCl, 1.4 Na_2HPO_4, 15 Glucose and 42 HEPES at pH 7-7.09.

(2.2.6) HEK293 cultures

HEK293 cells were maintained in E19 plating medium (although this sometimes excluded the anti-microbial components; see Table 2.1) on 10cm cell culture dishes (Greiner Bio-One, #664160). HEK293 cultures were derived from cryostocks (stored at -80°C) consisting of cells (having reached 80% confluence before freezing) suspended in 1ml fetal bovine serum (FBS), 10% dimethylsulfoxide and 10% glycerol. When starting a culture, HEK293 cells were diluted in 10ml E19 plating medium, pelleted and resuspended again in 10ml medium before subsequent pelleting and resuspension to reduce dimethylsulfoxide concentration. The culture was passaged at least once before transfections were applied.

After reaching 70-80% density, cultures were split and the cell suspension diluted by 1:20 for transfection and 1:25 for a subsequent split. Cells were split by first washing the cells with D-PBS (Gibco, #14190-094). The D-PBS was removed and the cells were detached from the culture dish by a two-minute treatment with 1ml of pre-warmed 0.25% Trypsin-EDTA solution in the 5% CO_2 incubator. Cells were collected into a suspension with 10ml pre-warmed E19 plating medium and spun down at 700xg for three minutes. The pellet was resuspended in fresh, pre-warmed E19 plating medium and diluted appropriately.

(2.2.7) Adeno-associated virus production

HEK293 cells were used to generate recombinant chimeric AAV 1 & 2 particles. HEK293 cultures were grown until they reached a density of 60%. A total 64µg of DNA was used for each 10cm dish and consisted of 32µg of pFΔ6 plasmid, 16µg of the expression plasmid (e.g. H2B-GCaMP6s) and

8µg of both the pH21 and pRV1 plasmid. See section 2.3 Plasmids for details about the virus production plasmids. The transfection procedure was similar to the one described in section 2.2.7 with 0.12ml of 2M $CaCl_2$ and 0.96ml of transfection buffer required for each 10cm dish. The final volume of the transfection mix was made up to 1.92ml with autoclaved dH_2O and DNA solution. Prior to addition of the transfection mix, the E19 plating medium was exchanged for fresh, pre-warmed, medium. The transfection mix was applied, dropwise and undiluted, to each dish. The precipitate was left on the cells for 48-72 hours. If the phenol red indicator showed a noticeable acidification, the medium was exchanged for fresh E19 plating medium. Cells were harvested in 0.5ml of D-PBS using a cell scraper and lysed by three freeze-thaw cycles. The lysed cell suspension was spun down at 10,000xg for five minutes and the virus-containing supernatant extracted and stored in a second eppendorf tube at -20°C until required. Prior to routine application of the virus in dissociated neuronal cell culture, different volumes of suspension were added to a dissociated neuronal culture to gauge the appropriate viral suspension needed for complete transduction.

(2.2.8) Lipofectamine transfections

Before discovering that diluting the calcium phosphate transfection mix dramatically reduces its toxicity for dissociated neurons, lipofectamine 2000 (Invitrogen, #11668-019) was used at times when calcium phosphate seemed unreliable. The day before, or a few hours before the procedure, 0.5ml of Neurobasal medium for every, well to be transfected was equilibrated in both the 5% and 10% CO_2 incubators. On the day of the transfection, a lipofectamine solution was prepared by adding 1µl of lipofectamine to 50µl of Neurobasal for every well under transfection. A plasmid solution was made by adding 0.75µg of DNA to 50µl of Neurobasal for each well. Both solutions were left at room temperature to incubate for five minutes. The plasmid solution was then added to the lipofectamine solution and mixed by pipetting. 0.5ml of equilibrated Neurobasal replaced the conditioned medium in each well, which was supplemented, filtered and stored in the 5% incubator. 0.1ml of lipofectamine transfection mix was added to each well and the plate was incubated at 5% CO_2. After two hours incubation time, the cells were washed once with 10% CO_2 equilibrated Neurobasal and then returned to the conditioned medium. These transfections were typically carried out at DIV8-10.

(2.3) Plasmids

Plasmids used for the expression of exogenous proteins in dissociated hippocampal neurons are listed in Table 2.3 along with source information. Adeno-associated virus plasmids are listed in Table 2.4.

(2.3.1) Plasmid amplification

XL1-Blue (Agilent Technologies, #200249) and SURE (Stop Unwanted Rearrangement Events; Agilent Technologies, #200238) electro-competent bacteria cells were used to generate and maintain plasmid stocks. LB medium (Roth, #X968.1) was used to grow electro-competent cells. Cells were prepared following a protocol provided by Oliver Schlüter (European Neuroscience Institute, Göttingen). Briefly, 4 x 500ml bacteria cultures were grown without antibiotics until an OD_{600} of approximately 0.6. Cells were pelleted three times at 8000rpm for 20 minutes and each time two pellets were combined and washed (with resuspension) in ice-cold 500ml dH_2O. After the final wash, the bacteria were resuspended again in 10% glycerol, spun down at 8000rpm and then resuspended in 30ml of 10% glycerol. This 30ml suspension was spun down one final time at 4000rpm and then resuspended in 4ml 10% glycerol, before the bacteria were distributed into 50µl aliquots.

To amplify plasmids, 50µl aliquots of either XL1-Blue (or SURE bacteria for plasmids needed for recombination into virus particles) were slowly thawed on ice until a small volume of plasmid solution (containing between 0.5-1µg DNA) could be mixed easily. The entire 50µl of suspension was added to an electroporation cuvette (Biozym Scientific GmbH, #748010) and a 1800V pulse was applied to transform bacteria. The suspension was diluted with 1ml of LB medium and left to incubate for one hour, shaking at 300rpm. 50-100µl of incubated suspension was then added to a LB-agar plate and left overnight at 37°C. The following morning, a single colony of bacteria was scratched from the agar and added to a starter culture of 5ml LB medium. The starter culture was incubated at 37°C (while shaking) for approximately five hours before being added to 300ml of LB medium, which was incubated overnight or until the OD_{600} reached a value of three or four. Cells were pelleted at 4000rpm at 4°C for 30 minutes and plasmid DNA was isolated using a Macherey-Nagel Nucleobond Xtra Maxi Kit (#740414.5) according to manufacturer's instructions.

(2.4) Recombinant BDNF and pharmacological agents

Recombinant BDNF (rBDNF) was purchased from R&D Systems (#248-BD/CF) and dissolved in PBS (139mM NaCl, 7mM $Na_2HPO_4.H_2O$, 1.2mM $NaH_2PO_4.H_2O$; pH 7.4) containing 0.01% BSA (Roth; 8076.1) at a concentration of 100µg/ml. This recombinant BDNF (~13kDa) was synthesized in *Spodoptera frugiperda (*Sf21) insect cells.

Drugs were prepared in aliquots 100-2000x their working concentration: 50mM D-(-)-2-Amino-5-phosphonopentanoic acid (AP5; Abcam, #ab120003), Bicuculline methiodide (Bic; Abcam,

#ab120108), picrotoxin (Abcam, #ab120315) and 1mM Tetrodotoxin citrate (TTX; Tocris, #1069). 50mM phorbol 12, 13-diacetate (PDA; Enzo, #ALX-445-003-M005) was dissolved in DMSO and then diluted 1:10 with dH_2O. A 10% vehicle control was prepared in parallel.

Voltage-gated calcium channel blockers: nimodipine (Abcam, ab120138), omega-conotoxin-GVIA (Peptides International, PCN-4161-v), SNX-482 (Peptides International, PCB-4363-s), TTA-P2 (Alomone Labs, T-155). Other blockers: TTX (Tocris, 1078), AP5 (Abcam, ab120003).

(2.5) Electrophysiology

Whole cell recordings were performed using an upright Olympus microscope (#BX51WI) and an EPC-10 HEKA amplifier controlled by Patchmaster software. Cells were visualized on a TV monitor through a Hamamatsu CCD camera. Recordings were carried out using standard techniques (Sakmann & Neher, 1995). Briefly, patching micropipettes were forged using a P-97 Sutter Instruments horizontal puller and thick-walled glass capillaries (Harvard Apparatus, #GC150F-7.5). Patch pipettes with resistances of 3-5MΩ were used for forming giga-seals on the plasma membrane before rupturing the patch and commencing the experiment.

Neurons were bathed in artificial cerebral spinal fluid (ACSF) during the experiments, which contained (in mM): 145 NaCl, 2.4 KCl, 10 HEPES, 7 glucose, 2 $CaCl_2$, 1 $MgCl_2$; osmolality 300mosm/kg and pH 7.4. For whole cell recordings without voltage steps (Fig1A-D; section 3.1), the pipette solution contained (in mM): 128 caesium methanosulfonate, 8 CsCl, 10 EGTA, 1 $CaCl_2$, 10 HEPES, 2 Na_2-ATP, 0.3 Na-GTP; osmolality 295mosm/kg and pH 7.3 (LJP measured as +10mV). For whole cell recordings with voltage steps (Fig1E,F; section 3.1): 135 potassium gluconate, 10 NaCl, 0.5 $MgCl_2$, 10 HEPES, 5 EGTA, 1 $CaCl_2$, 2 Na_2-ATP, 0.3 Na-GTP; osmolality 299mosm/kg and pH 7.3±0.02 (LJP calculated as +16.1mV). For perforated patch-clamp recordings (appendix figures), the pipette solution contained (in mM): 135 potassium gluconate, 15 NaCl, 2 $MgCl_2$, 10 HEPES, 3 EGTA, 2.25 $CaCl_2$; osmolality 295mosm/kg and pH 7.2±0.02 (LJP calculated as +10mV).

Liquid junction potentials (LJPs) for the whole cell pipette solution was measured or calculated using Peter Barry's LJP calculator (JPCalcWin). LJPs were compensated for by zeroing the current offset with the command potential set to –(LJPvalue)mV prior to the formation of a gigaseal with the target cell.

Series resistance compensation was applied for experiments described in figure1 A-D (65-92% compensation) and for experiments described in appendix figure 1C (90%). With compensation

applied, access resistance was found to range between 3.5-9.3MΩ. Otherwise, series resistance compensation was not applied. For experiments described in appendix figure 2, the attenuation of somatic voltage compared caused by series resistance of the patch pipette was calculated according to:

$$\Delta V_m = \frac{\Delta V_p R_m}{R_m + R_p}$$

where ΔV_p is the change in command voltage from baseline to the plateau of the voltage ramp. R_m is the membrane resistance and R_p pipette resistance. ΔV_m is the resulting somatic membrane change. If the variables are set such that ΔV_p = 0.1V, R_m = 1.5x10^8 and R_p = 5x10^7 then ΔV_m = 0.075V.

Access resistance for perforated patch recordings ranged between 20-60MΩ and was highly stable. Over the course of one hour recording time change in access resistance did not exceed 25%.

(2.5.1) Pressure application of rBDNF

Pressure application of recombinant BDNF (rBDNF) was carried out using a npi pressure application system (#PDES-DXH) controlled by TTL pulses from the EPC-10. Thin-walled glass capillaries (Harvard Apparatus, #GB150TF-8P) were used to forge the pressure application micropipettes with a resistance of 1-2MΩ. These pipettes were filled with 2µl of 100µg/ml rBDNF solution and positioned 0.4-1mm distant from the target cell. It was estimated that 60 seconds of ejection time was needed to completely expel at least 2µl of solution from a 1-2MΩ pipette. A constant volume of approximately 2ml ACSF in the chamber was maintained throughout. This produced a final concentration of at least 100ng/ml BDNF in the recording chamber.

A dissociated hippocampal neuron (DIV13-17) expressing GFP under the CaMKIIα promoter was selected as the target cell. I calculated the exact vertical and horizontal distances needed to move the pipette away from the cell, given the angle between the shaft of the pressure application pipette (PAP) and the tabletop, which would mean that the tip was pointing directly at the target cell at a distance of 0.4mm (or, in a few cases, 1mm). With the PAP in place, the target neuron was patched and held in voltage-clamp at -70mV. Access resistances were compensated between 65-92%. With compensation applied, access resistance was found to range between 3.5-9.3MΩ. Access resistance was measured by dividing the amplitude of a 5mV test pulse by the peak amplitude of the resultant slow capacitance current according to Ohm's Law: Resistance = voltage / current

(2.5.2) Lightspot stimulation experiments

In order to optically evoke action potentials in dissociated neurons, the upright Olympus microscope was upgrade to hold a Cairn infinity pathway with a 400µm pinhole drop-in unit (Acal Bfi GmbH; Cairn Research, UK) and an LED light source. The 400µm pinhole was found to deliver a lightspot approximately the same size as a cell body, which appropriately limits the stimulation to a single CheRiff-expressing neuron.

Dissociated neurons were transduced with AAV8-CheRiff-EGFP, which was provided by Oliver Schlüter (ENI, Göttingen) typically on DIV3. Between DIV13-17, most neurons could produce evoked action potentials with a fraction of the LED's maximum power. 10ms light pulses were controlled via TTL inputs from the EPC-10 to the OptoLED control box/power supply (#P1110/001/000).

Amphotericin B was used as the pore forming compound to achieve perforated patch-clamp recordings. I followed methods described elsewhere with modifications (Rae *et al.*, 1991). Briefly, amphotericin B was dissolved to 66mg/ml in DMSO (or 15µl DMSO per mg amphotericin B) and then diluted in pipette solution to a final concentration of 400µg/ml (or 3µl of 66mg/ml solution to 500µl pipette solution). The pipette tip was filled with perforant-free pipette solution and then the pipette was backfilled with solution containing 400µg/ml amphotericin B. Rae *et al.* (1991) recommended only dipping the tip of the pipette into the perforant-free solution for a few seconds. In my hands, this approach meant no positive pressure could be applied during the final approach to the target cell and resulted in a low success rate. Applying positive pressure meant amphotericin would reach the tip and interfere with seal formation. Not applying pressure meant that extracellular debris that often covered the cells could not be cleared. I found a more successful approach to involve backfilling the tip with perforant-free solution and then extract as much of the solution as was possible with a microloader tip (Eppendorf, #5242 956.003). A very small amount of clear solution would always be present in the tip, but this would be sufficient to allow positive pressure to be applied during the final approach to the cell without amphotericin reaching the tip. 30 minutes to one hour was required for maximal perforation.

After forming a successful perforation, single light pulses were triggered in quick succession and different neurons in the vicinity of the perforated cell were checked for connections. In some cases, cultures were treated with 20µM picrotoxin for several days prior to the experiment to reduce spontaneous activity. This aided in the identification of evoked EPSCs because high levels of spontaneous activity could occlude the evoked response. Treating dissociated neurons with

$GABA_A$ receptor antagonists is known to trigger a homeostatic response that weakens excitatory synapses (Turrigiano *et al.*, 1998).

(2.6) Imaging

To image calcium transients in dissociated hippocampal neurons, I used an Evolve 512 EMCCD camera (Photometrics) mounted on a Zeiss Ax10 inverted microscope. The fluorescent light was produced by a Lambda DG-4 illumination system (Sutter Instrument). Experiments were carried out in either a Warner Instruments low profile recording chamber (#RC-40LP or RC-41LP) or using a custom-built field stimulation chamber with parallel platinum electrodes following a similar design. MetaMorph (64-bit) was used to acquire timelapse images. The GFP-based genetically encoded calcium indicator, GCaMP6s, was always used for calcium imaging experiments, so the appropriate GFP excitation and emission filters were used.

When imaging calcium transient across multiple cells, a 10x or 20x magnification objective was used to acquire images at a rate of 2.5Hz with 100ms exposure time. The same acquisition settings were used to acquire spontaneous spine calcium transients at 100x magnification, except when pressure applying rBDNF or imaging these transients in order to measure their amplitudes. In these cases, calcium transients were imaged at 20Hz with 50ms exposure time.

(2.7) Data analysis

This section describes all data analysis techniques except those involving AARG analysis. For a description of AARG analysis see section 2.8.

All data processing and analysis was carried out using Igor Pro (version: 6.34A) or Matlab (version: 2013a/2014b/2015a). Pearson's linear correlation coefficient was calculated using the built-in Matlab function: corr. Wilcoxon rank sum test was carried out using the built-in matlab function: ranksum. Two-sample Kolmogorov-Smirnov test was applied using the built-in matlab function: kstest2. One-way ANOVA was applied using 'anova1' and multiple comparison tests were done using 'multcompare'. Standard confidence limits of 95% were applied.

(2.7.1) Analysis of somatic calcium transients

Matlab scripts were written to analyze somatic calcium transients in response to recombinant BDNF application.

Raw TIF files contained fluorescence signals from histone-tagged GCaMP6s (H2B-GCaMP6s) response to rBDNF application and 40mM KCl washin. These images were converted to MAT files. 40mM KCl MAT files were thresholded by taking the standard deviation of each pixel/element over time. The lowest threshold combination giving the clearest outline of the cells was used as a mask to judge the appropriate placing of 5x5 ROIs. The Matlab scripts first attempted to apply regions of interest (ROIs) to the cell bodies without user intervention. ROIs could be placed inappropriately, particularly when cell bodies appeared close together and the suprathreshold signals for the cells would fuse. In such cases, ROIs were deleted and manually replaced with one or more ROIs judged to be more appropriately overlapping with cell bodies (brightfield images of the cells and timelapse images of field stimulation responses were used to aide this judgement). After satisfactory placement of ROIs, raw fluorescence signals from the rBDNF response MAT files were converted to ΔF/F values for each ROI (see section 2.7.2 for calculations; equations are numbered). Assuming at this stage that each ROI represents the cell body of a single neuron, each cell was defined as responding to rBDNF if ΔF/F for the current ROI exceeded the sum of shifting baseline ΔF/F and the rate of change in ΔF/F. If this threshold was surpassed, then the signal also needed to be maintained for a fixed number of frames (see section 2.7.2 for details). The matrices containing the suprathreshold rBDNF data for the ROIs were transformed and projected to a 2D image.

For experiments testing the dependence of somatic calcium transients on TrkB expression, movie images with rBDNF application and 40mM KCl washin were manually inspected. Transfected (mCherry+) neurons were judged to be responding or not responding to 40mM KCl stimulation and/or rBDNF application. Thus, in these experiments, cells were placed into one of three categories: non-responsive, responding only to 40mM KCl or responding to both 40mM KCl and rBDNF.

(2.7.2) Calculations: somatic calcium transients

For all 25 pixels within each ROI, ΔF/F values were calculated as follows:

$F_i = \text{median}(q_1 \ldots q_n)$

$\Delta F_i = q_t - F_i$

where N is the number of frames in a single experiment (typically N = 750), i is the current pixel and q is the raw fluorescence value for the current pixel in a single frame (t).

Final ΔF/F values for each frame were calculated as the mean of 25 pixels within each ROI:

$$\Delta F / F = \sum_{i=1}^{n} \frac{(\Delta F_i / F_i)}{n} \quad \textbf{(1.0)}$$

n = number of pixels in ROI = 25

F_B and F_R are shifting average values of the ΔF/F baseline and first derivative values respectively and are defined as:

$$F_B = \sum_{t=j}^{N} \frac{([\Delta F / F]_t)}{n_B} \quad \textbf{(1.1)}$$

N = current frame – 1

j = current frame – n_B

n_B = 3.2 x frame rate

$$F_R = \sum_{t=j}^{N} \frac{([\Delta F / F]_t - [\Delta F / F]_{t-1})}{n_R} \quad \textbf{(1.2)}$$

N = current frame – 1

j = current frame – n_R

n_R = 1.2 x frame rate

where $[\Delta F/F]_t$ is the ΔF/F of frame t, which is within range of the current frame. These ranges are defined by the values n_B and n_R. The constants 3.2 and 1.2 were determined through trial and error testing. The chosen constants gave a very reasonable threshold output as shown in figure 2A,B. The same values were applied to all experiments included in analysis.

In order to pass threshold, ΔF/F value for the current frame needed to exceed (F_B + F_R) and surpass or equal the shifting average ΔF/F value for n_A frames in front of (i.e. further in time) the current frame. This last shifting average value of ΔF/F is defined as:

$$F_A = \sum_{t=j}^{N} \frac{([\Delta F / F]_t)}{n_A} \quad \textbf{(1.3)}$$

N = current frame + n_A

j = current frame

n_A = 1.6 x frame rate

As with n_B and n_R, the constant '1.6' was determined through trial and error and the same value was used for all analysed data. I reduced the threshold constants until suprathreshold activity (black and white images in Fig2A,B) overlapped reasonably well with the $\Delta F/F$ signal (see Fig2).

In addition, F_R had to exceed an 'activity threshold'. As with the other threshold constants, this was the lowest value which produced reasonable overlap between suprathreshold signal. By default, this value was set to 0.03. This value was changed to 0.82 for experiments described in figure 3 (section 3.1). The fluorescence intensity increases following application of Na/citrate solution (see figure 3) seemed to have slower rates of change compared to fluorescence intensity increases following rBDNF application. Thus, adjusting the activity threshold seemed to be the most likely means of excluding non-specific fluorescence intensity increases caused by high ion concentrations in the pipette.

(2.8) Activity- based Automatic Region of Interest Generation (AARG) analysis

(2.8.1) AARG thresholds for slow frame rate acquisition and ROI placement

Michael Siebrecht wrote Matlab functions to convert TIFF files to MAT files and count the overall number of events. These functions were: 'tif2mat' and 'openTifStack'. I relied on these functions for most data analyses in Matlab, although the functions required extensive modification. Michael Siebrecht also created other functions, which I used to create my own functions – either by modifying the code directly or using the same techniques. These functions were (original names used by Michael Siebrecht): 'AnalyseBatchOfExp', 'AutoRoiTS', 'Exp2Freq' and 'plotCaResults'. Some other Matlab functions were written by third parties and are freely available to download from the Matlab File Exchange webpages. These functions included: 'uipickfiles', 'heatmap' 'getline' and 'dispstat'. In some cases, I made minor modifications to third party scripts.

AARG automates the process of defining regions of interest (ROIs). Michael Siebrecht found that by combining what he termed Activity and Size thresholds, discrete spine calcium elevations could be extracted from the data. The approach was similar to the one applied by Kleindienst *et al.* (2011). The Activity threshold is applied to Matlab matrices generated by extracting the difference in the normalized fluorescence intensity profile for each pixel between each frame. Connected pixels above the Activity threshold having a collective size below the Size threshold are then filtered out. If either threshold is set too low, noise will contaminate the suprathreshold matrices and be clearly visible in background regions of maximum projection images overlaying an outline of the cell and the suprathreshold signal (see figure 5).

It is necessary for the user to find the appropriate Activity (or rate of change in fluorescence intensity) and Size threshold combination for the current data set. This will usually be the lowest combination producing a maximum projection image containing no background noise and is determined by visual inspection. The lowest threshold combination is found by initially applying a range of increasing threshold combinations. A Size threshold with no background noise is then fixed while a range of Activity thresholds are tested. Likewise, an Activity threshold that is known to produce no background is selected and combined with small increases in size. By alternately adjusting these two thresholds, the user is more likely to identify a threshold combination closer to the signal-noise limit. The scripts require Matlab 2014b or later (recommended 8GB RAM).

3x3 ROIs were placed over the centre of mass of suprathreshold pixel clusters (events). When ROIs overlapped, the ROI belonging to the largest event took precedence (unless the smaller event occurred in a preceding experimental condition). ROI placement is described in more detail in section 3.2.1.

(2.8.2) Shift correction

The extent of lateral shift along the X and Y axes was measured for each experiment involving application of voltage-gated calcium channel antagonists. If a shift of more than 3 pixels along either axis was detected between the reference image and the last data chunk (500 frames) of the same experiment, a correction procedure was applied. In 78% of measurements, frame shift was less than one pixel along the X or Y axis. Cross-correlation analysis was applied to detect lateral shift and corrected with Fast Fourier Transform if necessary. Shift detection and correction algorithms were provided by Dr Guobin Bao.

(2.8.3) AARG thresholds for fast frame rate acquisition

For frame rates of 20Hz I found that the Activity and Size threshold combination resulted in an unacceptably high level of false-negatives (i.e. too many real events were missed) when the thresholds were set high enough to exclude noise. It was necessary to maintain higher frame rates such that the amplitudes of spontaneous spine calcium transients (SSCTs) could be more accurately measured. Therefore, it was necessary to change my method for thresholding timelapse images.

Dr Guobin Bao provided me with the matlab and C++ functions that enabled me to greatly reduce the number of false-negatives while excluding noise artifacts. These functions enabled me to

incorporate a seven-stage thresholding algorithm into the AARG analysis procedure. These stages are described in the rest of this section and are summarized in methods figure 1.

Converting to MAT, binning, bleach correction and smoothing (methods figure 1A,B): During acquisition, Metamorph automatically splits a single 12000-frame experiment (duration: 10 minutes; acquisition rate: 20Hz) into 3 files consisting of approximately 4000 frames each. These files are chunked during TIFF-to-MAT file conversion into ~500-frame segments. This step was necessary in order to carry out analysis using Matlab on standard computers (RAM: 4-8GB; Processor: 2.4-2.8GHz multicore processor). In order to further limit computational demands, each timelapse movie was binned along the first and second dimension reducing each 512x512x500 chunk to 170x170x500 chunks. Although GCaMP6s exhibits very stable fluorescence even with continuous imaging (Chen *et al*, 2013), bleaching of the calcium signal was often noticeable. Bleaching compensation was applied by removing a single exponential decay occurring over the time course of the current data chunk. High-pass spatial filtering was applied across $\sigma \approx 1.7$ (Gaussian filter, $\sqrt{3} \approx 1.7$; where 3 is the side length of each ROI) to reduce single pixel noise.

Normalization and background subtraction with neighborhood correlation mask (method figure 1C,D): Each pixel is normalized such that the mean of the normalized raw fluorescence signal equals zero and the variance of the normalized data equals 1. This step is necessary for the background subtraction procedure to be valid (section 2.8.4) and prevents errors during calculation of cross-covariance. Background signal can be removed by decorrelating real fluorescence signal and background if these signals contribute independently to overall pixel intensity. Background (B) could be removed from the overall pixel signal (P) according to: A=P-k*B (see section 2.8.4 for more details). With background subtracted from normalized fluorescence signal, the correlation of each pixel with its immediate neighbors over time was calculated. Any pixels with a neighborhood correlation less that 3x standard deviation above the mean was excluded from further analysis, which reduces computational demands.

Event detection (method figure 1E-H): Cross-correlation coefficients (COR) were calculated for each pixel exceeding the neighborhood correlation threshold. In order to compute the COR, the cross-covariance coefficients (COV) were first computed. COV can be defined in the general form (see equation 3.0 and 3.1 in section 2.8.4), but was calculated according to Fast Fourier Transformation to allow efficient calculation of large data loads. In equations 3.0 and 3.1, A and B are two independent variables equivalent to the template values (from template calcium traces – see methods figure1E) and pixel values (normalized, background subtracted values), respectively. Templates are functions modelling one dimensional SSCTs. COV is calculated by crossing normalized, background subtracted data with template values. COR is defined as the COV divided

by the standard deviation of the pixel data across time (equation 3.2). Crossing COV and COR yields the final coefficients (E) which were evaluated with a threshold value: 5. To further filter out noise, the normalized, background subtracted pixel value had to also exceed 3.5 (methods figure 1G,H). These thresholds (5 for E values and 3.5 for data values) were applied to all data in this way before the automatic ROI placement algorithm was applied.

(2.8.4) Calculations: AARG thresholds for fast frame rate acquisition

Background subtraction and event detection used cross-covariance and cross-correlation calculations to optimize automated event detection.

Background subtraction:

Accurate global background subtraction increases the accuracy of the neighborhood correlation and cross-correlation calculation for each pixel based on the normalized fluorescence intensity. The pixel signal (P) is composed of the real signal (A), background signal (B) and the covariance between P and B, k:

P=A+kB,

k=Covar(P,B).

Proof that Covar(P,B) = k

If means of P, B and A = 0

Covar(P,B) = Covar(A+kB,B) = Covar(A,B)+Covar(kB,B)

Covar(kB,B) = k*Covar(B,B) = k*var(B)

If var(B) = 1

where var(B) is the variance of variable B

Covar(P,B) = Covar(A,B) + k **(2.0)**

If A and B are independent, Covar(A,B) = 0

So, Covar(P,B) = k

Background subtraction is performed according to: A=P-Covar(P,B)*B **(2.1)**

Covariance of P and B is defined as the correlation between the matrices of mean subtracted input data (represented by P) and the mean subtracted background signal (represented by B).

Event detection:

The general form of the cross-covariance function, which finds the covariance between two signals (or in this case a signal and a template signal) and can be defined as:

$$COV_{AB}(i) = \sum_{t=1}^{N}[(A_t - \mu_A)(B_{t+x} - \mu_B)] \quad \textbf{(3.0)}$$

where A is the template trace (consisting of 37 points – equivalent to 37 frames) and B is the current data chunk consisting of ~500 frames. μ is the mean of A or B. This can be simplified to:

$$COV_{AB}(i) = \sum_{t=1}^{N}[(A_t)(B_{t+x})] \quad \textbf{(3.1)}$$

because in the normalized data used in the current analyses μ = 0.

N is the number of points in A (N = 37; methods figure 1E). 'i' is the current pixel in B. x defines the exact location of B along the 500 frames of the current data chunk. Calculations described by equations 3.0 and 3.1 are carried out by Fast Fourier Transform for computational tractability

A is the template function modelling single SSCTs defined by:

$$y = e^{(-t-1)/tau}$$

the range of templates is defined by the tau values: [170, 75, 45, 30, 20, 14, 10, 7, 5, 3, 1.7, 0.7]. Meaningful COV values cannot be calculated for the last 36 frames if N = 37, so these values are set to 0. The template is 37 frames, while B is a data chunk consisting of 500 frames.

$COR_{AB}(i)$ is used to derive the final cross-coefficient value, which is defined as:

$$COR_{AB}(i) = \left(\frac{COV_{AB}(i)}{N}\right)\frac{1}{\sigma_B} \quad \textbf{(3.2)}$$

$$E_{(i)} = COV_{(i)} \times COR_{(i)} \quad \textbf{(3.3)}$$

where σ_B is the standard deviation of the current pixel across time in the current data chunk.

(2.8.5) Detecting SSCT peaks and measuring fluorescence signal intensity changes

The Activity and Size threshold used to detect events in an earlier version of the AARG program (section 2.8.1) has been replaced with the procedure outline in sections 2.8.3-2.8.4. This was necessary to improve event detection in data acquired at faster frame rates. In this updated

procedure, thresholds must be found for the E-value and normalized fluorescence intensity amplitude instead of the rate of raw fluorescence signal change (Activity) and clustering of suprathreshold pixels (Size). Although an updated thresholding procedure is being used, AARG analysis can still identify ROIs by comparing event sizes and overlaying ROIs with centres of mass of the suprathreshold pixel clusters (i.e. events).

During the ROI placement procedure, the spread of each event (i.e. the number of suprathreshold pixels) in every frame is collected. In addition, local maxima of fluorescence intensity are detected during each event. These two variables – event spread and local maxima of fluorescence intensity – are combined to aide detection of peak fluorescence intensities. This approach assumes that peak amplitudes are likely to overlap in time with the point of maximum event spread. Peak amplitudes are also likely to be a local maximum (although multiple local maxima can be reasonably detected within a single event). Thus, the peak amplitude location can be accurately predicted by identifying the local maxima overlapping with the largest amount of event spread.

The spread of all events at each time point was collected. If a gap of more than 400ms occurred between two measures of event spread then the current point was treated as a new event. This produced discrete clusters of event spread data for each ROI and enabled identification of single events for which a single peak intensity amplitude needed to be found. The local maxima with largest event spread provided the provisional location for peak fluorescence intensity. The baseline was provisionally identified as the frame immediately preceding the frame that first contained the initial part of event spread.

Final baseline and peak amplitude locations were found by taking a segment of the normalized, background subtracted fluorescence intensity signal. The segment started 1.5s (or 30 frames for 20Hz acquisition) before the time point of the provisional baseline and 1.5 seconds after the provisional time point of the peak amplitude. The normalized fluorescence signal was averaged across 9 pixels of the current 3x3 ROI for the time course of the segment to produce a fluorescence signal trace. The lowest three values of the trace were averaged and the highest three values were averaged to yield the final baseline and peak amplitude values, respectively.

A 3x3 ROI in a 170x170 image binned from a 512x512 image is equivalent to a 9x9 ROI in the original 512x512 image. In a 512x512 image, there are 6.25 pixels/µm, meaning that a 3x3 ROI in a 170x170 image will cover an area of 1.44x1.44µm (approximately 2µm^2).

(2.8.6) Connecting ROIs to dendrites

I modified the third-party matlab function, ‘getline’, to manually draw vectors along dendrites connected directly to the cell body or to another vector outlining a parent dendrite. Vectors connecting ROIs with parent dendrites were constructed automatically for any ROI within 5µm of a possible parent dendrite. The algorithm automatically constructed vectors by starting at the edge of the ROI closest to the nearest potential parent dendrite and selecting neighboring pixels with the highest fluorescence intensity signal as part of the vector. By constructing vectors along neighboring pixels with the highest fluorescence intensities, each vector approximates location of the spine neck when ROIs overlap with spine heads several pixels distant from the nearest point on manually drawn vector tracing the middle of the dendrite. Neighboring pixels further away from potential parent dendrites were de-selected. This process continued until the vectors for the current ROI and parent dendrite intersected. At this point the current ROI was assigned its parent dendrite.

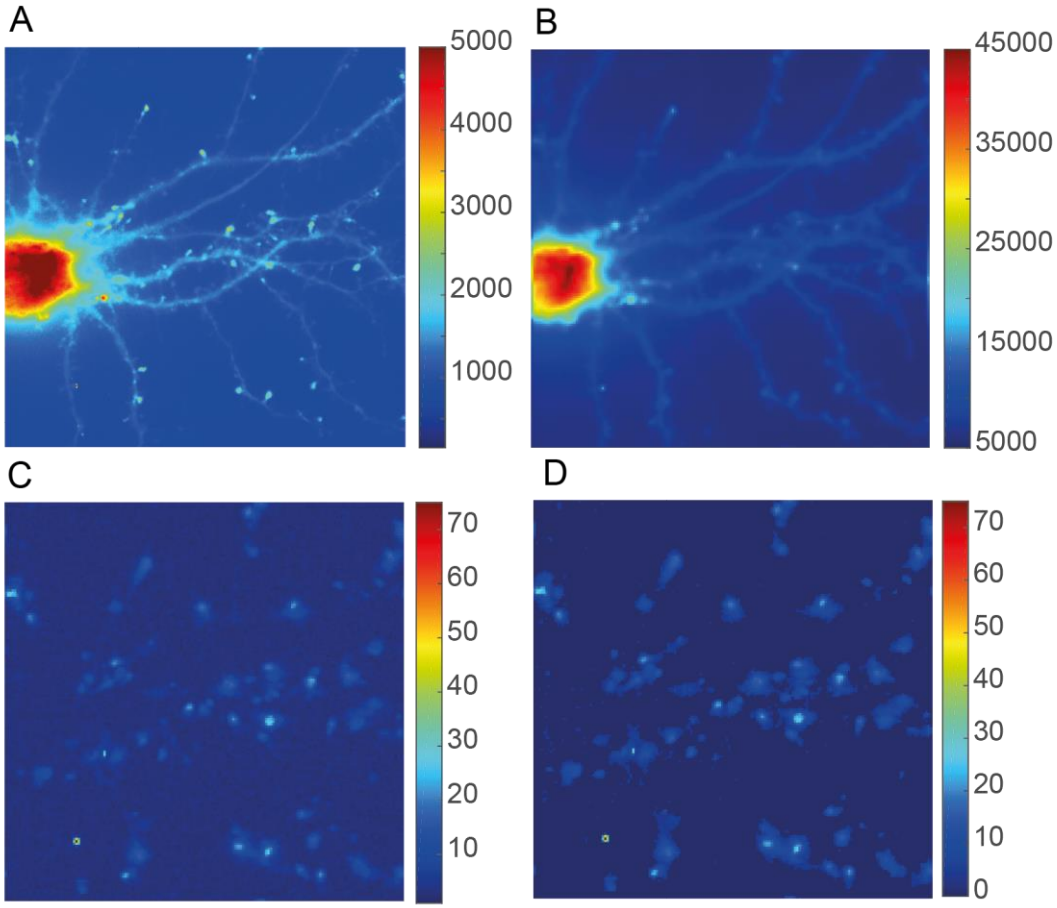
A
5000
4000
3000
2000
1000
B
45000
35000
25000
15000
5000
C
70
60
50
40
30
20
10
D
70
60
50
40
30
20
10
0
E templates
6
5
4
3
2
1
0
-1
-2
-3
0
5
10
15
20
25
30
35
40
F cross-correlation
400
350
300
250
200
150
100
50
0
G E-value ≥ 5
H E-value ≥ 5
pixel values in (C) > 3.5

Methods Figure 1: Thresholding spontaneous spine calcium transients. (A) *Maximum projection image of 503 frames of raw data converted to MAT file.* ***(B)*** *Same image as in A after binning, correcting for signal bleaching and high-pass spatial filtering across 1.7 pixels in the first and second dimensions.* ***(C)*** *Same data chunk after normalization and background subtraction.* ***(D)*** *Signal with neighborhood correlation threshold mask applied; only pixels containing signal 3x standard deviation above mean neighborhood correlation is included in further analysis.* ***(E)*** *Event templates used in cross-covariance calculations. The x-axis is equivalent to frame number. The y-axis is equivalent to the normalized, background fluorescence intensity values shown in C and D.* ***(F)*** *E coeffients (see equation 3.3) calculated for all pixels not excluded by the neighborhood correlation mask.* ***(G)*** *Pixels with E-values ≥ 5 are shown in white.* ***(H)*** *Excluding pixels with normalized, background subtracted intensity values (those in C) less than 3.5 applied in combination with the E-value threshold.*

Table 2.1: Medium formulations for E19 dissociated hippocampal cultures

Medium	**Component**	**Working concentration**	**Company/ Catalog no.**
E19 Dissection medium	HBSS		Gibco/14170-088
	HEPES (1M)	10mM	Gibco/15630-056
E19 Plating medium	DMEM with GlutaMax		Gibco/31966-021
	FBS	10%	Gibco/10500-064
	Penicillin-Streptomycin 10,000 units/ml	100 units/ml	Gibco/15140-122
Feeding medium	Neurobasal medium		Gibco/21103-049
	B-27 Supplement	1ml/50ml	Gibco/17504-001
	GlutaMax (200mM)	2mM	Gibco/35050-038
	Penicillin-Streptomycin 10,000 units/ml	100 units/ml	Gibco/15140-122

Table 2.2: Medium formulations for P0 dissociated hippocampal cultures

Medium	Component	Working conc/amount	Company/ cat. no.
Enzyme solution	L-Cysteine	2mg	Sigma/168149-25G
	Dissection medium	10ml	
	Na-EDTA pH8	0.1ml	
	2M $CaCl_2$	5µl	
	1500 units/ml DNase I	0.1ml	Roche/10104159001
	Papain	0.1ml	Worthington(LS003126)
Inactivation solution	Serum medium	10ml	
	Bovine serum albumin	25mg	8076.1 (Roth)
	1500 units/ml DNase I	0.1ml	Roche/10104159001
P0 Dissection medium	HBSS	500ml	Gibco/14170-088
	1M HEPES	5ml	Gibco/15630-056
	1M $MgCl_2$	5ml	
	2M $CaCl_2$	0.375ml	
P0 Plating medium	Neurobasal medium	47.75ml	Gibco/21103-049
	B27-supplement	1ml	Gibco/17504-001
	Penicillin-Streptomycin 10,000 units/ml	0.5ml	Gibco/15140-122
	Glutamic acid + aspartic acid	0.25ml	
	GlutaMAX	0.5ml	Gibco/35050 – 038
Serum medium	DMEM with GlutaMAX	46.4ml	Gibco/31966-021
	Penicillin-Streptomycin 10,000 units/ml	0.5ml	Gibco/ 15140-122
	Mito+ serum extender	0.1ml	
	Vitamins	0.5ml	Gibco/11120-037
	Fetal bovine serum	2.5ml	Gibco/10500-064

Table 2.3: Plasmids

Plasmid name/ protein of interest	Promoter	AAV vector	Provider	Affiliation
CheRiff	synapsin	Yes	Ed Boyden	MIT, USA
ChR2 (E123T/T159)	CaMKIIα	Yes	Karl Deisseroth	U. Stanford/HHMI, USA
EGFP	CaMKIIα	No	Thomas Dresbach	U. Göttingen, Germany
GCaMP6s	CaMKIIα	Yes	Mark Schnitzer	U. Stanford
H2B-GCaMP6s	synapsin	Yes	Loren Looger	Janelia Farm, USA
mCherry-Cre	synapsin	Yes	Bryan Roth	Chapel Hill, USA
mCherry	synapsin	Yes	Sebastian Kügler	U. Göttingen, Germany

Table 2.4: Virus plasmids

Plasmid	Description	Provider	Affiliation
pH21	Serotype 1 replication and capsid sequences	Moritz Rossner	Psychiatric Clinic, U. Munich
pRV1	Serotype 2 replication and capsid sequences	Moritz Rossner	Psychiatric Clinic, U. Munich
pFΔ6	Adenovirus helper plasmid	Susanne Schoch McGovern	University Hospital of Bonn, Germany

Results

(3.1) Membrane currents and somatic calcium elevations in response to exogenous brain-derived neurotrophic factor (BDNF) application

(3.1.1) Current responses to recombinant BDNF application

Endogenous BDNF expression is necessary for complete expression of LTP (Patterson *et al.*, 1996; Figurov *et al.*, 1996; Korte *et al.*, 1996). Applying recombinant BDNF to final concentration of 100ng/ml has been consistently reported to evoke a transient increase in the frequency of miniature excitatory currents (mEPSCs) (Magby *et al.*, 2006; Amaral & Pozzo-Miller, 2012). TrkB receptors – the BDNF receptors which must be activated for BDNF to facilitate LTP (Minichiello *et al.*, 2002) – are expressed both presynaptically and postsynaptically, which could lead to recombinant BDNF (rBDNF) altering release probability or unsilencing synapses through a postsynaptic mechanism. Due to the lack of spatial information in patch-clamp recordings, previous findings (Lohof *et al.*, 1993; Magby *et al.*, 2006; Amaral & Pozzo-Miller, 2012) could not definitively conclude whether rBDNF activated presynaptic, postsynaptic TrkB receptors or both. Determining which of these receptor populations are activated by rBDNF would be an important step in understanding how endogenous BDNF promotes LTP expression. Measuring changes in frequency of spontaneous synaptic calcium transients (SSCTs) at individual spines would be a means of gathering functional data while preserving necessary spatial information to gain insights into this protein's mode of action in facilitating LTP.

Initially I sought to replicate findings reported by Amaral & Pozzo-Millar (2012). These authors pressure applied 100µg/ml rBDNF solution to a final concentration of 100ng/ml in the recording chamber, while recording in whole cell voltage-clamp configuration and blocking action potential activity with TTX. Amaral & Pozzo-Miller (2012) recorded from CA1 neurons in organotypic slice cultures. All the experiments described below were carried out with dissociated rat hippocampal neurons between day in vitro (DIV) 13-19, unless otherwise specified. 100µg/ml rBDNF was pressure applied using 1-2MΩ micropipettes for 60 seconds with the tip placed 0.4mm from the recorded cell with 10µM bicuculline and 0.5-1µM TTX washed into the chamber. 60 seconds was the approximate time required for 2µl of solution to be ejected from the pipette into a chamber containing 2ml bath solution. Of 29 recorded cells, approximately 50% show no obvious current response to 60 seconds rBDNF application, however in some case there is a noticeable inward current typically occurring just after rBDNF application was complete (Fig1A,B). Occasionally, the tip of the pressure application pipette would become clogged with precipitated protein or salts, which could also inhibit an evoked response. In the experiments included in figure 1, pipette tips were inspected for tip blockages. Experiments are discarded in cases of pipette blockages. This

inward current could arise from widespread presynaptic release if rBDNF binds to TrkB receptors located on presynaptic terminals. In some cases, there is a clear transient decrease in mEPSC frequency following return of the current signal to baseline (Fig1A, insets). This could reflect a brief decrease in release probability following widespread synaptic vesicle fusion. However, the inward current is unlikely to arise due to such a mechanism because the transient decrease in mEPSCs do not consistently correlate with event peak amplitudes (Fig1C) and very small currents approaching the expected peak amplitude of mEPSPCs still have very slow rise times (Fig1D). The inward current, with highly variable peak amplitudes, detected here seems to reflect a postsynaptic response.

Voltage-steps revealed an outward current component starting during rBDNF application when the voltage command steps to more depolarized potentials (Fig1E,F). Similar to the inward current component, the outward current also has highly variable amplitudes. The inward current decreases in amplitude with progressively more positive voltage commands – possibly due to a combination of a reduction in driving force and shunting from the outward current. Cesium methanosulfonate-based internal solution was used with for initial experiments without voltage steps (Fig1A-D), while the experiments reported in figure 1E used potassium gluconate-based internal solution and a smaller chamber (hence only five seconds pressure application).

Apart from papers reporting transient increases in mEPSC frequency, other reports have suggested that inward current responses to rBDNF depend on TTX-resistant channel Nav1.9 (Blum *et al.*, 2002) or TRPC3 (Li *et al.*, 2010) channel activation. Nav1.9 channels open between approximately −20 and +30mV (Akopian *et al.*, 1996) and for this reason alone are unlikely to account for inward currents measured in cells held at −70mV.

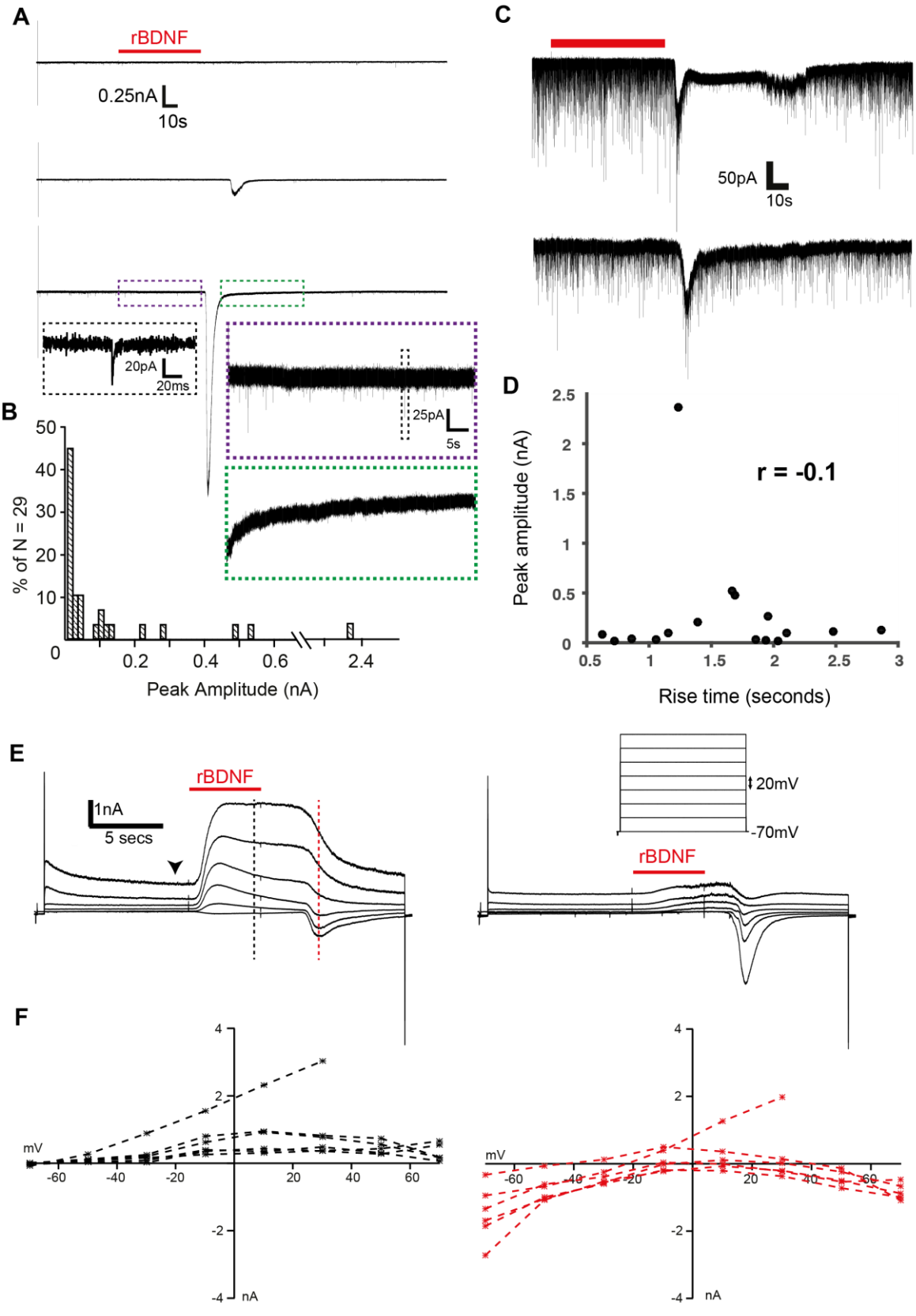
A
rBDNF
0.25nA
10s
20pA
20ms
25pA
5s
B
% of N = 29
Peak Amplitude (nA)
C
50pA
10s
D
Peak amplitude (nA)
r = -0.1
Rise time (seconds)
E
rBDNF
1nA
5 secs
20mV
-70mV
rBDNF
F
mV
nA
mV
nA

Figure 1: Inward and outward current responses to recombinant BDNF (rBDNF). (A) *Current responses to pressure application of rBDNF (red bar) from CaMKIIa-EGFP-expressing dissociated hippocampal neurons (DIV13-17). 100µg/ml rBDNF solution was ejected into the recording chamber for one minute from a glass pipette with its tip positioned 0.4mm (diagonal distance) from the cell. The duration of application and the volume of bath solution in the chamber (2ml) should produce a final concentration of approximately 100ng/ml. In most cases, neurons show no obvious response (top trace), while in others, a small inward current is detectable (middle trace). In a small number of cases, neurons respond to rBDNF application with a large delayed inward current (bottom trace). Insets: miniature excitatory postsynaptic currents (mEPSCs) (black dashed box).* ***(B)*** *Frequency histogram showing the distribution of peak amplitudes. In approximately 50% of cases, neurons show no response.* ***(C)*** *Two different neurons with similar inward current peak amplitudes. Top trace shows marked transient reduction in mEPSC frequency, while the lower trace does not.* ***(D)*** *There is no correlation between inward current amplitude and rise time of the current. Rise times should approach mEPSC rise times as peak amplitudes decrease if the inward currents are triggered by presynaptic vesicle fusion.* ***(E)*** *Voltage steps during pressure application revealed an outward current response with an onset during pressure application of rBDNF. Left, example experiment with dashed vertical lines indicating where the current response was sampled to plot current-voltage curves in F. Right, voltage step protocol applied to a total of six experiments and a second example with six voltage steps and a much smaller outward current component. Black arrowhead indicates sampling point for measuring the baseline of the current response* ***(F)*** *Current-voltage curves for all six experiments for outward currents (left, black dashed lines) and inward currents (right, red dashed lines). Experiments in A-D used a cesium methanosulfonate-based internal solution. Experiments in E and F used a potassium gluconate based internal solution.*

(3.1.2) Somatic calcium responses to rBDNF

Inward currents such as those described in figure 1, are likely to trigger measureable somatic calcium elevations. Using histone-tagged GCaMP6s under the synapsin promoter (H2B-GCaMP6s), I measured somatic calcium transients in response to repeated 100µg/ml rBDNF application. In these experiments, 100µg/ml rBDNF was applied for five seconds using 1-2MΩ pipettes. The volume in the chamber ranged between 200 and 600µl. Repeated applications of 100µg/ml rBDNF revealed that most neurons (transduced with H2B-GCaMP6s-containing AAV particles) responded to all three rBDNF applications within 5-20 seconds after start of each application (Fig2A). This onset time matches that of the inward current described in figure 1, which is consistent with these somatic calcium transients being triggered by those same currents. Somatic calcium transients with this onset time are also highly sensitive to blockade of voltage-

gated calcium channels (Fig2B) – this finding further supports the view that inward currents measured in figure 1 create membrane depolarizations leading to the activation of calcium channels along the plasma membrane.

It is unlikely that some of the larger inward currents reported here occur under physiological conditions. For this to happen, rBDNF would have to be released simultaneously and bind to receptors across large areas of the neuron's plasma membrane (for instances where the current is measured in the nanoampere range). Nevertheless, the range of inward current amplitudes could reflect an interesting physiological property of hippocampal neurons – namely that TrkB receptors are being expressed at the plasma membrane surface at different concentrations in different cells. TrkB surface expression is known to be influenced by activation of purinergic receptors (Lee & Chao, 2001; Assaife-Lopes *et al.*, 2014) and other tyrosine kinase receptors (Puehringer *et al.*, 2013). The presence of surface TrkB receptors at spines could be a crucial factor affecting the kind of plasticity the respective synapses can undergo.

A critical experiment is to test the dependence of somatic calcium transients on TrkB expression. Floxed-TrkB mouse neurons were transduced with AAVs carrying H2B-GCaMP6s plasmids (H2B-GCaMP6s plasmids were kindly provided by Loren Looger) and transfected with either a mCherry-Cre fusion construct or mCherry only construct – again under the control of the synapsin promoter. After rBDNF application, 40mM potassium chloride was washed in to evoke calcium elevations in all neurons (both those responding and those not responding to rBDNF) to identify neurons that were unresponsive to rBDNF application (Fig2C). These data were analysed by manually inspecting transfected neurons to determine if there was a fluorescence intensity change in response to rBDNF application or 40mM KCl washin. Transfections were carried out on DIV8 or DIV9 and the earliest experiments were carried out five days later on DIV13 or DIV14. Cell health appears to be somewhat compromised by mCherry-Cre expression. There are fewer mCherry-Cre+ cells in each field of view compared to mCherry+ cells (Wilcoxon rank sum test, $p<0.01$). Furthermore, fewer mCherry-Cre+ neurons respond to 40mM KCl washin compared to mCherry+ neurons (Wilcoxon rank sum test, $p<0.001$). Despite the smaller number of detectable mCherry-Cre+ neurons, some respond to rBDNF application (Fig2D). This result suggests that the somatic calcium transient as well as the inward current driving this calcium elevation, are not dependent on TrkB activation.

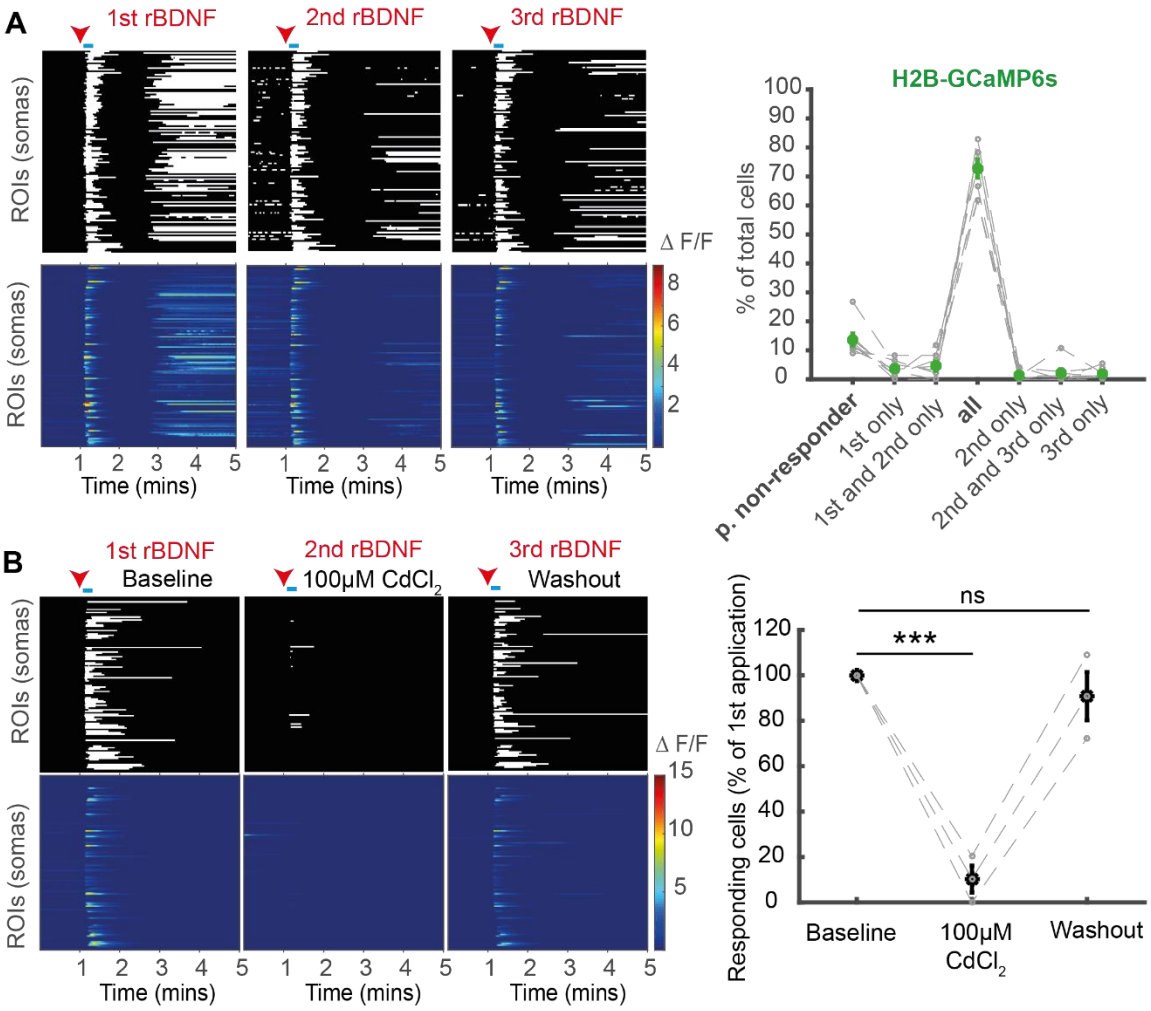
A
1st rBDNF
2nd rBDNF
3rd rBDNF
ROIs (somas)
ROIs (somas)
Δ F/F
8
6
4
2
1 2 3 4 5
Time (mins)
H2B-GCaMP6s
% of total cells
100
90
80
70
60
50
40
30
20
10
0
p. non-responder
1st only
1st and 2nd only
all
2nd only
2nd and 3rd only
3rd only
B
1st rBDNF
Baseline
2nd rBDNF
100μM CdCl2
3rd rBDNF
Washout
ROIs (somas)
ROIs (somas)
Δ F/F
15
10
5
Time (mins)
ns
***
Responding cells (% of 1st application)
120
100
80
60
40
20
0
Baseline
100μM CdCl2
Washout

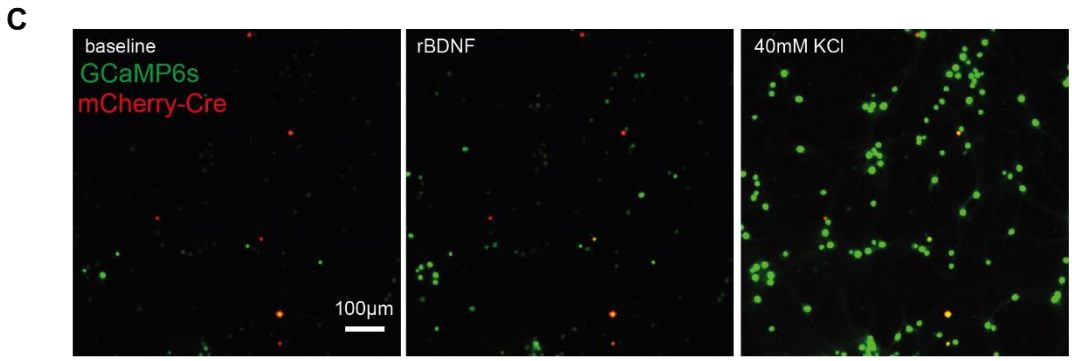
C
baseline
GCaMP6s
mCherry-Cre
100μm
rBDNF
40mM KCl

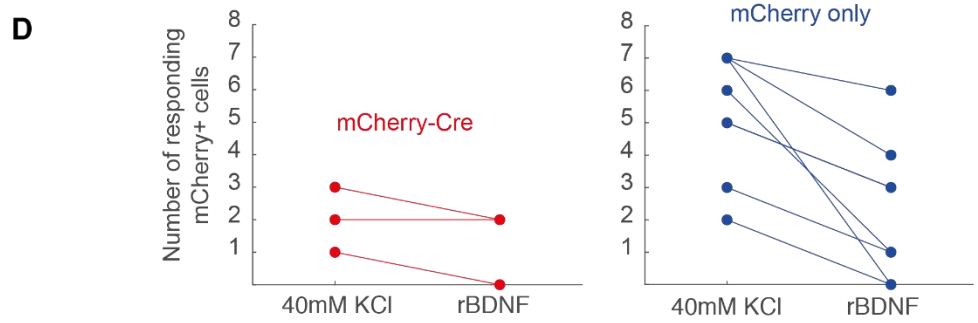
D
Number of responding mCherry+ cells
8
7
6
5
4
3
2
1
mCherry-Cre
40mM KCl
rBDNF
mCherry only
40mM KCl
rBDNF

Figure 2: TrkB-independent somatic calcium transients in response to 100µg/ml rBDNF application. (A) *Imaging somatic calcium responses using histone-tagged GCaMP6s (H2B-GCaMP6s) to 100µg/ml rBDNF application from dissociated hippocampal rat neurons. Regions of interest were placed over cell bodies using a semi-automated approach (see section 2.7). H2B-GCaMP6s expression is limited to cell bodies, which greatly facilitated data analysis. To further characterize the rBDNF response, rBDNF was applied three times with the same field of view. Top three panels show the suprathreshold response to rBDNF application applied for five seconds duration starting one minute (red arrow heads) into image acquisition (frame rate 2.5Hz). Bottom three panels show ∆F/F values for the same experiment as the above panels. Right, categorization of neurons according to which rBDNF application(s) elicit a detectable response between 5-20s after rBDNF application starts (blue bars next to red arrows in A). Neurons showing no response to rBDNF were detected with 40mM potassium chloride. N = 8 coverslips, 3 cultures.* ***(B)*** *Somatic calcium transients in response to rBDNF application are almost completely blocked by 100µM cadmium, which blocks VGCCs (one-way ANOVA, main effect: p<0.001; Tukey-Kramer posthoc test: p<0.001***).* ***(C)*** *Floxed-TrkB dissociated hippocampal neurons expressing H2B-GCaMP6s (green) through AAV transduction (as in A) and transfected with a mCherry-Cre construct (red). Panels showing H2B-GCaMP6s expression are maximum projections across 20 frames during baseline (left), peak of rBDNF response (middle) and following 40mM potassium chloride application (right).* ***(D)*** *Number of mCherry+ cells showing a detectable calcium transient immediately after rBDNF application. N = 8 coverslips, 3 cultures for mCherry only; n = 9 coverslips, 3 cultures for mCherry-Cre. Note that only 3/9 coverslips tested contained KCl-responsive mCherry-Cre+ neurons. Of those responding to 40mM potassium chloride, floxed-TrkB neurons expressing both mCherry alone and mCherry-Cre showed immediate calcium transients suggesting TrkB activation does not fully account for the immediate response.*

(3.1.3) TrkB-KO neurons respond robustly to application of rBDNF

rBDNF solution is prepared by dissolving the lyophilized compound in PBS plus 0.01% bovine serum albumin (BSA). The albumin limits binding of rBDNF to various pieces of labware it may come into contact with. The lypophilized peptide is also not pure. Upon dissolution, the final solution may contain up to 150mM sodium chloride and 50mM sodium citrate. To test for non-specific responses due to pressure application of solution without rBDNF, I pressure applied sodium chloride and sodium citrate dissolved in PBS with 0.01% BSA to 300mM and 100mM, respectively (“NaCl/citrate” solution; pH: 6.98) on to three different coverslips (Fig3A). This was followed by pressure application of 100µg/ml rBDNF solution in each case (Fig3B). High rate of change (in fluorescence intensity) threshold (Tm) is the lowest threshold value required to block detection of the NaCl/citrate solution response (right panels, Fig3A,B), while low Tm (Tm = 0.03) is

the threshold value used for experiments described in figure 2. Even when high Tm is used to analyze data from floxed-TrkB experiments, at least one mCherry-Cre+ neuron still responds to rBDNF. This result indicates that floxed mCherry-Cre+ neurons can show a strong response to application of 100µg/ml rBDNF solution. It therefore seems unlikely that sensitivity of floxed mCherry-Cre+ neurons to rBDNF could be attributed to incomplete TrkB knockout. It is also unlikely that responses from floxed mCherry-Cre+ neurons are sensitive to changes in osmolarity. 100ug/ml rBDNF solution is hyperosmotic, but, in a small number of experiments, pressure application of hyperosmotic sucrose solution alone did not evoke a response (Fig3D).

One possibility is that the TrkB-independent somatic calcium transient could be confined to the soma, while synaptic calcium transients in response to rBDNF application are diminished in TrkB knockout neurons. To measure calcium transients in spines, dissociated hippocampal rat neurons transfected with cytosolic GCaMP6s were imaged at 100x magnification during pressure application using widefield fluorescence microscopy. Spine calcium transients can be readily detected in ACSF without magnesium under these conditions (see section 3.2.1). Regions of interest (ROIs) were automatically generated using an algorithm: Activity-based Automatic ROI Generation (AARG), which uses localized synaptic activity to pin ROIs to sites of postsynaptic activity (see section 3.2.1). Following pressure application of rBDNF, magnesium was washed out of the imaging chamber (while blocking action potentials with 0.5-1µM TTX) to reveal SSCTs, which enables AARG analysis to pin ROIs to synaptic sites across the field of view during analysis (Fig4A). A single floxed-TrkB mouse neuron expressing mCherry-Cre for seven days showed robust calcium transients at most ROIs following rBDNF application, which appears to be stronger than the strongest response detected in seven wild-type rat neurons (Fig4B). All animals used in the preparation of floxed-TrkB mouse cultures, which eventually showed mCherry-Cre+ neurons responding to rBDNF, are homozygous for the floxed TrkB allele. Thus, TrkB should have been knocked out in all Cre+ floxed-TrkB neurons. Together, my findings provide evidence against the notion that the immediate calcium elevation triggered by application of 100µg/ml rBDNF solution depends on TrkB activation.

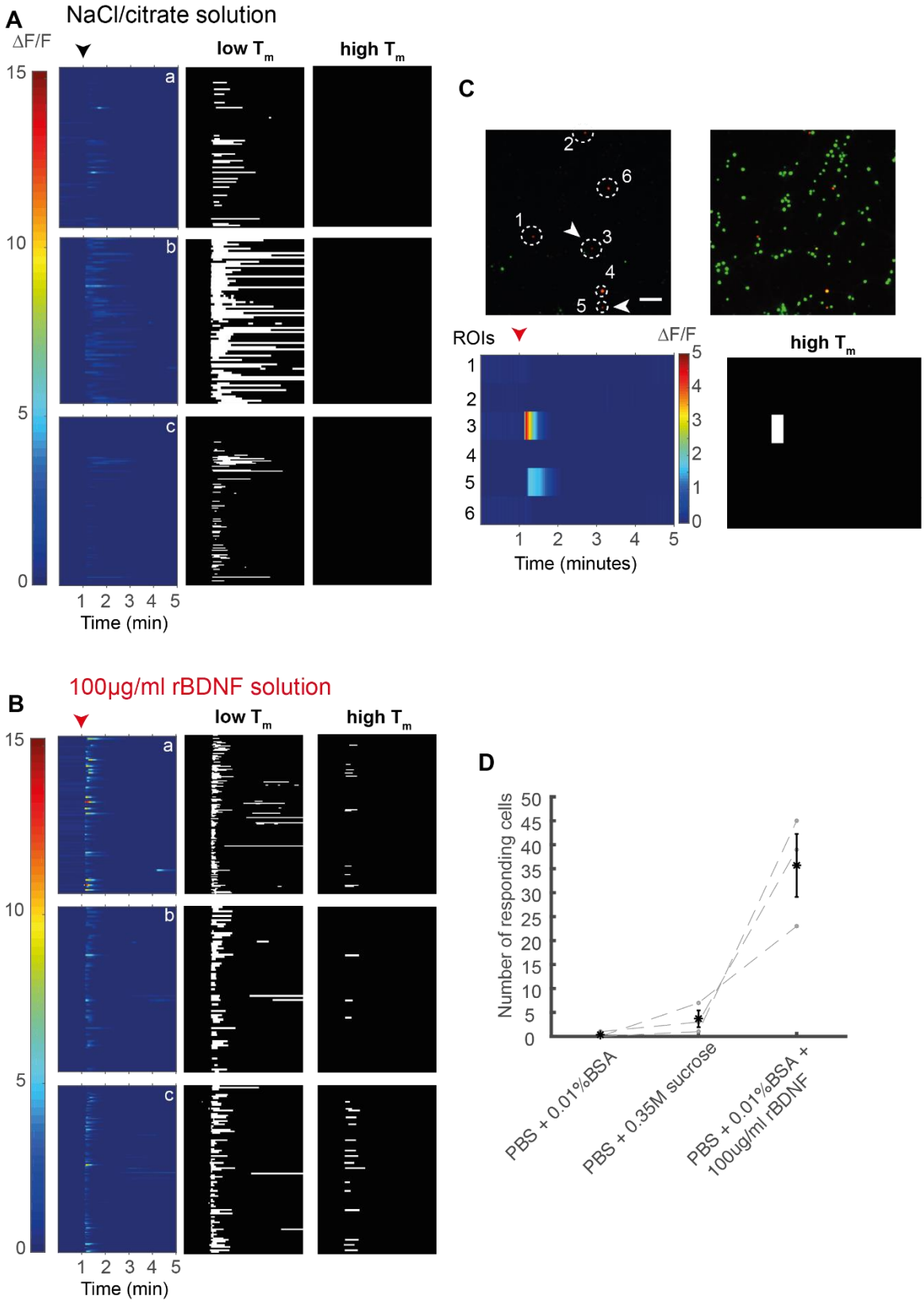
A
NaCl/citrate solution
ΔF/F
low T_m
high T_m
a
b
c
15
10
5
0
1 2 3 4 5
Time (min)
B
100μg/ml rBDNF solution
low T_m
high T_m
a
b
c
15
10
5
0
1 2 3 4 5
Time (min)
C
2
6
1
3
4
5
ROIs
ΔF/F
high T_m
1
2
3
4
5
6
5
4
3
2
1
0
1 2 3 4 5
Time (minutes)
D
Number of responding cells
50
45
40
35
30
25
20
15
10
5
0
PBS + 0.01%BSA
PBS + 0.35M sucrose
PBS + 0.01%BSA +
100ug/ml rBDNF

Figure 3: Other compounds do not fully account for somatic calcium transients evoked by 100µg/ml rBDNF solution. *Lyophilized rBDNF is reconstituted in PBS containing 0.01% crystalline bovine serum albumin (BSA). The lyophilized rBDNF is not pure: NaCl and sodium citrate are present with the rBDNF such that upon reconstitution to 100µg/ml rBDNF, the concentrations of these other compounds could be as high as 150mM NaCl and 50mM sodium citrate.* ***(A)*** *Three experiments (marked a, b and c) with BSA-containing PBS plus 300/100mM NaCl/citrate (instead of 100µg/ml rBDNF) solution in the pressure application pipette (applied for duration of five seconds at 1 minute (black arrow head)). Low Tm is the threshold used during analysis of experiments shown in figure 2. High Tm is the minimum threshold value necessary to eliminate all detected response to NaCl/citrate solution.* ***(B)*** *Same experiments as in A, in which the pressure pipette was exchanged for one containing 100µg/ml rBDNF.* ***(C)*** *Top left, six mCherry-Cre expressing neurons in the field of view (white dashed circles) and their baseline H2B-GCaMP6s fluorescence (maximum projection across first 100 frames). Two neurons (3 and 5) have detectable rBDNF responses (white arrow heads). Top right, overlaid maximum projection image of H2B-GCaMP6s response to 40mM potassium chloride and the mCherry-Cre channel (same experiment as illustrated in figure 2C). Applying high Tm to this experiment does not abolish both responses, suggesting that NaCl/citrate components in rBDNF aliquots may contribute, but do not completely account for the detect signals reported in figure 2C. (scale: 100µm).* ***(D)*** *Hyperosmotic solution (PBS+0.35M sucrose) triggers only a very weak somatic calcium transient (n = 3 coverslips, 1 culture).*

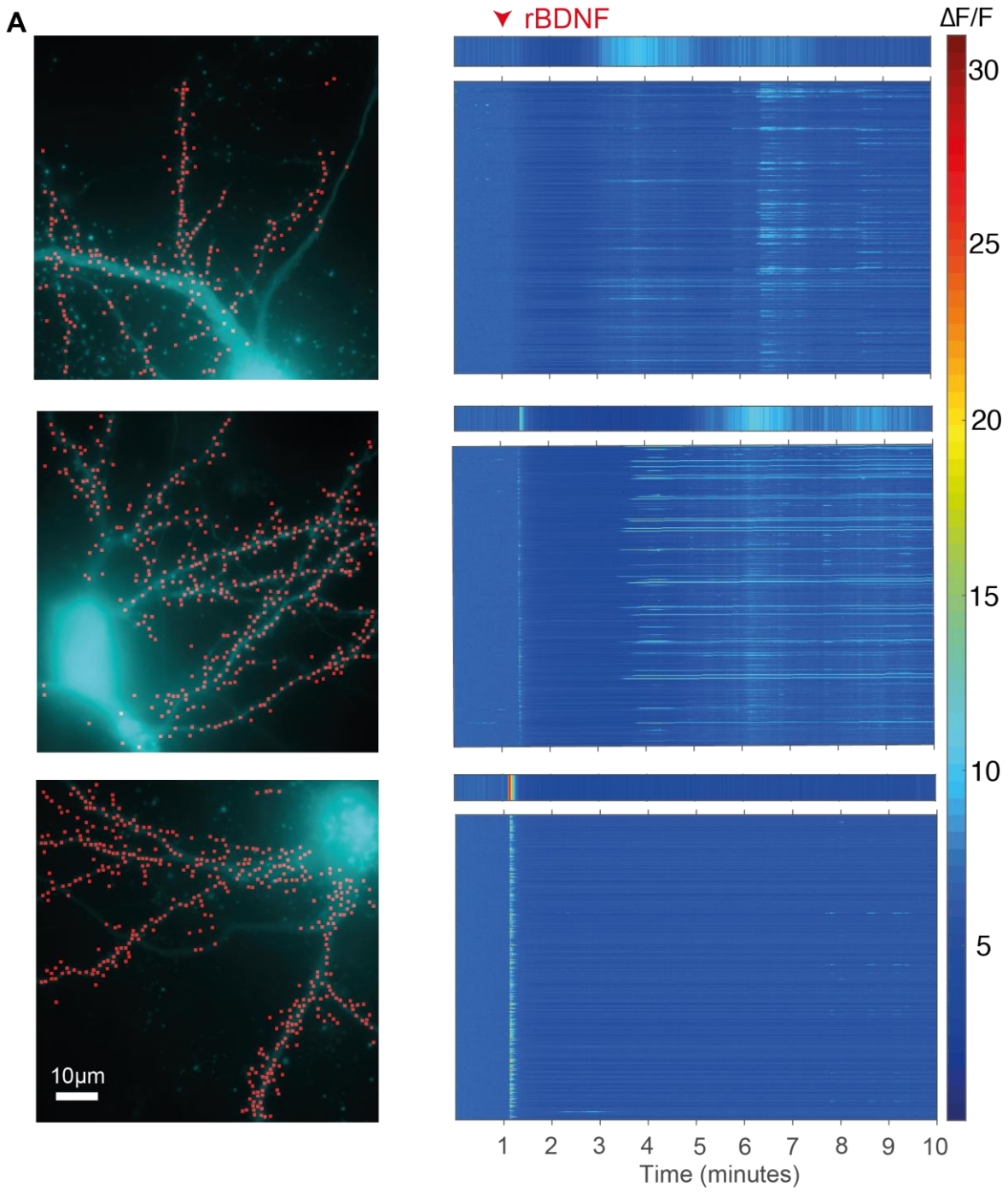

Figure 4: Floxed-TrkB mouse neurons expressing mCherry-Cre for seven days respond to 100µg/ml rBDNF robustly across the dendritic tree. (A) *Variable responses from single rat neurons across multiple 5x5 ROIs established by AARG analysis. One additional ROI is placed in the centre of the cell bodies (not shown in ROI maps). 100µg/ml rBDNF solution was applied (red arrowhead) for five seconds. ROI maps (left) and activity maps (right) from three of seven neurons are shown, which are representative of the between-cell variability in the sample. Panels are ordered with the least responsive cell at the top and the most responsive cell at the bottom. DIV13-18.*

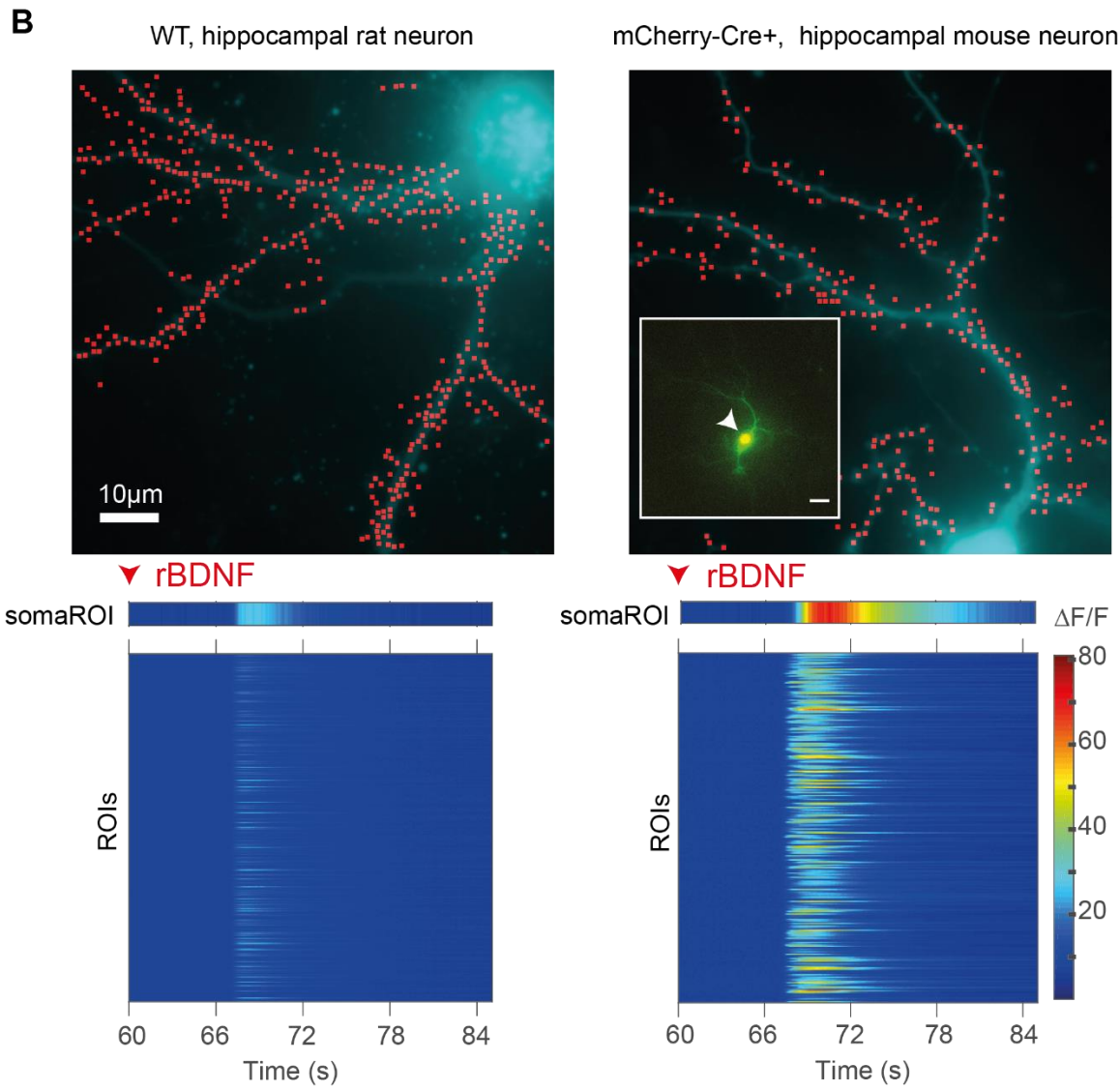

Figure 4 continued. (B) *Left, same dissociated hippocampal rat neuron (top) as shown in A. Right, same as for left, except the cell shown is a dissociated hippocampal mouse neuron expressing mCherry-Cre (inset image: overlay between mCherry-Cre signal and cytosolic GCaMP6s signal shown in yellow (white arrowhead)). Floxed-TrkB neuron: transfection day, DIV8; day of experiment, DIV15.*

(3.2) AARG analysis used to detect distance-dependent voltage-gated calcium channel activation in dendrites

(3.2.1) AARG uses local activity to pin ROIs to postsynaptic sites

Washing out magnesium in the presence of 0.5-1µM TTX reveals SSCTs, which are absent in the presence of 1mM magnesium and TTX (Fig5A) or when exposed to 50µM AP5 in 0 magnesium ACSF (Fig5A). To extract events from raw data, a combined threshold of the fluorescence intensity derivative and event size is applied (see section 2.7). The combined threshold is chosen by taking the lowest values giving no background noise (Fig5B) across all experiments. Suprathreshold SSCTs (tSSCTs) have a centre of mass that can be well approximated by clusters of suprathreshold pixels (Fig5C). Each tSSCT can produce a square ROI centred over its centre of mass and events occurring at the same synaptic input will overlap. The ROI of a given input site is the ideal ROI of the largest event occurring at the respective location. The basic principle of AARG is that each event has an ideal ROI, which can become the established ROI at that site if the event owning it is larger than any preceding event at that site with an overlapping ideal ROI. The one exception to this rule is when ROIs are pre-established. A pre-established ROI is one that is set by an event detected in a preceding condition that is part of the same experiment. For example, in figure 5D yellow ROIs are established by events detected in the second condition after 5µM phorbol ester (+PDA) washin. Red ROIs were established in the baseline condition (or a preceding condition) and are thus treated as pre-established ROIs in the second and third condition. A pre-established ROI cannot be superseded by another ROI. If a larger event is detected in a subsequent experimental condition with an ideal ROI that overlaps the pre-established ROI, the pre-established ROI remains as the established ROI. This exception maintains consistent analysis between treatment groups.

AARG analysis contains an important assumption: one ROI per input site. In figure 5D, the same spine as shown in 5C contains five established ROIs after the third condition (white dashed circle). This represents a high level of oversampling, which can be ameliorated by increasing ROI size. In 512x512 pixel images oversampling can be reduced by selecting 5x5 ROI sizes or larger without compromising overlap with synaptic inputs expressing PSD95-RFP (Fig6B).

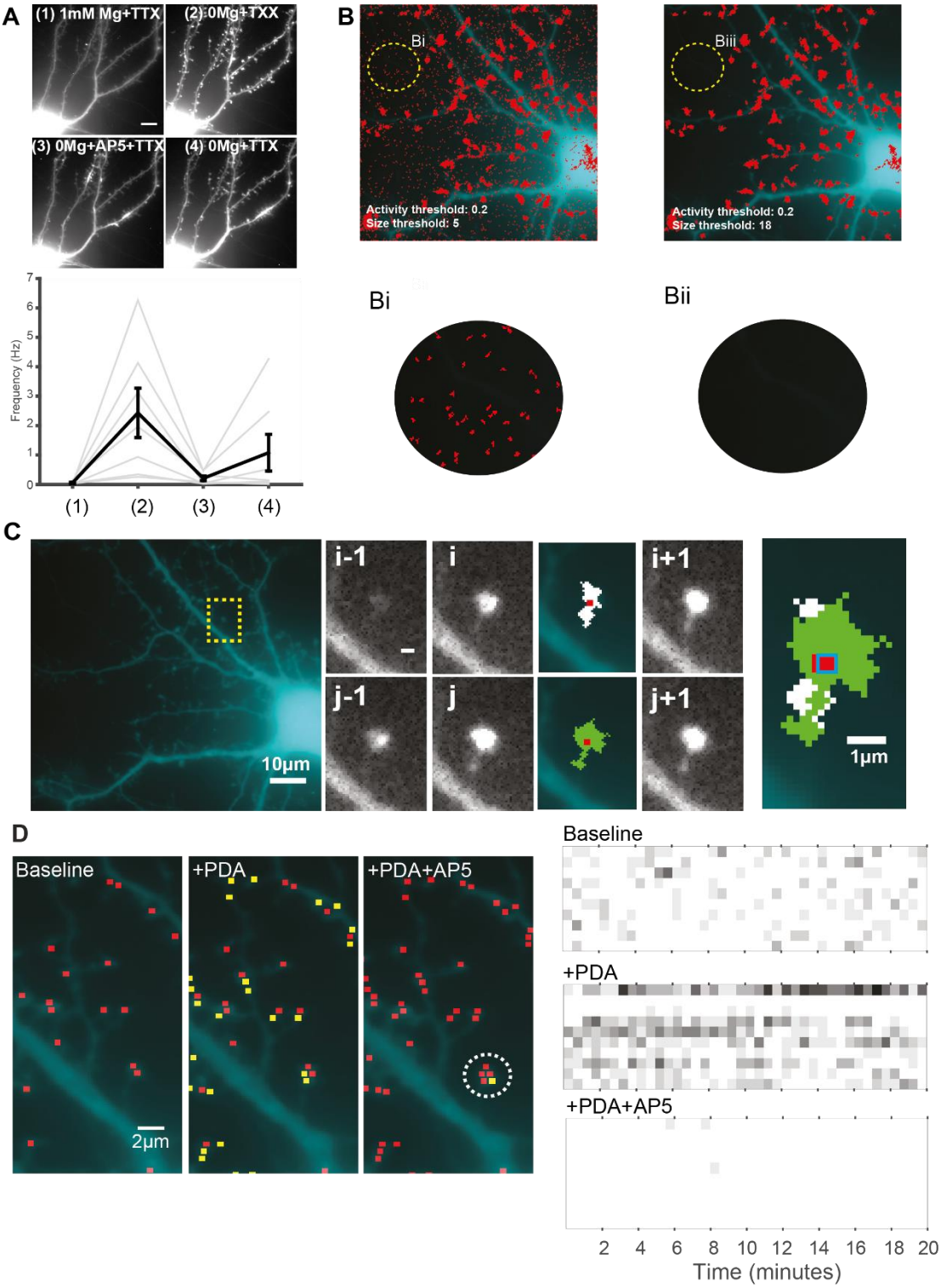
A
(1) 1mM Mg+TTX
(2) 0Mg+TXX
(3) 0Mg+AP5+TTX
(4) 0Mg+TTX
Frequency (Hz)
(1)
(2)
(3)
(4)
B
Bi
Activity threshold: 0.2
Size threshold: 5
Biii
Activity threshold: 0.2
Size threshold: 18
Bi
Bii
C
10µm
i-1
i
i+1
j-1
j
j+1
1µm
D
Baseline
+PDA
+PDA+AP5
2µm
Baseline
+PDA
+PDA+AP5
2 4 6 8 10 12 14 16 18 20
Time (minutes)

Figure 5: Activity-based Automatic Region of interest Generation (AARG) analysis to record spontaneous synaptic calcium transients. (A) *Removing magnesium from extracellular solution increases the frequency of spontaneous synaptic calcium transients to measurable levels. Synaptic calcium transients could be detected using slow acquisition rates (2.5 Hz).* ***(B)*** *Events are extracted using a combination of the events' rate of rise and size. Appropriate thresholds are chosen as the lowest threshold values that exclude almost all noise in background regions (Bi and Bii). High rates of false-positive detection are evident when threshold values are too low (Bi).* ***(C)*** *Each event detected at an active spine is assigned an ideal ROI (red square, 3x3 pixels) overlapping with the event's centre of mass. When ideal ROIs overlap, the ideal ROI belonging to the largest event becomes or remains the established ROI. The event detected in frame i (suprathreshold pixels in white) establishes a ROI from its ideal ROI. The green event occurs later in frame j and has an ideal ROI overlapping with the established ROI (right). The green event is larger than the white event, so the ideal ROI for the green event becomes an established ROI. Data linked to the old established ROI is transferred to the new established ROI. Scale: 1µm.* ***(D)*** *Phorbol ester compounds increase the rate of spontaneous vesicle fusion by priming more synaptic vesicles for release. Left, ROIs established in the baseline or previous condition are shown in red. ROIs established in the current condition (except baseline) are displayed in yellow. Right, activity maps showing top 10 most active ROIs (at baseline). Activity is almost completely abolished by 50µM AP5 as it is in A. Increased activity results in multiple ROIs within a single spine, suggesting use of 3x3 ROIs in 512x512 images can lead to oversampling (white dashed circle).*

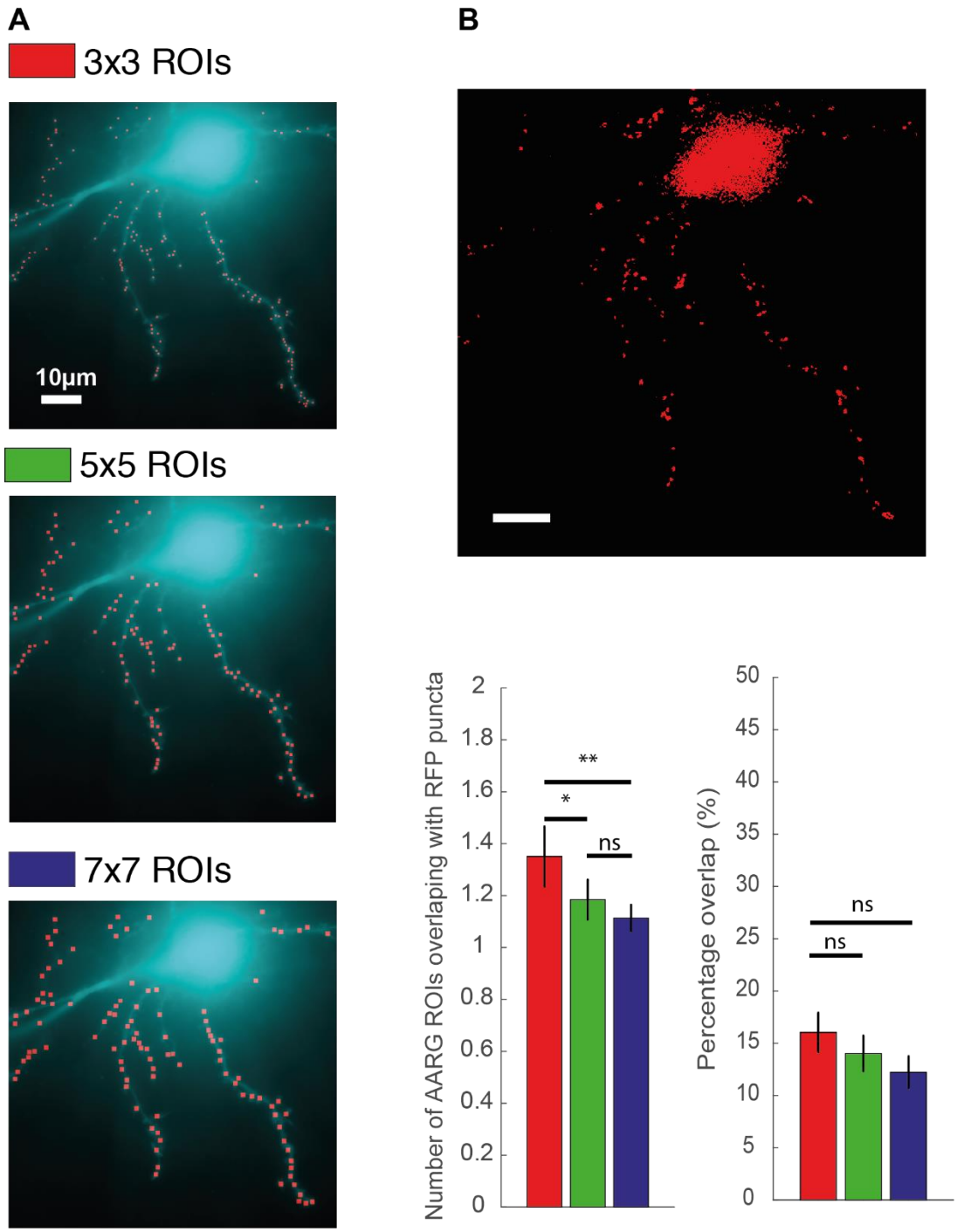

Figure 6: Oversampling can be avoided by using 5x5 ROIs or larger. (A) *AARG analysis repeated for each experiment (with co-expressed cytosolic GCaMP6s and PSD95-RFP) using 3x3 (red), 5x5 (green) and 7x7 (blue) ROIs.* ***(B)*** *Top, PSD95-RFP expression for the cell in A. Bottom, 3x3 ROIs overlap with more discrete RFP puncta compared to 5x5 or 7x7 ROIs (Tukey-Kramer posthoc test, *p<0.05, **p<0.01), suggesting a greater tendency to oversample. Reduced oversampling with large ROIs does not come at a cost of significantly reduced overlap between ROI pixels and RFP+ pixels (one-way ANOVA, F(2,14) = 0.42, p>0.05).*

A

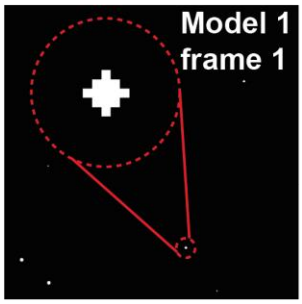

B

Model property	Model 1	Model 2
Total number of events	4000	1500
Number of repeater locations	160	30
Number of repeater events	1600	800
Pre-established ROIs	0	15

C

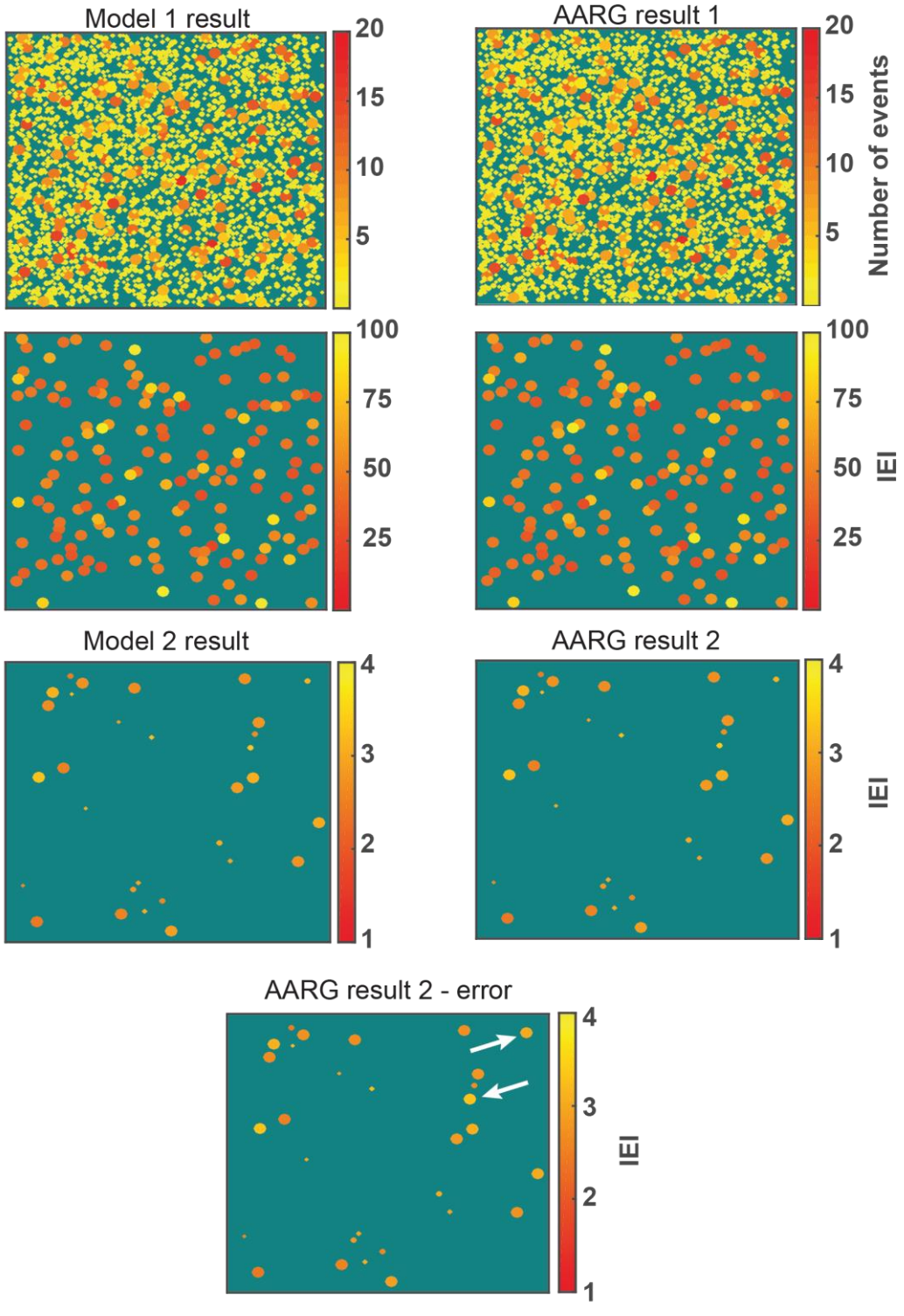

Figure 7: AARG validation. (A) *First frame for Model 1. Every model event (red dashed circle) has the same type of symmetrical structure, but vary in size. The inset event has a size equivalent to 13 pixels.* ***(B)*** *Essential properties of two models used to validate AARG.* ***(C)*** *Model result versus the AARG result. As well as producing the model to validate AARG, the modelling script uses the same output format as AARG. The crucial difference is that the modelling script has access to property information about each event and can assign events to the output on this basis. AARG, on the other hand, must find the appropriate location for the event data algorithmically. Model data presented here is generated from the output structures saved by the modelling script and by AARG after evaluating the model data. Model 2 models the effect of 'pre-established ROIs' (see main text). In this case, AARG must correctly identify pre-established ROIs and not overwrite them, even if the current event is larger. In the example marked 'AARG result 2 - error' pre-established ROIs have been inappropriately overwritten (white arrows) and replaced by the ideal ROIs of the two large events shown. Following updates to the code, the outputs for the modelling script and AARG were in perfect agreement. For clarity, entire events for each established ROI are shown rather than their ideal ROIs.*

(3.2.2) Validating AARG

Given the complexity of the algorithm, it is necessary to validate AARG using model data. To this end, I wrote a modelling script, which can generate any number of symmetrical model events (Fig7A). The modelling script consists of multiple user-determined parameters to set the complexity of the model in terms of the overall number of events and proportion of different types of events. A model event is a two-dimensional object representing a cluster of suprathreshold pixels that would be attained after applying the derivative and size thresholds to real data.

Every model can contain three types of events: Large events, repeater events and free events. A repeater location is defined by the ideal ROI of the large event that 'owns' this location. Only one large event occurs at any given repeater location, but any number of repeater events can occur at a repeater location. The ideal ROI of a repeater event must overlap with the ideal ROI of the large event. Free events have ideal ROIs overlapping with no other ideal ROIs from other events. Large events have a uniform size, which is always distinctly greater than the different sizes of repeater or free events.

In addition to creating the model data, the modelling script produces the same cell array output structures as AARG. If AARG and the modelling script work as intended, the cell arrays and their contents should match perfectly. The modelling script has access to information about each event's identity (whether it is a large event, repeater event or free event) and updates the cell

arrays based on this information. AARG, however, must determine algorithmically how the cell array should be updated with each frame.

In figure 7, AARG has been validated using two models. The contents of the cell arrays are displayed in the form of heatmaps showing the number of events and the inter-event interval (IEI) for each established ROI (Fig7C). For clarity, each established ROI is represented by the event that created it rather than a small 3x3 element structure. Note that free events will only ever have a sum of one event, so they do not appear in the IEI display. Model One models events in a single condition, and Model Two models events producing pre-established ROIs. In the latter case, AARG should plot the event sizes linked to the pre-established ROIs and not overwrite them with ideal ROIs from the large events. As illustrated in the bottom panel, an error has occurred: two smaller events modelling events making pre-established ROIs were replaced by large events with overlapping ideal ROIs (indicated by the white arrows). Activity maps such as those displayed in figure 7 are used principally for display. To verify a perfect match between the AARG and modelling script cell arrays, a simple Matlab function was written to check each cell for matching contents. Following iterative refinement of AARG and the modelling script, the algorithms eventually showed 100% agreement for Models One and Two.

(3.2.4) Measuring SSCT amplitudes

Combined rate of fluorescence intensity change (activity) and size thresholding does not adequately detect events from timelapse images acquired at faster frame rates (20Hz rather than 2.5Hz). The detection of suprathreshold SSCTs is improved by first defining the neighborhood correlation values for each pixel and excluding values below 3x standard deviation value. Since synaptic events will produce pixels with stronger neighborhood correlation values, much of the background can be excluded based on this thresholding mask of the neighborhood correlation values. A second step involves calculating cross-correlation coefficients for the pixels containing suprathreshold neighborhood correlations and limiting suprathreshold pixels to those exceeding further thresholds. The cross-correlation coefficient (COR) is calculated by first obtaining the cross-covariance coefficient (COV) between the data and a template. The template models a range of one-dimensional SSCTs (methods figure 1E). Dividing by the standard deviation of fluorescence intensity across time for each pixel yields COR (equation 3.2, section 2.8.4). COV and COR have complementary properties: COV is effective in detecting small events that match well to one of the templates, but is ineffective in excluding large events that do not match well to any template. COR, on the other hand, tends to inappropriately pass small noise with good template matches, but is effective in removing large events with poor template matches. A final cross of COR with COV

yields the final pixel coefficients (E) (equation 3.3; methods figure 1F). E coefficients reduce the number of thresholds that must be applied by combining the advantages of COR and COV.

Suprathreshold SSCTs (tSSCTs) detected using the correlation threshold (Fig8C) are 3D structures in contrast to tSSCTs created from the fluorescence intensity derivative and size combination threshold. The AARG algorithm is well suited to establishing ROIs from such structures. A 3D tSSCT will be detected over multiple frames and AARG will treat each component of an event as an individual event. Data collected by a single ROI can be plotted as event size (in pixels) versus time (Fig8E). When appropriately scaled, individual events can be identified as contiguous changes in event size with a clear event size peak and time gaps separating individual events (Fig8E, inset). Local maxima of fluorescence intensity (red points, Fig8E) overlapping with largest event size measurements reliably detect amplitude peaks (Fig8F,H). In the example shown in figure 8, the top two most active ROIs showed a positively skewed distribution of event peak amplitudes (Fig8G,I) – although the third most active ROI shows a distribution that could arguably be described as approximating a Gaussian distribution (Fig8I). Overall, there is a clear positive skew of SSCT peak amplitudes (Fig8J). When distributions are positively skewed the median average becomes a more representative value than the mean. In non-skewed, Gaussian distributions mean and median values are equal. To avoid potential sampling errors, I used the median rather than the mean SSCT peak amplitude for each ROI.

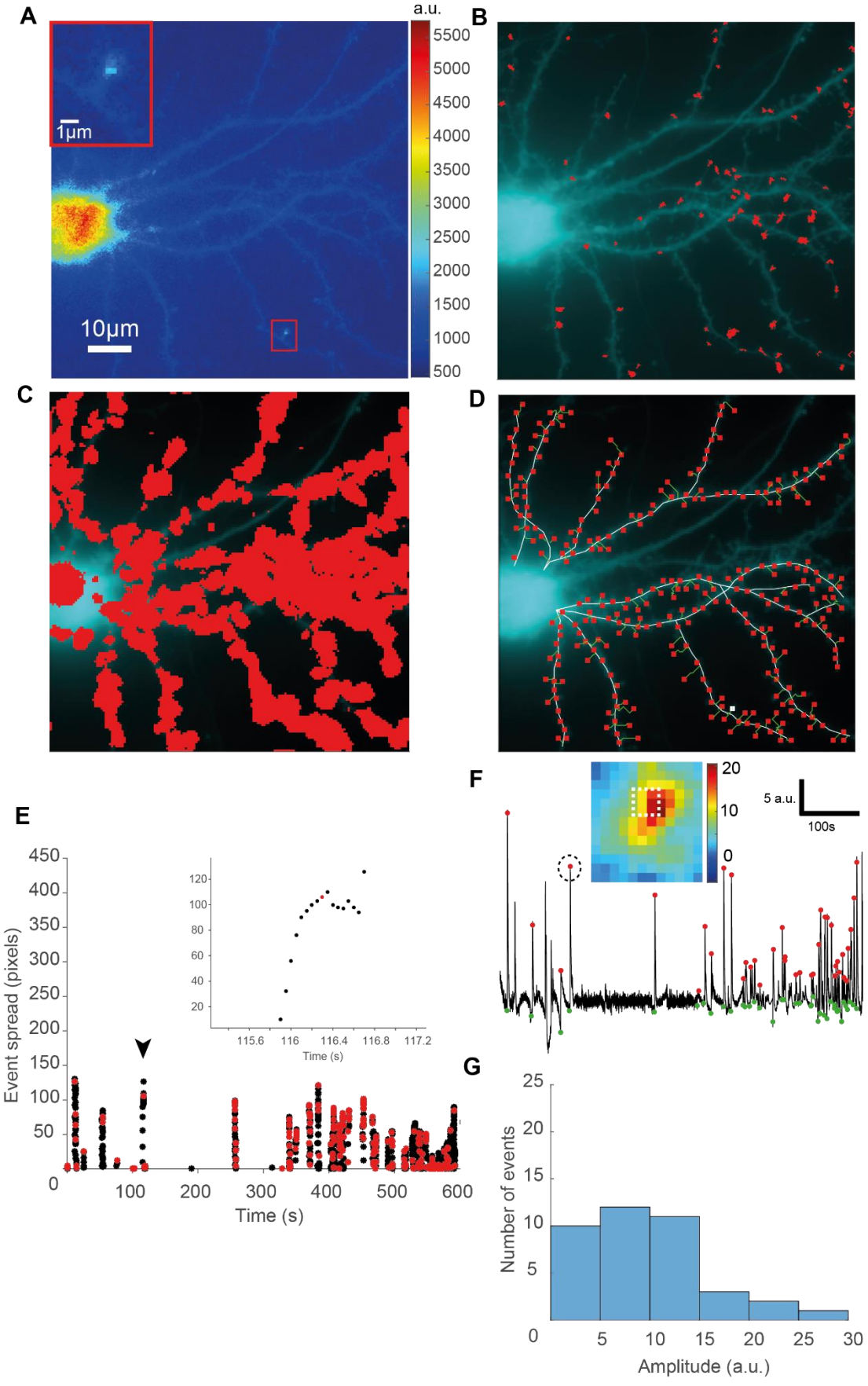
A
a.u.
5500
5000
4500
4000
3500
3000
2500
2000
1500
1000
500
1µm
10µm
B
C
D
E
Event spread (pixels)
450
400
350
300
250
200
150
100
50
0
100
200
300
400
500
600
Time (s)
120
100
80
60
40
20
115.6
116
116.4
116.8
117.2
Time (s)
F
20
10
0
5 a.u.
100s
G
Number of events
25
20
15
10
5
0
5
10
15
20
25
30
Amplitude (a.u.)

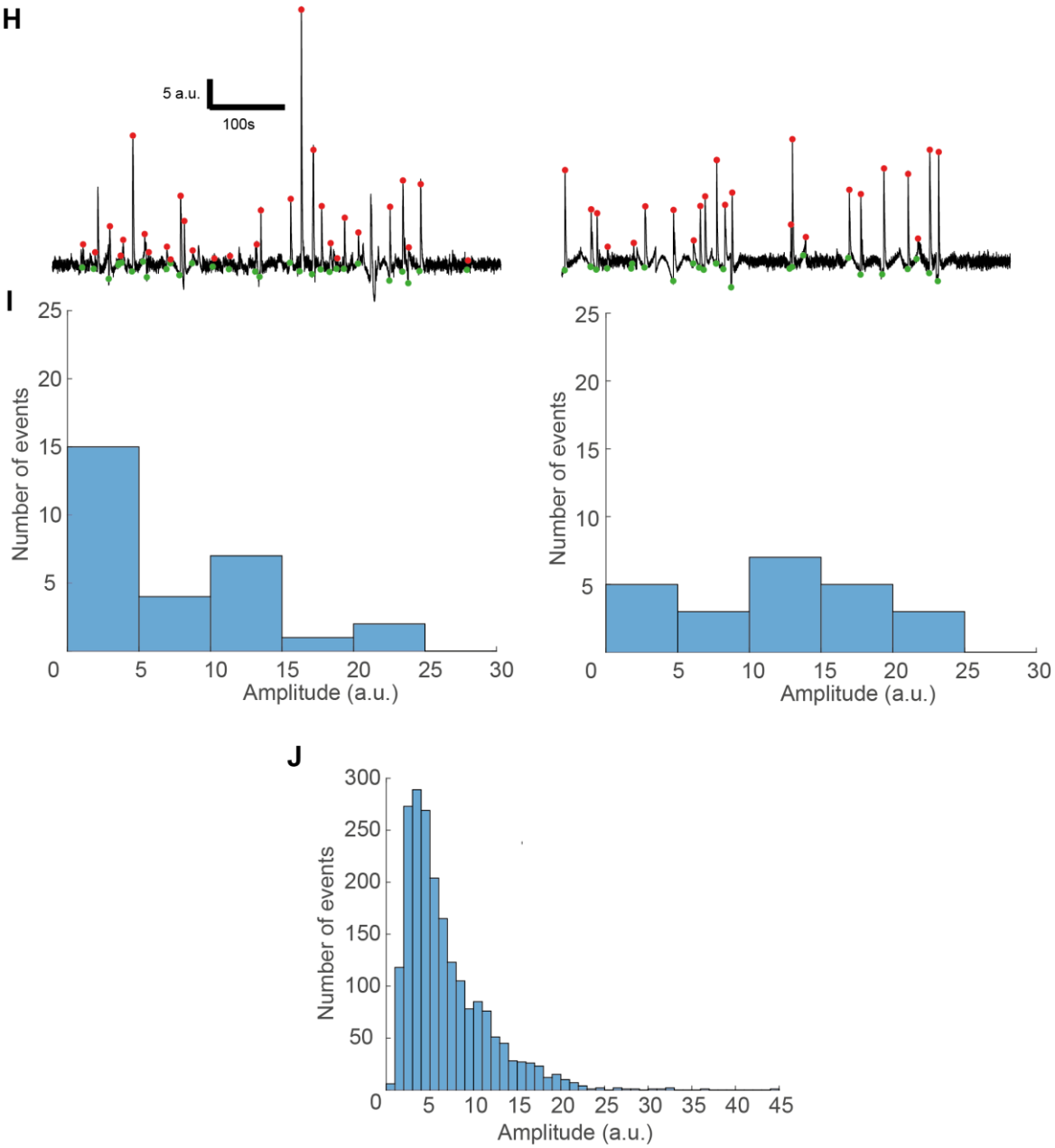

Figure 8: Accurate detection of synaptic calcium transient peaks by thresholding cross-correlation coefficients. ***(A)*** *Raw data image of a single frame with an active spine (red box). Inset, enlarged image of active spine.* ***(B)*** *Combined fluorescence intensity derivative plus size threshold applied to 4000 frames acquired at 20Hz.* ***(C)*** *Events detected across the same frames as in B by thresholding E coefficients (see sections 2.8.3 and 2.8.4) for each pixel.* ***(D)*** *Established ROIs included in data analysis. White lines are drawn manually and are connected to a start point on the cell body or another white line. Green lines connect each ROI to the adjacent white line (see section 2.8.6). Lateral shift during the time course of each experiment was measured before analysis and corrected if necessary.* ***(E)*** *With fast acquisition thresholding, AARG collects each component of every event (black dots) and identifies local maxima within each event (red dots). Event components from a single ROI collected during 10 minutes image acquisition. Inset, single*

event (black arrowhead in main graph) with one local maxima. Event peaks are provisionally identified as the local maxima with the largest component (i.e. largest point of event spread). ***(F)*** *Trace for white ROI in D lasting 10 minutes in total. This is the most active ROI. Peaks (red dots) are automatically detected. Some parts of the trace fall below stable sections of baseline because data are analysed in 500 frame chunks. Inset shows, the same SSCT after image processing as shown in A with the 3x3 established ROI (for a 170x170 pixel image) outlined (white dashed box). This is the peak of the event highlighted in E and F (dashed circle).* ***(G)*** *Frequency histogram for peak amplitudes for events shown in F. Median rather than mean peak amplitudes are used as representative values due to the strong positive skew. Distribution includes all events detected in each ROI over a 10-minute imaging period.* ***(H)*** *Trace for 2nd (left) and 3rd (right) most active ROIs with the corresponding amplitude distributions shown in* ***(I)****.* ***(J)*** *Amplitude distribution for all events across all ROIs.*

(3.2.5) Absence of SSCT scaling within branches

Due to filtering of synaptic signals between input sites and points of signal integration (Spruston *et al.*, 1994; Magee, 2000) as well as compensatory mechanisms known to exist at some synapses to counter these effects (Magee & Cook, 2000; Katz *et al.*, 2009; Shipman *et al.*, 2013), it is possible that correlations between median peak amplitude of SSCTs and distance from branch point within single branches are common.

Losonczy & Magee (2006) found no correlation between spine calcium transients and location from branch point along apical oblique dendrites of CA1 pyramidal neurons. In line with this previous finding, I detected very few (~2% out of 474) dendrites with either a positive or negative correlation between median peak amplitude and distance along the dendrite (Fig9). The small percentage of dendrites showing a correlation between distance and amplitude are evenly distributed across dendrites of different diameters. Thus, correlating dendrites did not cluster among extremely thin or thick dendrites.

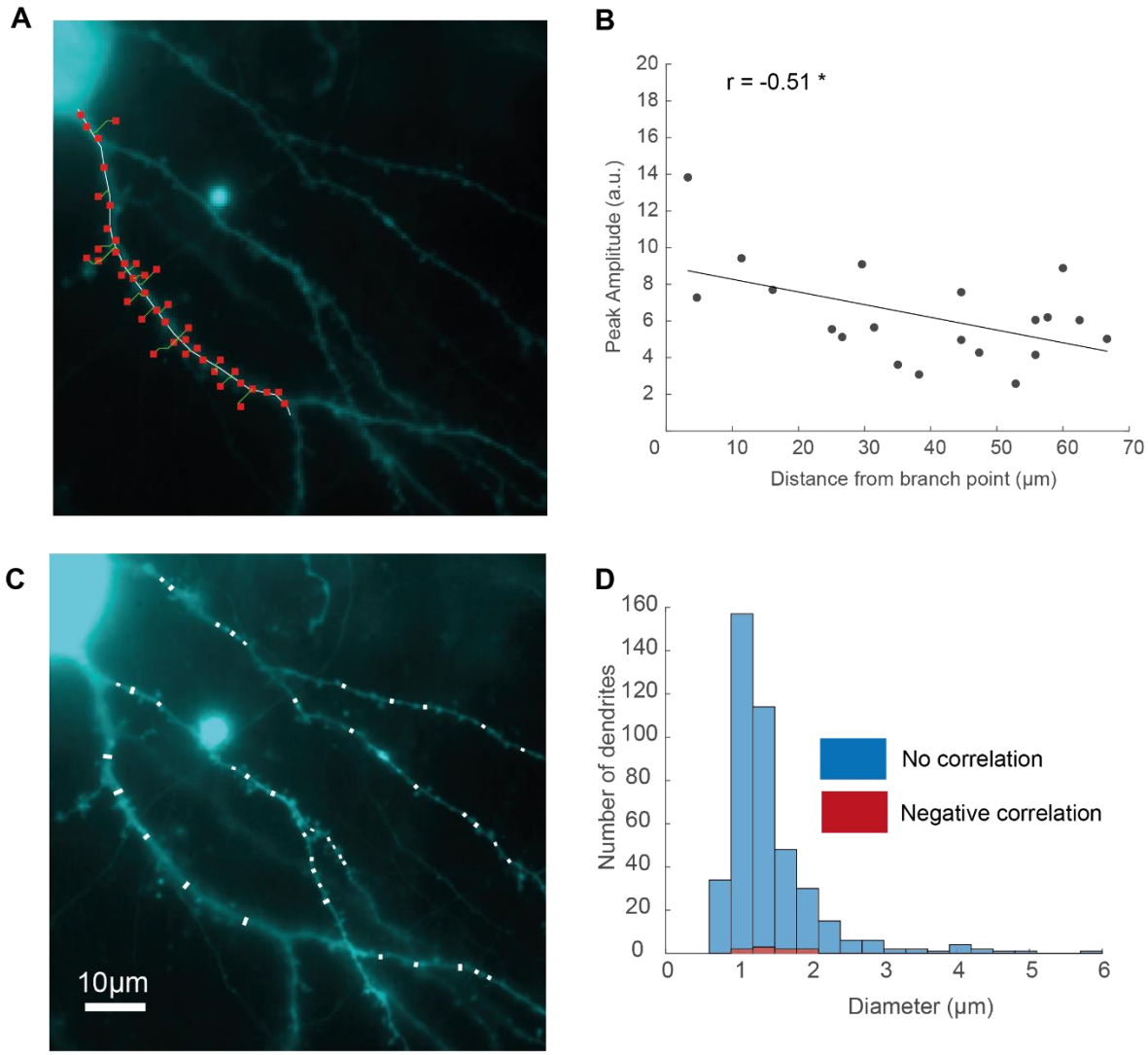

Figure 9: Correlation between peak amplitude and distance from branch point exists only in a small proportion of dendrites. (A) *One of a small percentage (1.9%) of 474 branches showing a significant negative correlation (shown in B) between median peak amplitude and distance from branch point.* ***(C)*** *White bands mark locations where dendrite diameters are measured. Diameter of a single branch is typically measured at three or more locations.* ***(D)*** *Most branches show no correlation between median peak amplitude and distance from branch point (blue) while a very small proportion of branches show negative skew (red). A similar proportion show positive skew (not shown). Correlating branches show no obvious signs of clustering within branches of specific diameters, suggesting they do not occur exclusively within thinner distal branches or thicker main apical branches of pyramidal-like dissociated neurons. 474 dendrites across 40 cells. Branches were excluded from analysis if less than 25µm in length.*

(3.2.6) Calcium channel contribution to SSCTs depends on dendrite distance from soma

Dendritic cable filtering is thought to necessitate distinct learning rules depending on distance of synaptic input from the axon initial segment (Froemke *et al.*, 2005; Sjöström & Häusser, 2006; Letzkus *et al.*, 2006) – the major point of synaptic integration in every neuron. It is therefore reasonable to predict that distance-dependent patterns of plasticity-related protein expression exist to support these different learning rules. Voltage-gated calcium channels are involved in the induction and/or maintenance of LTP (section 1.2.6) and could contribute differently to the amplitude of SSCTs depending on distance of the synaptic input site from the soma. I found that non-specific blockers 100µM cadmium and 10µM mibefradil (more potent against CaV3, but also blocks ATP-dependent K+ channels –Gomora *et al.*, 1999) significantly reduce SSCT amplitudes at all dendrite classifications (Fig10A,B). This is also true for nimodipine, a commonly used dihydropyridine – a class of drug that blocks CaV1 channels (Fig10A,B). Blockade by selective inhibitors for CaV2.3, CaV2.2 and CaV3 channels shows a distinctive distance-dependent gradient with more proximal primary dendrites exhibiting a significant decrease in median peak amplitudes of SSCTs than more distal dendrites beyond secondary classification (Fig10C,D). Thicker dendrites are more likely to be primary dendrites than secondary or beyond secondary. Dendrites with larger diameters exert different biophysical constraints on synaptic signals, which may account for the observed gradient with specific blockers. Discounting primary and secondary dendrites with larger diameters than the widest >secondary dendrite removes significant effects of specific CaV2 blockers, but not CaV3 (Fig11). It seems that CaV3 participation in transmitter-evoked SSCTs is distance-dependent, with less participation occurring at more distal synapses. These data further suggest that CaV1 channels are the only major channel subtype contributing to SSCT at distal synaptic inputs in dissociated hippocampal cultures under these experimental conditions.

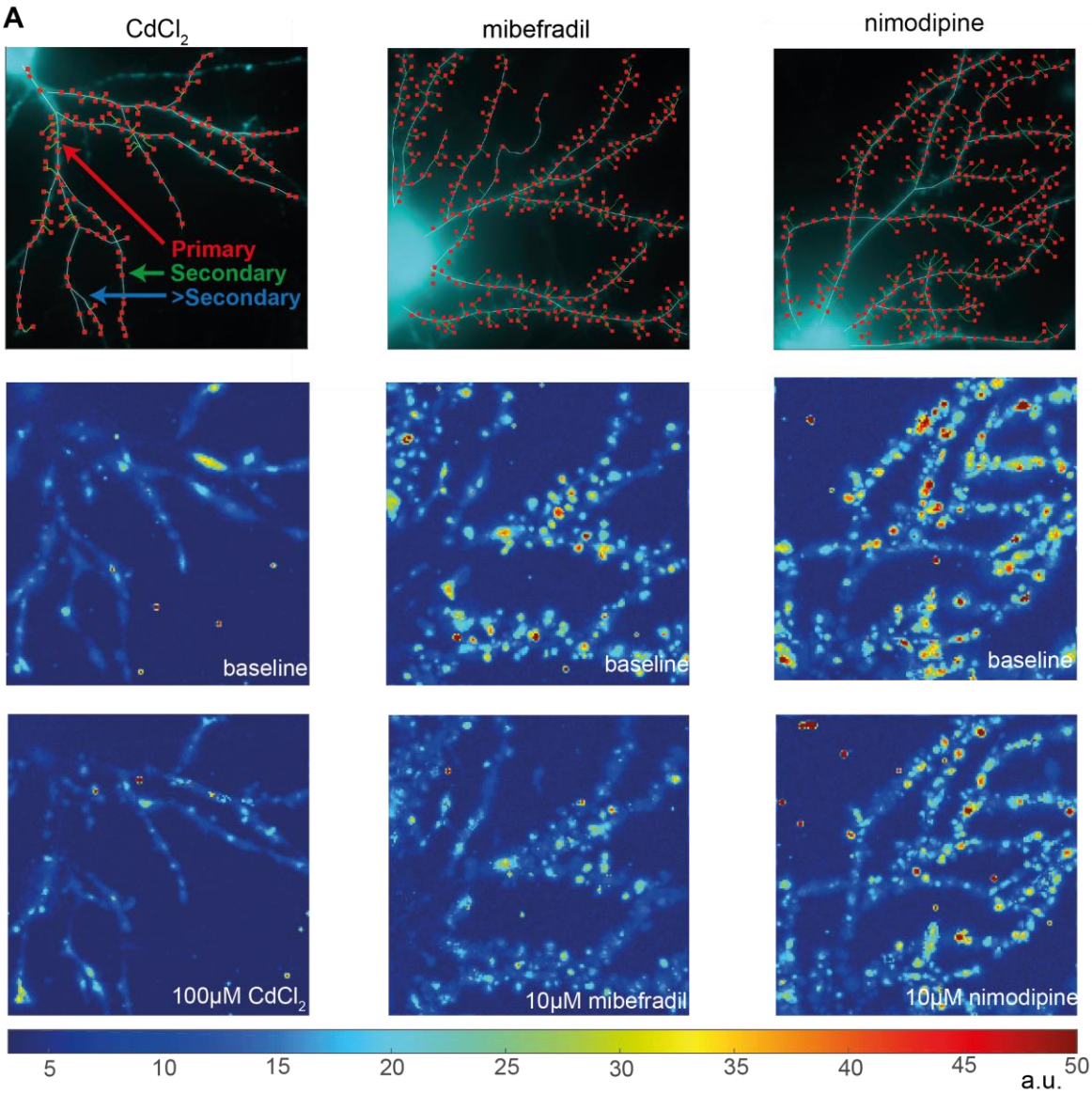

Figure 10: Gradient of sensitivity to specific VGCC blockers across the dendritic tree. (A) *Top panels, ROIs established by AARG after analyzing events from baseline and treatment condition. Middle panels, maximum projection images across 10 minutes after normalization and background subtraction before washing in blockers. Lower panel, same as middle panels after washing in blockers: 100µM cadmium, 10µM mibefradil (CaV3 antagonist – but see section 3.2.6), 10µM nimodipine (CaV1 antagonist). Dendrites are classified according to number of branch points between the current branch and the cell body. Primary dendrites are connected directly to the cell body, while for secondary dendrites there is one branch point.*

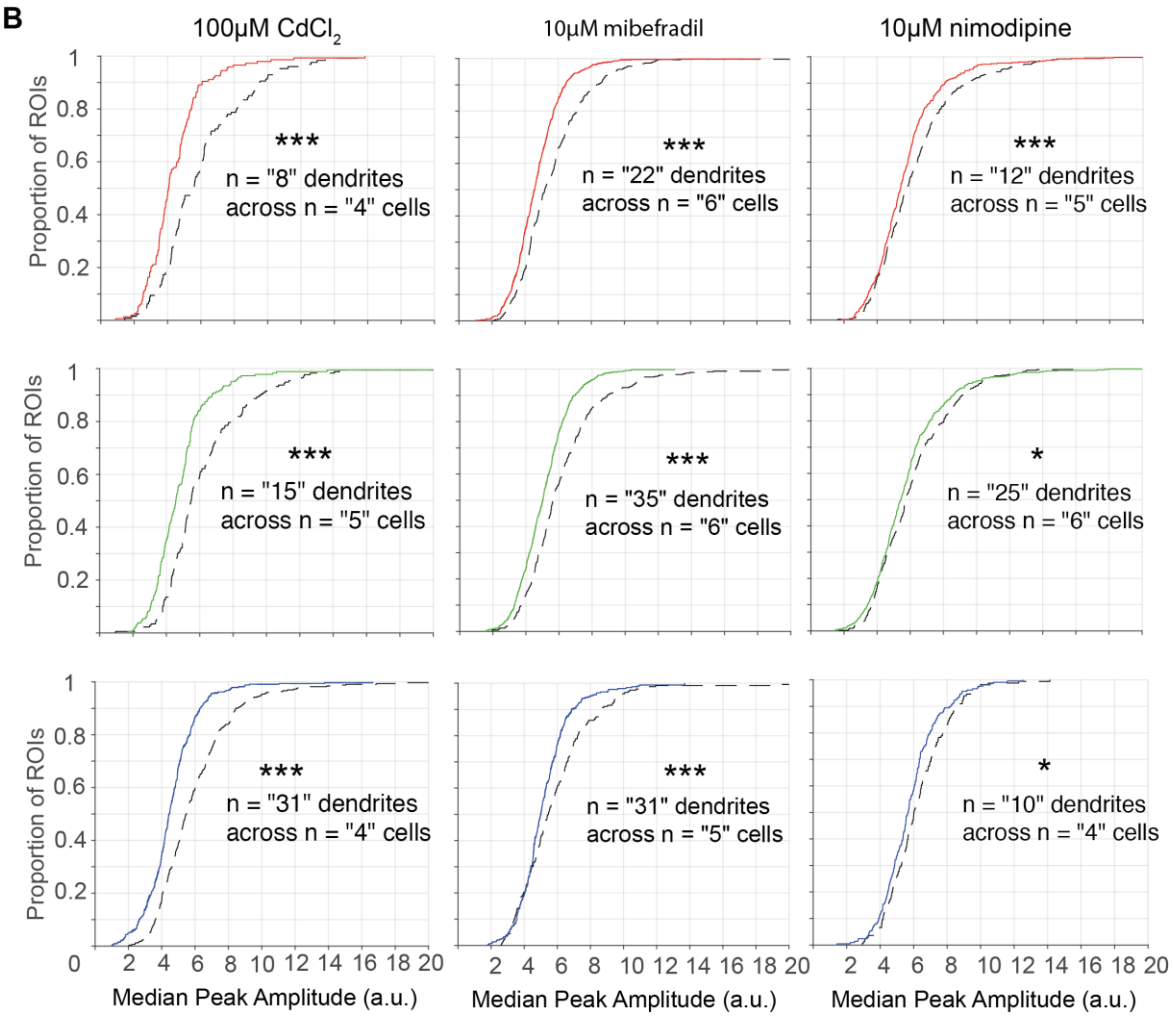

Figure 10 continued. (B) *Cumulative distribution plots with Kolgomorov-Smirnov (KS) statistics applied to primary (red), secondary (green) and >secondary (blue) dendrites for three different blockers: 100µM $CdCl_2$, 10µM mibefradil and 10µM nimodipine. *p<0.05;***p<0.001. Black dashed line indicates baseline measurements.*

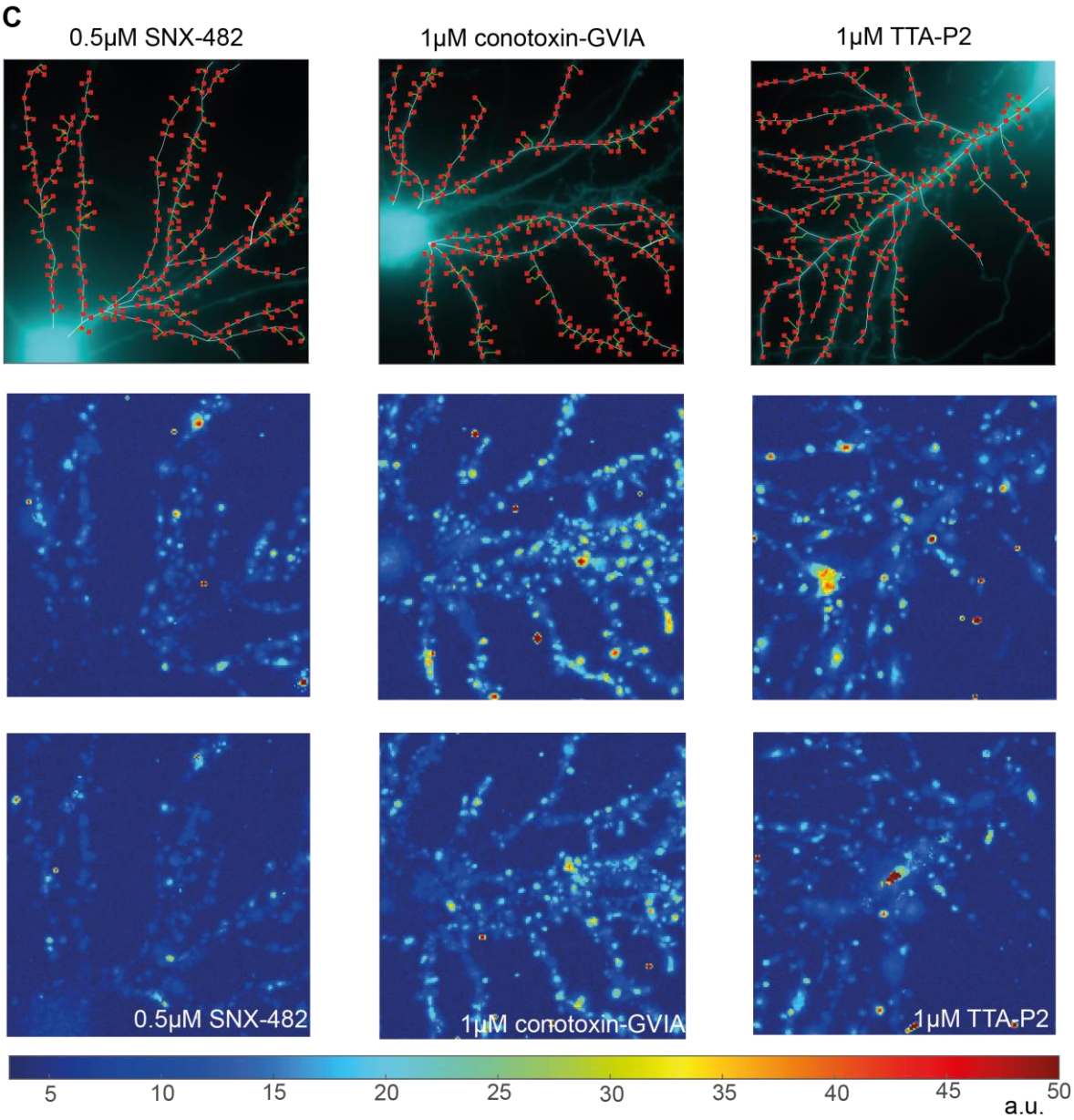

Figure 10 continued. (C) *Same as A, but for 0.5µM SNX-482 (peptide blocker specific for CaV2.3), 1µM conotoxin-GVIA (peptide blocker specific for CaV2.2) and 1µM TTA-P2 (specific for CaV3 channels).*

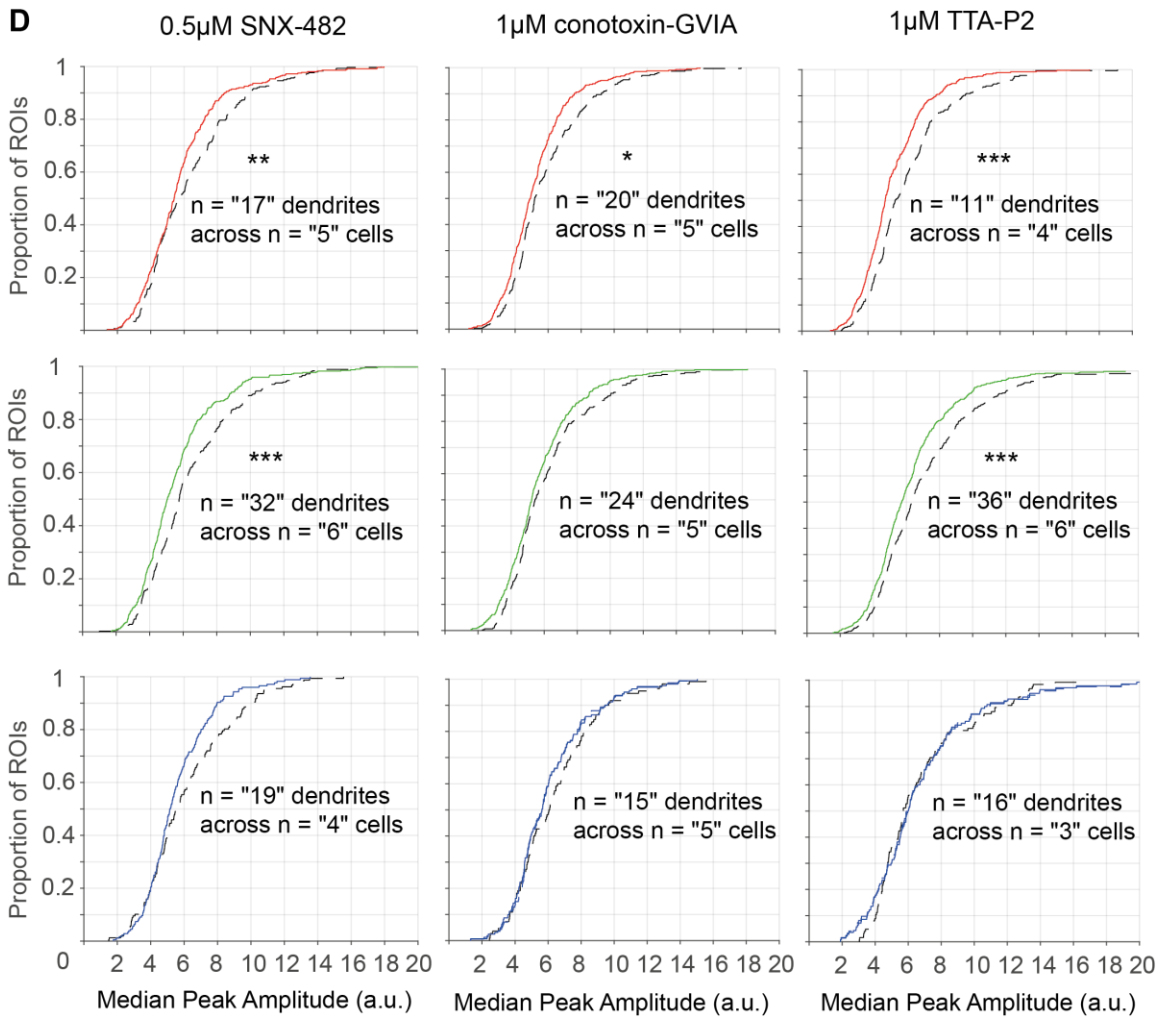

Figure 10 continued. (D) *Specific blockers for CaV2.3 subtypes (0.5μM SNX-482), CaV2.2 (1μM omega-conotoxin-GVIA) and CaV3 (1μM TTA-P2) reveal a gradient of sensitivity across the dendritic tree. Cumulative distribution plots with Kolgomorov-Smirnov (KS) statistics applied to primary (red), secondary (green) and >secondary (blue) dendrites. *p<0.05; **p<0.01; ***p<0.001.*

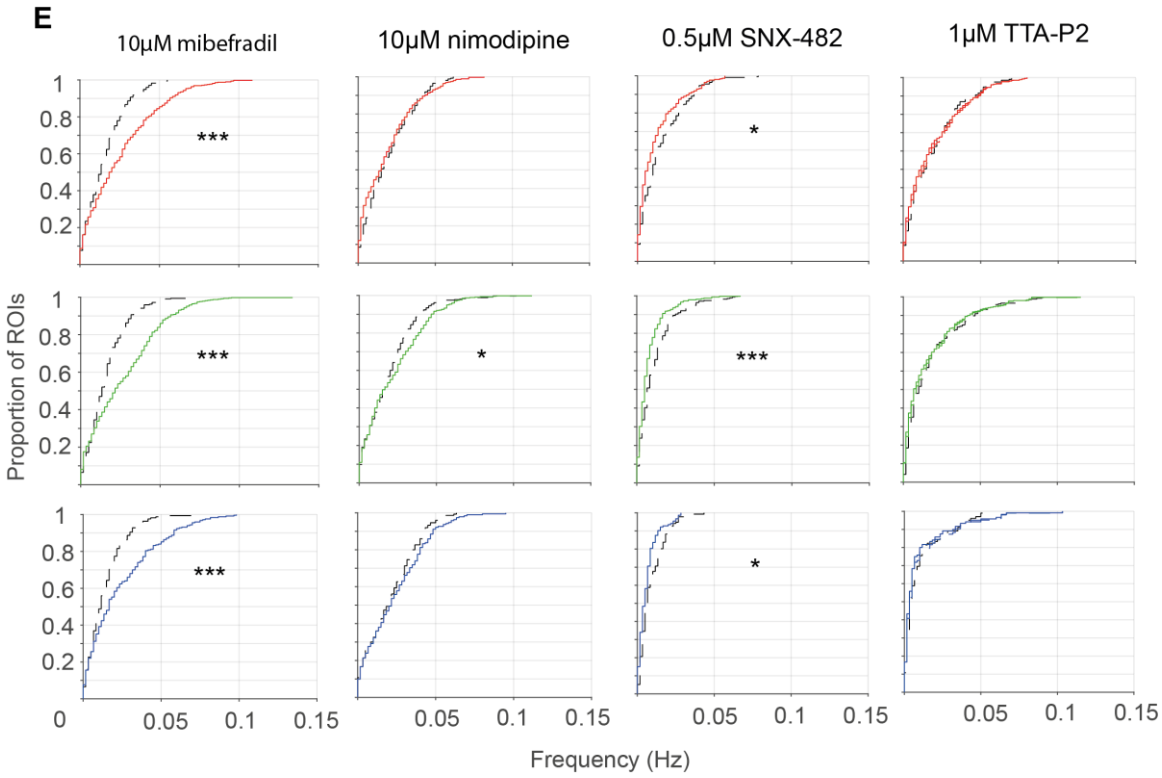

Figure 10 continued. (E) *Frequency of SSCTs increases significantly across all dendrite classifications following 10μM mibefradil treatment, while 0.5μM SNX-482 treatment was followed by a significant decrease in SSCT frequency. These data are derived from the same experiments as the amplitude data presented in B and D. Cumulative distribution plots with Kolgomorov-Smirnov (KS) statistics applied to primary (red), secondary (green) and >secondary (blue) dendrites. *p<0.05; **p<0.01; ***p<0.001.*

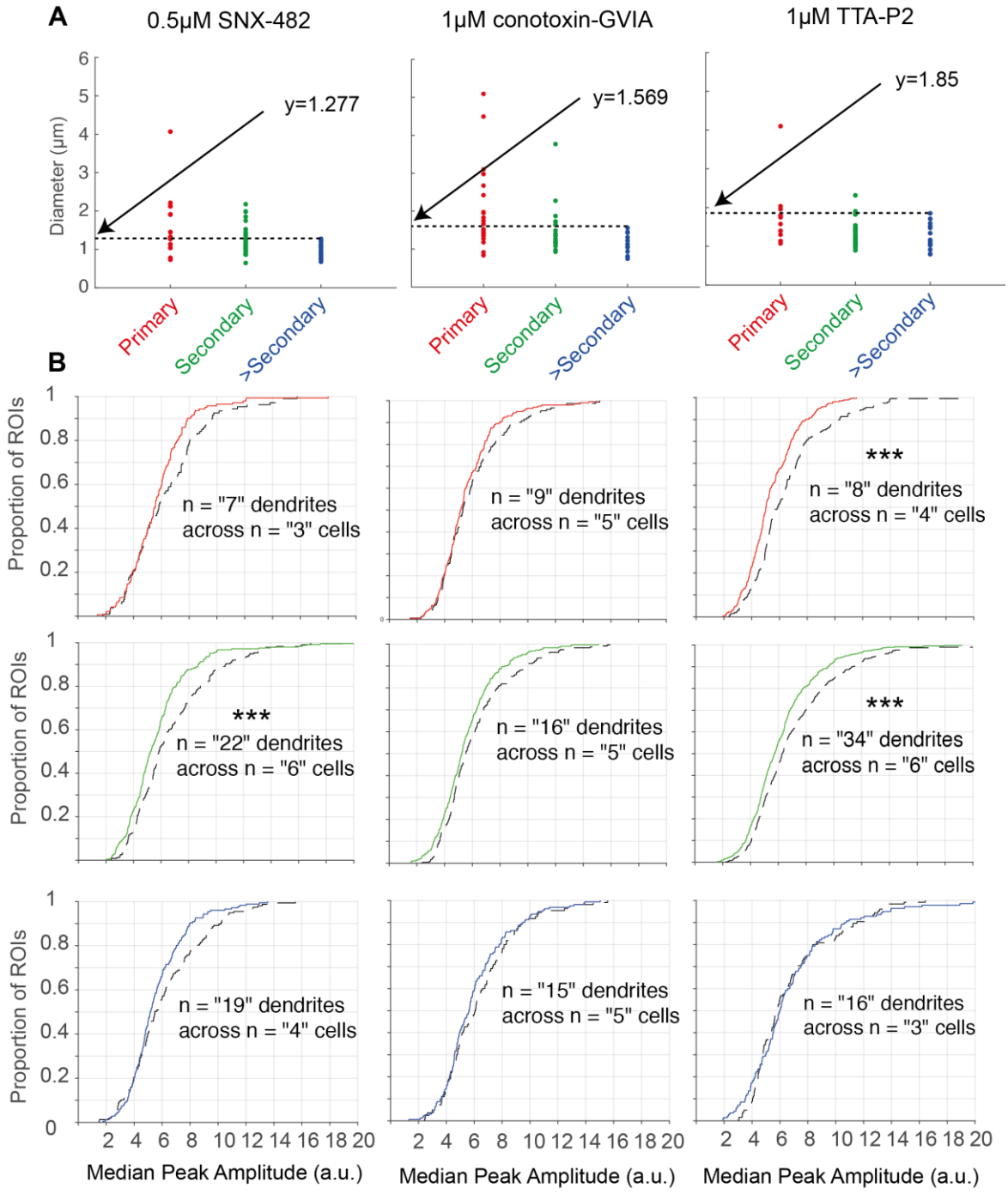

Figure 11: Sensitivity gradient does not depend on dendrite diameter. (A) *Dendrite diameters for each classification. Only dendrites equal to or thinner than the diameter of the thickest >secondary branch are included in this analysis (black dashed line).* ***(B)*** *Cumulative distribution plots as shown in figure 10. Same data as in figure 10, but with dendrites thicker than the values indicated by the dashed line intersecting the y-axes in A excluded. Cumulative distribution plots with Kolgomorov-Smirnov (KS) statistics applied to primary (red), secondary (green) and >secondary (blue) dendrites. ***p<0.001.*

Appendix

(A.1) Paired stimulation of synaptically connected dissociated neurons does not readily induce plasticity

(A.1.2) Rationale and current-clamp stimulation

I sought a means to test the hypothesis that neurons with weak inward current responses to rBDNF application would be less likely to undergo potentiation than neurons with strong inward current responses. Bi & Poo (1998) produced one of a small number of reports describing plasticity between pairs of neurons in dissociated cultures in the presence of physiological magnesium concentrations. Lacking the availability of channelrhodopsins, these authors used low density neuronal cultures, with neurons supported by islands of glia cells and projecting to neurons on neighboring islands. Given the low number of neuronal cells and their more readily identifiable projections, the authors were able to perform dual perforated patch-clamp experiments and evoke LTP with a paired, low frequency stimulation protocol.

I found connected pairs of neurons in my higher density culture system difficult to find using two whole cell patch-clamping pipettes. With the availability of a wide variety of channelrhodopsins (Fenno *et al.*, 2011), however, paired stimulation experiments should be feasible in more typical higher density dissociated neuronal cultures, such as those used in my experiments. Transducing these cells with CheRiff (a highly sensitive channelrhodopsin; Hochbaum *et al.*, 2014) enabled me to quickly test neurons surrounding the recorded cell for synaptic connections. After entering whole cell configuration, the contents of the cytosol are washed out by the relatively large volume of electrolyte in the pipette. If too much time (reportedly 20 mins; Malinow & Tsien, 1990; Stevens & Wang, 1994) elapses between entering whole cell and starting the LTP stimulation protocol, then LTP cannot be induced – presumably because important components have been washed out from the cytosol. To overcome this complication, I used the perforated patch-clamp technique for all attempts to induce LTP. To ensure that the patch remained stable throughout the recording, baseline and post-stimulation recordings were carried out in voltage-clamp mode to allow measurement of the access resistance from the membrane capacitance transient (Marty & Neher, 1995).

I initially verified that the lightspot stimulation apparatus selectively stimulated single cells (AppFig1A). In the first LTP stimulation protocol attempted, I applied lightspot illumination of a presynaptic partner triggering single presynaptic action potentials before injecting current to trigger bursts of three spikes in the postsynaptic neuron (AppFig1B). Pre- and postsynaptic stimulation were separated by +10ms. Pairing was applied at a relatively low frequency of 5Hz. This was

below the frequency reportedly inducing potentiation in earlier study of spike timing-dependent plasticity (STDP) (Markram *et al.*, 1997; Sjöström *et al.*, 2001), but this earlier work used a one-to-one spike pairing protocol. Later it was reported that single action potentials at low pairing frequencies do not induce LTP, whereas low pairing frequencies with high frequency postsynaptic bursts of at least three spikes induces LTP (Kampa *et al.*, 2006). In the eight pairings made in perforated patch current-clamp configuration with a postsynaptic spike burst protocol, there is no indication that synaptic connections potentiated (AppFig1C).

Bursts of action potentials could facilitate LTP by triggering stronger depolarizations and, as a consequence, longer relief of NMDAR magnesium block. Binding of glutamate to NMDARs ensures selective activation of these receptors at stimulated synapses (Bliss & Collingridge, 1993). However, the optimal delay between pre- and postsynaptic stimulation to achieve maximum NMDAR calcium conductance may vary between inputs. This could be particularly true for dissociated neuronal cultures where inputs to the dendritic tree are likely to be more disordered. If distance-dependent learning rules exist for hippocampal neurons in primary cell culture as they appear to exist for L5 pyramidal neurons (Froemke *et al.*, 2005; Sjöström & Häusser, 2006; Letzkus *et al.*, 2006), then optimal delay for high frequency spike bursts to induce plasticity may even vary between inputs emanating from the same presynaptic partner neuron.

Before spike pairing protocols were established (Magee & Johnston, 1997; Markram *et al.*, 1997), LTP had been reported using low frequency presynaptic stimulation paired with long lasting depolarizations (Liao *et al.*, 1995; Isaac *et al.*, 1995). Using a pairing protocol such as this, which eliminates the time-dependent factor, might be necessary if optimal pairing delay is a difficult factor to control. Rather than stepping to 0mV, I ramped the voltage command to +30mV from -70mV resting command (AppFig2A). I favoured the ramp protocol because large voltage steps seemed more likely to result in patch rupturing. +30mV command was applied because this compensated for the additional series resistance inherent in perforated patch-clamp recordings (assuming a baseline voltage clamp of -70mV; see section 2.5). I carried out pairing protocols using HEPES-buffered extracellular solution (19 pairings) and bicarbonate-CO_2-buffered extracellular solution containing 200µM glycine (a cofactor necessary for NMDAR activation) (12 pairings). In neither case does the pairing protocol result in convincing, sustained potentiation (AppFig2B,C). Perhaps there is not a complete absence of potentiation (AppFig2D,E), but these faint, single examples pale in comparison to average potentiation reported in the literature from this type of stimulation protocol (50% from baseline; Markram *et al.*, 1997; Kampa *et al.*, 2006).

This absence of potentiation using an experimental design that should have delivered more encouraging signs of stable LTP prompts me to re-evaluate two assumptions that I held prior to

conducting these experiments. 1) The complete lack of any other publication since Bi & Poo reported their findings in the late 90's showing plasticity between pairs of neurons in cell culture is due to technical hindrances. 2) Successful LTP induction requires coincidence between glutamate binding to NMDARs and backpropagating spikes.

Conceivably, many other labs would have been interested in applying Bi & Poo's strategy for evoking LTP in cell culture, but to successfully carry out these experiments requires application of the more challenging perforated patch-clamp technique in an atypical culture system. This is indeed a source of discouragement, but channelrhodopsins have been available for over a decade to ease the experimental design and it is rather curious if other investigators have, in all this time, not attempted experiments similar to ones described in appendix figures 1 and 2. I have come to suspect that the difficulties I encountered in my attempts to induce LTP (and difficulties others may have also encountered) lies in the second assumption that I made. This issue is discussed in depth in section 4.3, but, in brief, I believe that high density dissociated neuronal cultures lack local input cooperativity when pairs of neurons are stimulated (AppFig3C) and I hypothesize that this is essential for LTP induction at distal synapses where many synaptic connections are formed. LTP induction may be achieved at more proximal dendrites, which are in range of somatic depolarizations, but any induction at these locations will be partially blurred by non-potentiating connections to more distal locations. Thus, potentiation will, if it is detected, appear weak. In hippocampal slices (AppFig3A) or low-density cultures (AppFig3B), input cooperativity is more readily achieved because inputs receiving presynaptic stimulation are more likely to cluster on single dendrites compared to stimulated inputs in high density cultures.

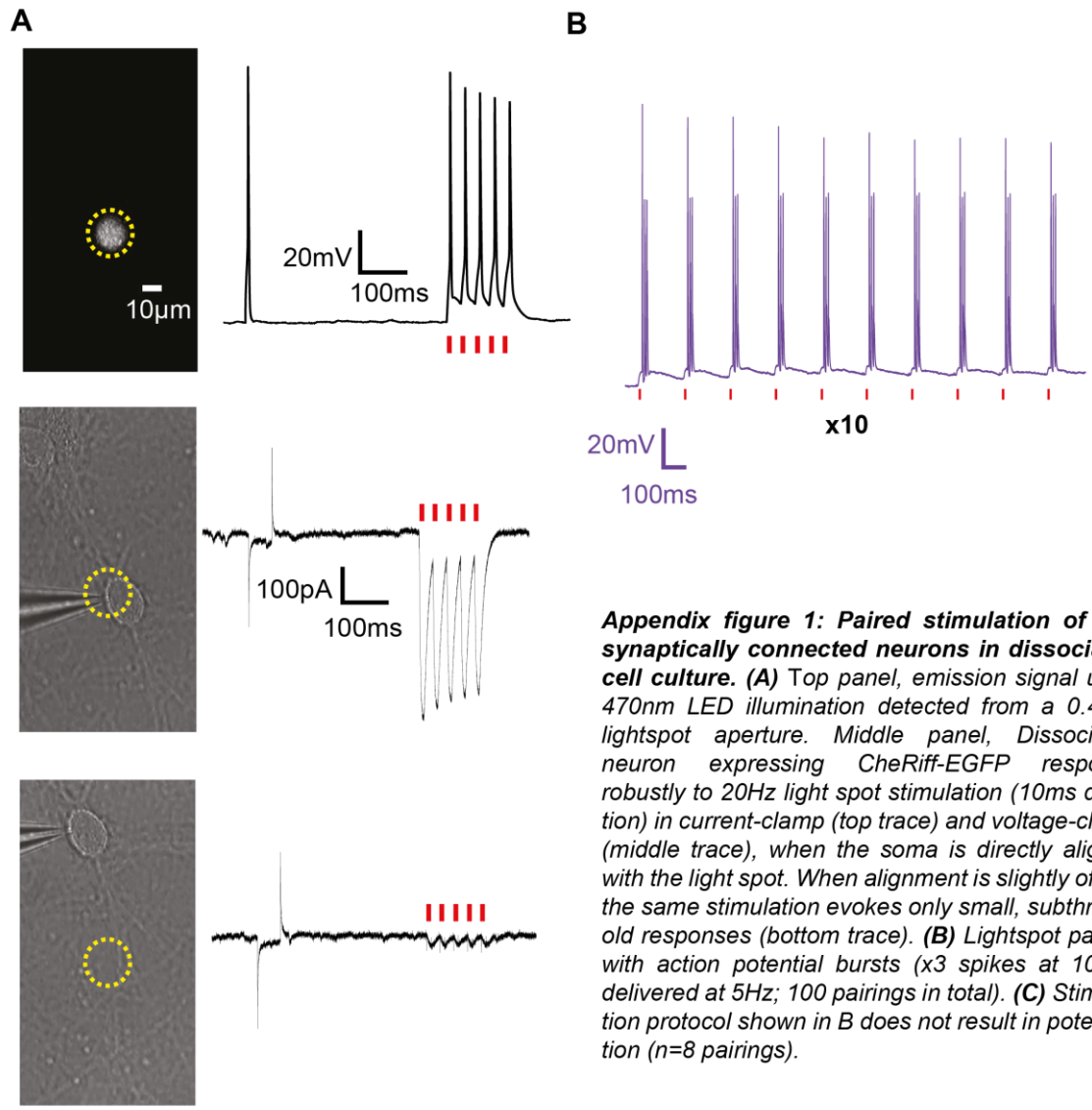

Appendix figure 1: Paired stimulation of two synaptically connected neurons in dissociated cell culture. ***(A)*** *Top panel, emission signal upon 470nm LED illumination detected from a 0.4mm lightspot aperture. Middle panel, Dissociated neuron expressing CheRiff-EGFP responds robustly to 20Hz light spot stimulation (10ms duration) in current-clamp (top trace) and voltage-clamp (middle trace), when the soma is directly aligned with the light spot. When alignment is slightly offset, the same stimulation evokes only small, subthreshold responses (bottom trace).* ***(B)*** *Lightspot pairing with action potential bursts (x3 spikes at 100Hz delivered at 5Hz; 100 pairings in total).* ***(C)*** *Stimulation protocol shown in B does not result in potentiation (n=8 pairings).*

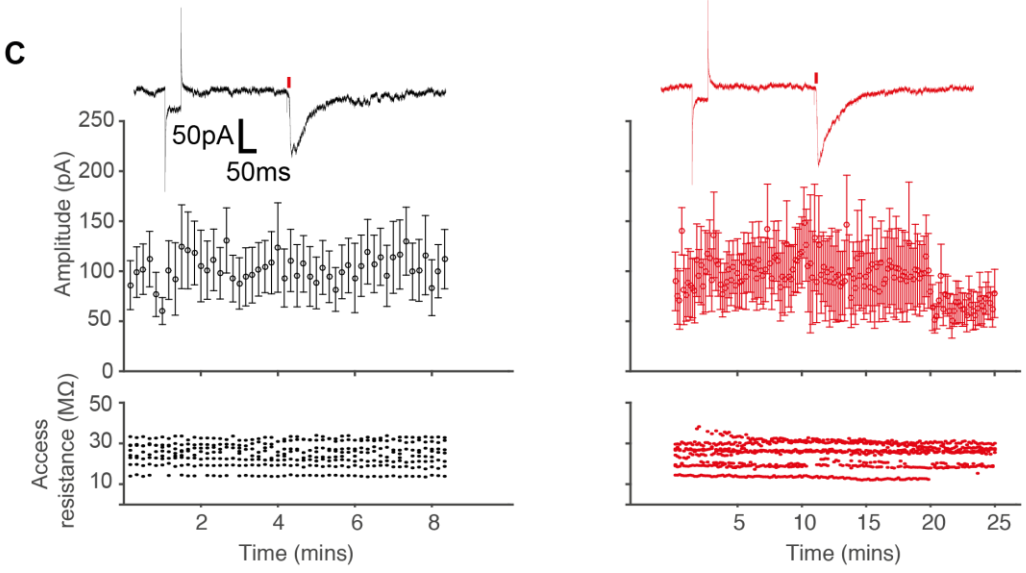

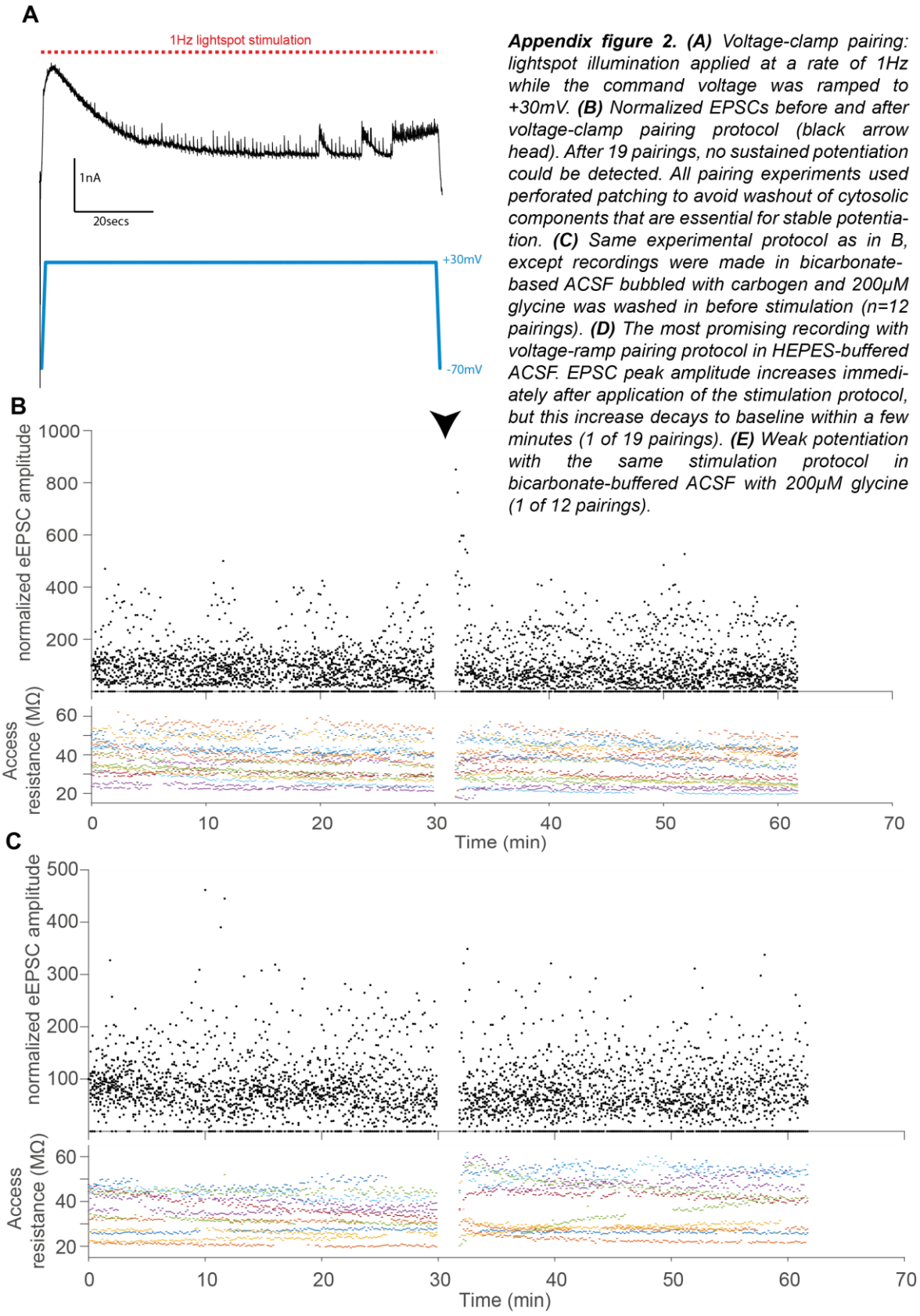

Appendix figure 2. ***(A)*** *Voltage-clamp pairing: lightspot illumination applied at a rate of 1Hz while the command voltage was ramped to +30mV.* ***(B)*** *Normalized EPSCs before and after voltage-clamp pairing protocol (black arrow head). After 19 pairings, no sustained potentiation could be detected. All pairing experiments used perforated patching to avoid washout of cytosolic components that are essential for stable potentiation.* ***(C)*** *Same experimental protocol as in B, except recordings were made in bicarbonate-based ACSF bubbled with carbogen and 200μM glycine was washed in before stimulation (n=12 pairings).* ***(D)*** *The most promising recording with voltage-ramp pairing protocol in HEPES-buffered ACSF. EPSC peak amplitude increases immediately after application of the stimulation protocol, but this increase decays to baseline within a few minutes (1 of 19 pairings).* ***(E)*** *Weak potentiation with the same stimulation protocol in bicarbonate-buffered ACSF with 200μM glycine (1 of 12 pairings).*

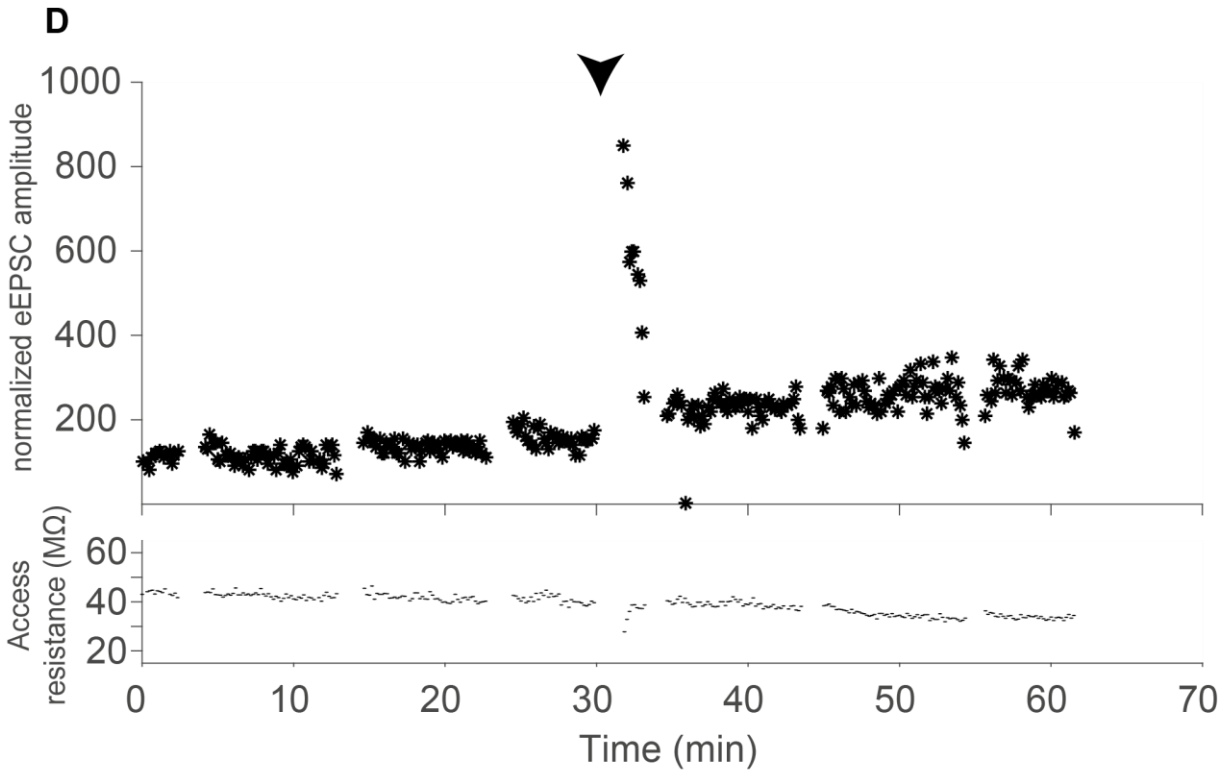
D
normalized eEPSC amplitude
1000
800
600
400
200
Access resistance (MΩ)
60
40
20
0
10
20
30
40
50
60
70
Time (min)

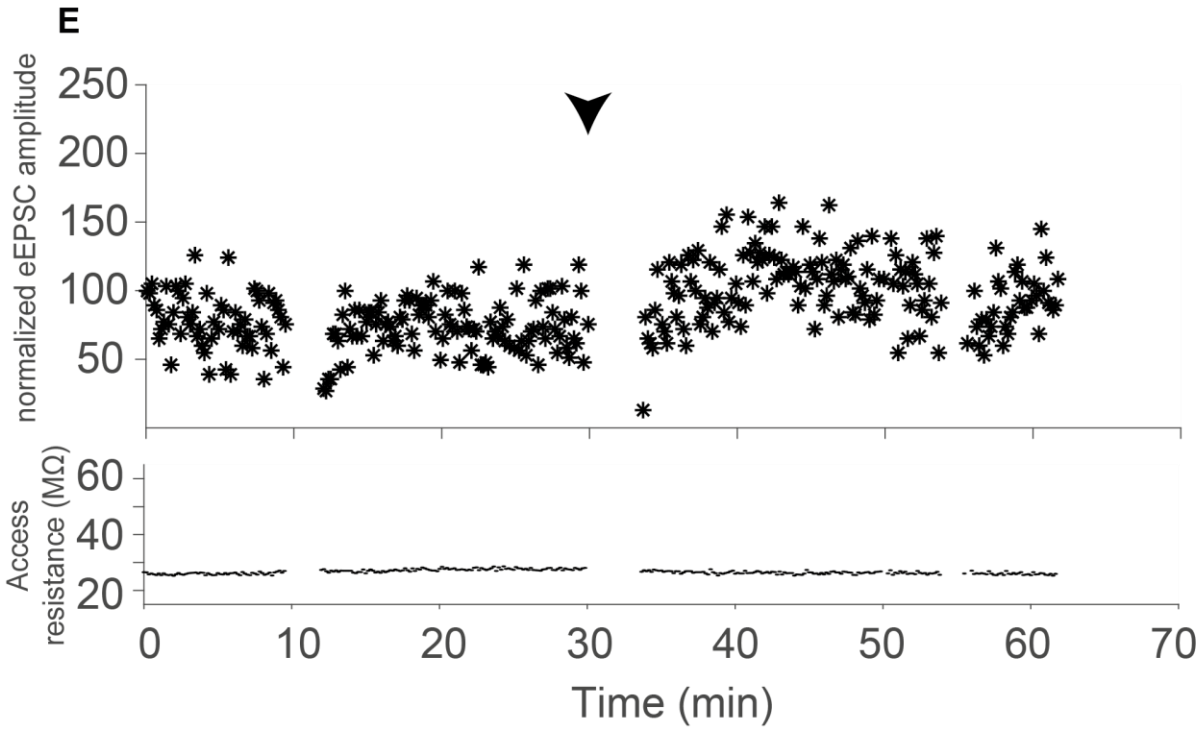
E
normalized eEPSC amplitude
250
200
150
100
50
Access resistance (MΩ)
60
40
20
0
10
20
30
40
50
60
70
Time (min)

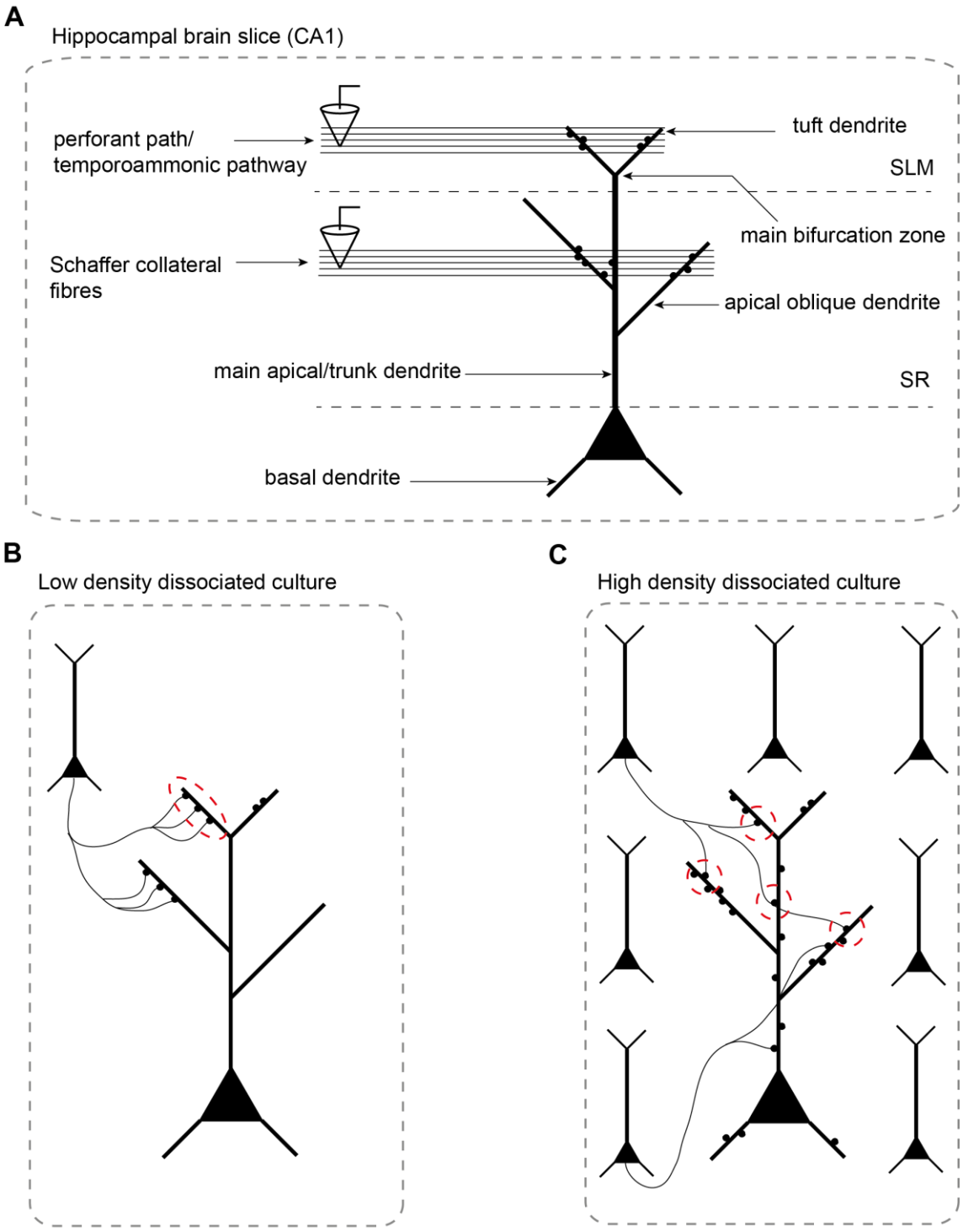

Appendix figure 3. Input cooperative on single dendrites cannot be achieved with paired stimulation of two neurons in high density dissociated cultures. *(**A**) LTP is readily evoked in hippocampal brain slices by recording from CA1 neurons and stimulating in the stratum lacunosum-moleculare (SLM) or the stratum radiatum (SR). Stimulation is likely to recruit multiple fibres projecting to either proximal (trunk/oblique) or distal (tuft) dendrites. Fibres follow predictable projections to CA1 dendrites and are likely to cluster on the same dendrites. (**B**) A small pool of possible presynaptic neurons in low density dissociated cultures (Bi & Poo, 1998) is likely to result*

*in anatomical synaptic clustering (red ellipse). (**C**) High density dissociated cultures are likely to have more distributed synaptic connections between cell pairs (see section 4.3 for further discussion).*

Discussion

(4.1) Exogenous application of BDNF

(4.1.1) Outward current response to rBDNF

By pressure applying recombinant BDNF to a final concentration of approximately 100ng/ml, I have detected both an outward and an inward current response to exogenous BDNF (Fig1). Although these current responses and the somatic calcium transient (most likely triggered by the inward current) may not occur under more physiological conditions, the size of the response – particularly the inward component – may nevertheless be indicative of physiologically interesting phenomena. For example, larger response amplitudes could be indicative of higher concentrations of surface-expressed BDNF receptors. Interesting questions that would arise from a correlation between TrkB surface expression and magnitude of the BDNF response include: does increased receptor surface expression correlate with increased LTP expression at the single cell level?

There are two known structurally unrelated BDNF receptors in the mammalian brain – tyrosine receptor kinase (TrkB) and pan neurotrophin 75 (p75) receptor (Dechant & Barde, 2002; Lu, 2003). The inward current component is most likely linked to TrkB activation because several studies have shown that TrkB activation triggers inward currents in hippocampal neurons. However, the VGCC-sensitive calcium influx (Fig2B), which is probably activated by these inward currents, is prominent in floxed-TrkB mouse neurons expressing Cre recombinase for at least five days (Fig2C;Fig4B). Compared to other synaptic proteins, TrkB has a relatively fast turnover rate – with a half-life of 0.7 days (Cohen *et al.*, 2013). At five days post-transfection with a Cre recombinase construct (under the control of the strong neuronal promoter for synapsin), I would expect TrkB expression in transfected neurons to be below 10% of wildtype expression. My results clearly show a strong response to rBDNF in Cre-expressing floxed-TrkB neurons. All mouse pups used in the preparation of cultures containing BDNF-responding, Cre-expressing neurons were homozygous for the floxed TrkB allele. These findings lead me to conclude that the inward current response I initially detected is not dependent on TrkB activation.

(4.1.2) G-protein coupled inwardly rectifying channels

Without invoking TrkB activation, it is difficult to account for the inward current component in response to rBDNF. It is also difficult to account for the outward component because all previous accounts of membrane current responses to rBDNF made no reference to an outward current. The outward component occurred during the application of rBDNF and was revealed by depolarizing voltage steps. Of the two BDNF receptors – TrkB and p75 – only p75 receptor activation has been

linked to the occurrence of an outward current (Coulson *et al.*, 2008). As with TrkB receptors, p75 receptors are not ionotropic. P75 relies on intracellular signalling cascades to link their activation to the gating of other, channel-forming, proteins. Through intracellular second messengers, p75 can promote both cell survival and death (Dechant & Barde, 2002).

Coulson *et al.* (2008) measured outward currents in HEK293 cells. This current is dependent on co-expression of G-protein coupled inwardly rectifying potassium (GIRK) channels and the C-terminal fragment of the p75 receptor. Co-expression of activated p75 receptors and GIRK channels in HEK293 cells (which, as Coulson et al showed, have no endogenous expression of these proteins) led to increased cell death, which depends on potassium efflux through GIRK channels. Coulson et al showed that overexpression of p75 C-terminal fragments in mouse dorsal root ganglion neurons leads to increased cell death, but this can be reduced through co-expression of dominant negative GIRK channels.

GIRK channels are tonically activated via binding BetaGammaG-protein subunits and phosphatidylinositol 4,5-biphosphate (PIP2) (Huang *et al.*, 1998; Kobrinsky *et al.*, 2000). Coulson et al found that p75 receptor signalling products still increased the rate of cell death even in the presence of G-protein-inactivating pertussis toxin. Furthermore, Coulson et al, found that PIP2 levels increased, in a Rac GTPase-dependent manner, following expression of activated p75 receptor in cell cultures. These results led Coulson et al to the conclusion that p75 receptor activity triggers GIRK activation via a phosphatidylinositol signalling pathway in neurons.

Could p75 receptor coupling to GIRK channels account for the outward current response I observed to rBDNF application? Chloride or potassium ions are the most plausible mediators of the outward current that I measured given the composition of my internal and extracellular solutions (section 2.5). As BDNF receptors are not ionotropic receptors, the activated BDNF receptor must be linked through a second messenger signalling pathway to either a potassium or chloride channel. No chloride channel linked to a second messenger signalling pathway has been described and GIRK channels are the only known potassium channel subtype to be activated via second messengers, except calcium ions (Hille, 2001).

Another consideration is the timing of the outward current. Current onset occurred within one second of rBDNF application, so p75-GIRK signalling would need to have a time scale in the 100ms range. GIRK channel currents activate in response to $GABA_B$ (Lüscher *et al.*, 1997) and muscarinic (Sadja *et al.*, 2002) receptor activation, but it is not clear from these studies if GIRK signalling could be triggered rapidly enough following p75 receptor activation. It is possible that

exposure to other signalling molecules, such as the G-protein subunit G-betagamma, (before exposure to PIP2) speeds up the time course of GIRK channel activation (Huang *et al.*, 1998).

(4.1.3) Inward current response to rBDNF

Despite the occurrence of the inward current component being apparently independent of TrkB expression, I suggest that cross-talk between the proposed p75-GIRK pathway and part of the BDNF-TrkB signalling pathway could account for this prominent current. TrkB activation has been shown to activate canonical transient receptor potential (TRPC3) channels expressed in the plasma membrane via activation of phospholipase C gamma (PLCgamma) (Li *et al.*, 1999). PLC-gamma metabolizes PIP2 to inositol triphosphate (IP3) and diacylglycerol (Berridge & Irvine, 1989). Increased concentrations of IP3 and diacylglycerol activate TRPC subtypes TRPC6 and 7, as well as TRPC3 (Albert, 2011).

Electrophysiological measurements of TRPC-mediated currents triggered by BDNF-TrkB signalling were reported by Pozzo-Miller and colleagues in hippocampal brain slices. In this study, Li *et al.* (2010) stimulated mossy fibre boutons, in the presence of blockers for ionotropic and metabotropic glutamate receptors, to elicit an inward current (I_{BDNF}) with similar kinetics to the inward current I observed. The I_{BDNF} observed by Li *et al.* (2010) could be significantly reduced in amplitude by the BDNF scavenging antibody (TrkB-IgG) or by knocking down TRPC3 expression in CA3 neurons. PIP2 is necessary for GIRK channel activation (Huang *et al.*, 1998) – which might mediate the outward current I observed – and the metabolic product of PIP2, IP3, could account for the inward current – through calcium-dependent insertion of TRPC receptors. However, it is not clear what signal increases PLC-gamma activation if TrkB signalling is not involved. Via an as yet unknown pathway, p75 receptor activation would have to trigger PLC-gamma activation.

I carried out control experiments where I pressure applied solutions containing buffering compounds present with lyophilized BDNF supplied by R&D Systems (Fig3A,B). The results from these experiments suggested that some response could be detected if these compounds are present at the high concentrations tested. The concentrations that I tested were approximately double the expected final concentration of these compounds. Using these concentrations has helped to illustrate the strong response still present in Cre-expressing floxed-TrkB neurons (Fig3C), but it is unclear from these experiments how much of the response is truly an artifact arising from higher salt concentrations. Indeed, hyperosmotic solutions did not strongly induce somatic calcium transients in a small number of experiments (Fig3D). As such, it remains necessary to test different concentrations of buffering compounds and other factors, which could

account for the outward and inward current components that emerge in response to rBDNF application.

(4.1.4) Summary: inward and outward currents in response to rBDNF application

p75 receptors could trigger activation of GIRK channels via G-protein and PIP2 second messengers (Coulson *et al.*, 2008), which would then mediate the outward current I detected during rBDNF application. Because p75-GIRK signalling is known to depend on the presence of PIP2, p75 receptor activation could lead to the generation of PIP2 necessary for IP3 production, which also leads to insertion of TRPC channels into the plasma membrane thereby enabling an inward current, which I also detected. However, critical uncertainties remain. In particular, what would trigger PLC-gamma activation to promote metabolism of PIP2 in the absence of TrkB activation? Currently, there exists no evidence for ligand-bound p75 receptor triggering PLC-gamma activation. Furthermore, numerous studies have reported different current responses to rBDNF application (Blum *et al.*, 2002; Amaral & Pozzo-Miller, 2007). None of these previous reports showed responses to acute application of rBDNF during voltage steps and there is only one publication describing a biochemical link between a BDNF receptor and a channel that could plausibly mediate a neurotrophin-induced outward current (Coulson *et al.*, 2008). If the outward current depends on p75 receptor activation, this would be a novel finding in need of further investigation.

(4.1.5) AARG analysis and rBDNF application

A procedure for analyzing spontaneous synaptic calcium transients with the bare minimum of user input is needed for analyzing events from large number of spines. Such a procedure would be interesting for the analysis of calcium transients occurring in response to synaptically active recombinant compounds such as BDNF. I hypothesized that the inward current response I detected following rBDNF activation reflects different levels of TrkB expression at synapses across the dendritic tree. However, employing AARG to test this prediction would have been premature considering I did not find evidence that the rBDNF current response depends on TrkB activation. I used AARG to show, in the case of one Cre+ floxed-TrkB neuron (Fig4B), that there is a robust fluorescence signal across most synaptic sites at the expected time point following rBDNF application. This result suggests that rBDNF-sensitive TrkB knockout neurons are responsive to rBDNF throughout the dendritic tree and not just in the soma.

I anticipate that with improved characterization of the rBDNF current/calcium response, similar experiments could be carried out that will reveal site-specific BDNF signalling properties in cultured neurons or neurons in more physiological preparations. Other soluble compounds known to alter

synaptic function could be applied in a similar manner. These types of experiments become more important for understanding synaptic function when one considers the profound impact synaptic location, along the dendritic axes, has on function and how relatively little experimental work has been directed at this issue (see section 1.2.6). However, rather than testing other synaptically active compounds using AARG analysis, I tested the effect different VGCC blockers would have on the amplitude of SSCTs.

(4.2) Distance-dependent VGCC contribution to SSCTs

(4.2.1) Blockade of VGCCs

Cadmium and nickel ions emerged as generic blockers for VGCCs with cadmium showing preferential block of CaV1 channels over LVA channels (Snutch *et al.*, 2013). CaV3 channels can be blocked by cadmium, zinc and nickel ions with nickel being the most potent (Snutch *et al.*, 2013), but nickel is not specific for LVA channels. CaV2.3 channels are also blocked by concentrations of nickel known to inhibit CaV3 channels (Metz *et al.*, 2005; Tai *et al.*, 2006).

Until the introduction of more selective and potent blockers for CaV3 channels (specifically, TTA-P2; see Shipe *et al.*, 2008; Choe *et al.*, 2011), nickel has been used extensively to study the role calcium channels in synaptic transmission (Wolfart & Roeper, 2002; Yasuda *et al.*, 2003; Kampa *et al.*, 2006; Takahashi & Magee, 2009; Larkum *et al.*, 2009). Mibefradil was also used as a blocker of T-type currents, even though it has been shown to block others – notably R-type currents (Randall & Tsien, 1997) and P/Q-type currents (Jiménez *et al.*, 2000).

Nimodipine is perhaps the most commonly used dihydropyridine drug treated as a selective L-type current antagonist, but, like nifedipine (another dihydropyridine) it has been shown to block CaV3 channels in the low 10s of micromolar range (McDonald *et al.*, 1994; Randall & Tsien, 1997). In this section, I will offer an interpretation of my findings from AARG analysis to evaluate the sensitivity of SSCTs to different VGCC blockers, in light of the specificity issues that exist for most VGCC antagonists.

(4.2.2) Non-specific blockers and CaV1 channels

Cadmium and mibefradil are two of the less specific pharmacological agents used to block VGCCs. Cadmium ions enter cells – possibly through NMDAR and VGCC pores – and cause toxicity after long exposure times (Usai *et al.*, 1999). The decrease in SSCT amplitudes across all regions of the dendritic tree that I detect with 100µM cadmium (Fig10A,B), could be partially explained by cadmium acting as a competitive antagonist to calcium entry through NMDARs and

weakly binding to GCaMP6s or not at all. 10µM mibefradil also reduces the SSCT amplitude across all dendritic regions of the cell (Fig10A,B), which could also arise from off-target effects of this drug. Other than blocking R-type and P/Q-type currents in addition to T-type currents, mibefradil can block sodium, potassium and chloride channels (Perez-Reyes, 2003). Partial blockade of potassium currents by mibefradil (IC50 = 4.65µM for Kv4 channels; Gomora *et al.*, 1999) could lead to depolarization of the resting membrane potential and increased release probability – which would account for the increased frequency of events I detected with 10µM mibefradil (Fig10E).

As with 100µM cadmium chloride and 10µM mibefradil, 10µM nimodipine reduced the amplitude of SSCTs across all three dendritic classifications (Fig10A,B), suggesting that nimodipine-sensitive VGCCs are present throughout the dendritic tree. Unlike cadmium and mibefradil, these findings cannot be easily dismissed as a result of off-target effects, because 10µM nimodipine is known only to block CaV1 and CaV3 channels (Randall & Tsien, 1997). It has no effect on R-type currents measured in Purkinje neurons (Randall & Tsien, 1995) and my results show that the specific CaV3 channel block has no effect on distal (>secondary) dendrites (Fig10C,D; Fig11). This implies that the remaining component in distal dendrites is driven by CaV1 channels.

CaV1 expression is thought to occur mainly in the soma and basal dendrites of hippocampal pyramidal neurons (Catterall, 2011; Snutch *et al.*, 2013) – a conclusion that is based mainly on immunohistochemical data (Hell *et al.*, 1993). Cell-attached recordings along the apical dendrites of CA1 neurons also suggest that HVA-type VGCCs, such as CaV1 channels, are present in higher concentrations in proximal regions of the main trunk dendrites compared to distal regions (Magee & Johnston, 1995*a*). Although informative, immunohistochemical studies are difficult to quantify and may be confounded by lack of epitope availability in situ, while cell-attached recordings such as those carried out by Magee & Johnston (1995) may still be prone to voltage errors (Williams & Wozny, 2011). These voltage errors arise due to unintended transmembrane voltage fluctuations that occur during application of voltage steps or voltage ramps used to characterize dendritic expression and properties of ion channels (Williams & Wozny, 2011). Furthermore, cell-attached recordings have limited access to the dendritic tree. Only thick dendrites such as the main apical of pyramidal neurons can be patched, while thinner dendrites in more distal regions are inaccessible. Using a timelapse imaging approach I have detected nimodipine-sensitive VGCCs in distal parts of cultured hippocampal neurons (Fig10A,B), which are most probably a population of CaV1 subtypes. These results would need to be followed up by more physiologically-relevant preparations to determine whether or not CaV1 channels are present at distal synapses in the living brain.

(4.2.3) CaV2 channels: synaptic integration

Previous studies indicate that CaV2.2 channels (which conduct the N-type current) are not strongly associated with spine calcium transients (Sabatini & Svoboda, 2000; Bloodgood & Sabatini, 2007). CaV2.2 channel contributions to synaptic transmission may be confined to presynaptic terminals, where a close association between SNARE proteins and calcium sources is required for calcium-dependent vesicle fusion (see section 1.1.2). CaV2.2 channels bind to SNARE proteins in isolation or in various combinations (Atlas, 2001). Formation of these SNARE-CaV2.2 complexes appears to be important for correct docking and/or priming of synaptic vesicles for fusion (Catterall, 1999; Atlas, 2001).

CaV2.2 channels may be expressed postsynaptically in cultured hippocampal neurons. However, consistent with this channel having a predominately presynaptic role in synaptic transmission, I detect only a slight contribution from CaV2.2 in generating SSCTs compared to CaV2.3 and CaV3 channels (Fig10C,D; Fig11), which appear to have a more dominant role in promoting postsynaptic calcium transients.

As outlined in section 1.2.4, SNX-sensitive CaV2.3 channels are one of the main contributors to spine calcium transients (Sabatini & Svoboda, 2000; Bloodgood & Sabatini, 2007). Activation of small conductance potassium (SK) channels appears to depend on opening of CaV2.3 channels in dendritic spines of hippocampal (Cai *et al.*, 2004; Bloodgood & Sabatini, 2007; Giessel & Sabatini, 2010) and layer 5 (Bock & Stuart, 2016) pyramidal neurons. Coupling of SK and CaV2.3 channels may help control the extent of supralinear summation arising from synchronously active inputs in these cell types (Cai *et al.*, 2004; Bock & Stuart, 2016). Supralinear summations are dendritic depolarizations with simultaneous, or near-simultaneous, time courses and amplitudes that exceed those which would be expected from a linear relationship between increasing stimulation intensity and the measured response (Schiller *et al.*, 2000; Magee, 2000). Dendritic spikes are examples of supralinear summation and can depend principally on NMDAR (Schiller *et al.*, 2000), dendritic voltage-gated sodium channels (dVGSCs) (Golding & Spruston, 1998; Kim *et al.*, 2015) or VGCCs (Larkum *et al.*, 1999; Takahashi & Magee, 2009). Often dendritic spikes have been less carefully defined and are sometimes described as ‘plateau potentials’ (Cai *et al.*, 2004; Takahashi & Magee, 2009; Bock & Stuart, 2016). Dendritic spikes are of great interest because they suggest a mechanism by which neurons could detect coincident events in the absence of bAPs (Schiller *et al.*, 2000). This point is discussed in greater depth in section 4.3.8.

Several studies have shown that blockade of SK channels with the specific antagonist apamin, leads to a broadening (Cai *et al.*, 2004) or an increase in amplitude (Bock & Stuart, 2016) of dendritic spikes. Bock & Stuart (2016) measured dendritic spikes dependent on NMDAR activation

from L5 pyramidal neurons using iontophoretic application of glutamate to trigger supralinear summation of membrane potential fluctuations in basal dendrites. Bath application of 100nM apamin increased the amplitude of NMDAR-dependent supralinear potentials (NMDAR spikes) without altering baseline properties of the cell (such as membrane resistance). Co-application of SNX-482 to block CaV2.3 channels removed this effect, suggesting that activation of SK channels depends on CaV2.3 conductance. In hippocampal pyramidal neurons, exposure to 100nM apamin increases the duration of dendritic spikes (Cai *et al.*, 2004) while 0.3µM SNX-482 and 100nM apamin reduce amplitudes of spine calcium transients (Bloodgood & Sabatini, 2007). Together, these findings suggest that calcium influx through CaV2.3 channels may be part of a generic negative feedback mechanism, helping to control local integration of synaptic inputs.

CaV2.3 channels contribute to spine calcium transients (Sabatini & Svoboda, 2000; Bloodgood & Sabatini, 2007) and form part of a negative feedback mechanism to limit activation of spines (Bloodgood & Sabatini, 2007; Bock & Stuart, 2016) through coupling to SK channels, which repolarize local membrane voltages. I have applied AARG analysis to further evaluate the contribution of CaV2.3 channels to spine calcium transients along increasingly distal segments of the dendritic tree of cultured hippocampal neurons. Taking this approach, I have shown that CaV2.3 channels contribute to NMDAR-dependent, spontaneous spine calcium transients (SSCTs) (Fig10C,D; Fig11). Secondary dendrites, which would correspond to proximal tuft dendrites and oblique apical dendrites in pyramidal neurons seem to be more sensitive to CaV2.3 blockade than more distal dendrites or thin primary dendrites (Fig11).

(4.2.4) CaV2 channels: control of spiking modes

Numerous neuronal cell types in the CNS maintain different firing modes – including pyramidal neurons of the hippocampus (Spruston & McBain, 2006). These neurons fire single spikes with clear after-hyperpolarization potentials (AHPs) or spike bursts at frequencies of 100Hz aided by after-depolarization potentials (ADPs) (Magee & Carruth, 1999; Spruston & McBain, 2006). Group I metabotropic glutamate receptors (mGluRs) are known to increase neuronal excitability by reducing post-spike AHPs (Ireland *et al.*, 2004). (Park *et al.*, 2010) showed that a post-burst ADP (pbADP) in CA1 neurons depends on activation of both group I mGluRs and CaV2.3 channels. These authors applied small current injections into CA1 neurons held in current clamp to trigger pbADPs in the presence of DHPG (a group I mGluR agonist). Although the pbADP was blocked by 1µM TTX, larger current injections, which triggered calcium spikes, could rescue pbADPs. This is an interesting finding because it is consistent with calcium spikes being critical for increased firing (and possibly bursting) behaviour of hippocampal pyramidal neurons – similar to the role calcium spikes are thought to have in layer 5 pyramidal neurons (see section 4.3.7). The authors showed

that pbADPs require extracellular calcium and activation of nickel-sensitive VGCCs. 100µM nickel chloride was required to block approximately 75% of the pbADP – this is a higher concentration than expected for blockade of CaV2.3 channels, given reports from others (Tai *et al.*, 2006). Nevertheless, crucial experiments from knockout mice lacking the CaV2.3 alpha1 subunit show that CA1 neurons depend on CaV2.3 expression for pbADPs.

The hippocampus receives neuromodulatory inputs from the cholinergic pathway, which are thought to control oscillatory patterns of activity within the intact strata of the hippocampus (Teles-Grilo Ruivo & Mellor, 2013) and facilitate memory encoding (Larson & Munkácsy, 2015). Findings from Tai *et al.* (2006) suggest that activation of the cholinergic receptors by 2µM carbachol triggers CaV2.3-dependent calcium spikes. Tai *et al.* (2006) showed that 2µM carbachol selectively increases the HVA calcium channel component in CA1 neurons from acute brain slices, while not altering the current-voltage relationship in the LVA component. Based on these initial findings, the authors expect that 50µM nickel inhibited calcium spikes through blockade of HVA CaV2.3 channels, rather than LVA CaV3 channels.

In summary, CaV2.3 channels play multifunctional roles controlling integration of both inputs and coordination of outputs. Although it is not always clear whether CaV2.3 or CaV3 channels are principally involved. Both are sensitive to low (40-50µM) nickel and some CaV2.3 channels are resistant even to SNX-482 blockade (Tottene *et al.*, 2000). SSCT amplitudes decreased following application of 0.5µM SNX-482 in primary and secondary dendrites (Fig10C,D) and this effect was maintained in secondary dendrites when thicker dendrites were excluded from analysis (Fig11). Higher expression of CaV2.3 channels in secondary dendrites may be necessary to support supralinear dendritic processes such as dendritic calcium spikes.

(4.2.5) CaV3 channels: control of spiking modes

CaV3 channels have distinctive gating characteristics compared to HVA channels (Randall & Tsien, 1997; Perez-Reyes, 2003). CaV3 channels become inactivated with increasingly depolarized membrane potentials (Randall & Tsien, 1997) and must be de-inactivated before it is possible for the channel to become activated again (Simms & Zamponi, 2014). CaV3 channels de-inactivate when membrane potentials hyperpolarize and once in a de-inactivated state, these channels – being LVA channels – require relatively small voltage deflections to become activated and open (Randall & Tsien, 1997; Perez-Reyes, 2003). These properties enable CaV3 channels to play a central role in switching firing states in multiple types of neurons, including thalamocortical relay neurons, Purkinje neurons and dopaminergic neurons in the substantia nigra (Lambert *et al.*, 2014). Many CaV3 channels will be active near the resting membrane potential, which promotes

low threshold spiking in rhythmically firing neurons of the thalamus (Perez-Reyes, 2003) and inferior olive (Lambert *et al.*, 2014). If CaV3 channels form protein complexes with small conductance (SK) calcium-activated potassium channels, their function of promoting burst firing by tonically depolarizing the resting membrane potential can be inverted (Wolfart & Roeper, 2002). Under these conditions, calcium entry through CaV3 channels activates SK channels to limit further depolarization of the membrane and spiking (Wolfart & Roeper, 2002).

(4.2.6) CaV2.3/3 channel contribution to calcium spikes

Besides influencing the firing rate for somatic spikes, CaV2.3 and CaV3 channels may also be involved in controlling dendritic calcium spikes. (Larkum *et al.*, 1999) described a dendritic calcium event that depended on coincident synaptic activity in the apical tuft of layer 5 pyramidal neurons and a bAP. When a L5 spike was closely followed (3-7ms) by synaptic stimulation, then a calcium spike would be triggered – initiated within a "hotspot" of the main apical dendrite. This calcium spike appears to trigger bursts of somatic spikes. In a more recent study, Larkum and colleagues were able to patch apical tuft dendrites and measure non-linear voltage fluctuations associated with NMDAR activation in response to synaptic stimulation. None of these supralinear voltage changes were sensitive to 100µM cadmium or 100µM nickel. 1µM TTX slowed the speed of the voltage change, but did not alter the size of the integral. Only 50µM AP5 abolished the supralinear component of this voltage fluctuation. Stimulating two branches simultaneously to trigger supralinear voltage deflections could trigger calcium spikes in the proximal region of the dendrites (near the central bifurcation point of the main apical dendrite). In the modelling part of their study, Larkum *et al.* (2009) found that NMDAR spikes were essential for reducing the number of synapses in the tuft that were needed to trigger a calcium spike. Furthermore, in order to better fit their model to experimental data, a heterogeneous distribution of VGCC conductance was required, with a higher proportion of channels inserted in the central bifurcation zone of the main apical dendrite than in other regions.

In experiments I carried out with more specific VGCC blockers, SNX-482 and TTA-P2 continued to reduce peak SSCT amplitudes even after controlling for uneven distributions of diameters across branch categories (Fig11). Overall, VGCCs in secondary dendrites made a larger contribution to secondary dendrites compared to other branch types under the experimental conditions tested here (Fig11). This result may reflect the uneven distribution of VGCCs, which could support activation of supralinear dendritic events (Larkum *et al.*, 2009; Almog & Korngreen, 2016). This is an interesting possibility, but further experiments would be needed to verify if VGCCs expressed in electrochemically isolated spines can support calcium spikes in hippocampal pyramidal neurons beyond a primary cell culture model.

Calcium ions are charge carriers as well as second messengers (Perez-Reyes, 2003). This dual capability seems to enable VGCCs to drive local calcium spikes in pyramidal neurons (Larkum *et al.*, 1999; Takahashi & Magee, 2009), which may rely on local hotspots where higher densities of VGCCs are expressed (Larkum *et al.*, 2009) and drive bursts of somatic spikes (Major *et al.*, 2013). One possibility provided by AARG analysis is to quantify changes in SSCT amplitudes following exposure to different pharmacological agents – including VGCC blockers – while avoiding drawbacks associated with immunohistochemical or electrophysiological approaches (section 4.2.2). If VGCC subtypes are differentially expressed across the plasma membrane surface – which would be expected from the studies by Larkum and others – then this should be apparent in how SSCT amplitudes are affected by various antagonists in different sections of the dendritic tree. As outlined above, I have detected different levels of sensitivity to specific VGCC blockers across proximal and more distal compartments. The pattern I detected is consistent with a VGCC expression profile that supports calcium spikes.

(4.3) LTP

(4.3.1) Synapses of dissociated neurons in cell culture can potentiate

Dissociated hippocampal neurons establish synaptic connections after approximately one week with appropriate cell culture techniques (sections 2.2.1 and 2.2.2) and frequent calcium transients appear localized to dendritic spines (Fig5). In short, all the components for synaptic plasticity appear to be there and based on previous reports (Bi & Poo, 1998; Molnár, 2011) I should have detected more promising signs of potentiation.

Numerous publications describe some form of synaptic plasticity in primary neuronal cell cultures (Turrigiano, 2012). Cultured neurons from the neocortical, hippocampus and spinal cord are known to undergo homeostatic synaptic scaling (Turrigiano, 2012). Blockade of network activity or AMPAR activation for 2-3 days promotes a global increase in AMPAR expression at synapses of dissociated neurons, which can be detected as an increase in mEPSC amplitude or an increase in intensity of staining for surface GluA1 subunits (Turrigiano *et al.*, 1998; O'Brien *et al.*, 1998). Homeostatic synaptic scaling is a type of synaptic plasticity that is thought to balance overall synaptic strength such that relative differences between input strengths are maintained without the strongest synapses becoming excessively potentiated and inducing disease states, such as epilepsy (Turrigiano, 2008).

Hebbian, or Hebbian-like, plasticity is also well documented in dissociated neuronal cultures beyond the study by Bi & Poo (1998). These other studies relied on identifying synaptically connected pairs, applying high frequency stimulation to the presynaptic partner in 0 magnesium bath solution or providing somatic depolarization with low frequency presynaptic stimulation in physiological magnesium concentrations (Bekkers & Stevens, 1990; Arancio *et al.*, 1995). Alternatively, Hebbian-like plasticity was induced by chemical stimulation – often referred to a chemical LTP (cLTP) (Molnár, 2011). This type of synaptic plasticity appears to depend on the same mechanisms as classical Hebbian plasticity, such as calcium influx through NMDARs (Lu *et al.*, 2001) and CaMKII activation (Hayashi *et al.*, 2000), but lacks the input specificity that comes with electrode-evoked Hebbian plasticity.

(4.3.2) Chemical LTP

Treating dissociated cultures with 100-200µM glycine in the absence of magnesium is a standard cLTP stimulation protocol that has been used by multiple groups leading to increases in AMPAR content at synaptic sites (Lu *et al.*, 2001; Park *et al.*, 2004; Petrini *et al.*, 2009), which can be measured as an increase in mEPSC or an increase in GluA1 subunit staining (Lu *et al.*, 2001). Another approach has been to treat cells with 50µM forskolin and 0.1µM rolipram for 30 minutes. Forskolin activates adenylate cyclase, which synthesizes cyclic adenosine monophosphate (cAMP). Increased cAMP activates phosphokinase A (PKA), which phosphorylates AMPAR subunits GluA1 at ser-845 and limits NMDAR-induced internalization of the receptor (Ehlers, 2000). AMPARs are constitutively recycled at the postsynaptic membrane, so by reducing the number of receptors that are endocytosed, adenylate cyclase-activators can increase synaptic strength (Ehlers, 2000).

(4.3.3) LTP induction using electrodes

Clearly, the ability of dissociated neurons to undergo synaptic plasticity has been demonstrated by a large number of different groups. Yet only a small number (Arancio *et al.*, 1995; Bi & Poo, 1998) have reported the successful application of an induction protocol without resorting to removing magnesium and supplementing the extracellular medium with glycine or any other unphysiological form of stimulation. Hebbian LTP should be inducible in the presence of physiological ion concentrations in healthy, mature neuronal cell cultures.

A critical feature of older studies identifying pairs of synaptically connected neurons in dissociated cultures is that the investigators used a very low-density culture system (20-50,000 cells/ml in Bi & Poo (1998) compared to 160,000 cells/ml used in my culture preparation). In such a low-density culture system, each neuron will have relatively few synaptic partners and there is an increased

probability that immediately adjacent neurons form synaptic connections with each other. This is in contrast with higher density culture systems (such as the one I used), the chances of finding connected cell pairs amongst neighboring neurons is much lower and finding connected pairs with two micropipettes much less likely. In low density cultures, neighboring neurons are not only more likely to form connections with the recorded cell, they are likely to form multiple connections on the same dendritic branch (AppFig3B). Under these conditions and even with only one presynaptic partner being stimulated, input cooperativity can potentially play a more important role during LTP induction. In higher density cultures, inputs from the same presynaptic partner are much more likely to be spread across the dendritic tree (AppFig3C). Any synaptic organization found in vivo or in hippocampal brain slices – such as temporoammonic projections along stratum lacunosum-moleculare (SLM) (Remondes & Schuman, 2003) to distal tuft dendrites and Schaffer collateral inputs along the stratum radiatum (SR) to more proximal apical input sites of CA1 neurons (AppFig3A) – is lost.

Synaptic integration zones exist within the dendritic tree (sections 4.2.3 and 4.3.7) and LTP (at least in L5 pyramidal neurons) relies on distance-dependent induction rules (see section 1.2.6). The dendritic depolarization signal (bAP or input cooperativity) a synapse needs in order to stably potentiate may depend on its location within the dendrites. Most LTP studies have been carried out in hippocampal slices with three broad approaches taken: field recordings, whole cell patch-clamp combined with low frequency stimulation of CA1 efferents and whole cell patch-clamp combined with minimal intensity stimulation of CA1 efferents. Although hippocampal brain slices represent a very different system compared to the cell culture environment, there are too few LTP studies using electrode-based stimulation techniques in cell culture to make an accurate assessment of the possible explanations for the almost complete absence of potentiation in my experiments.

(4.3.4) LTP induction: brain slices and whole cell recordings

The earliest LTP studies in brain slices typically relied on high frequency (100Hz or more) field stimulation applied to bundles of axons projecting to CA1 neurons of the hippocampus (Bliss *et al.*, 2006). Stimulation is applied either as a single burst of high frequency pulses or shorter bursts with time intervals intended to mimic temporal dynamics of oscillations known to exist in vivo within the hippocampus (Larson & Munkácsy, 2015). The stimulation electrode is placed within the SLM or SR. The SLM contains axons from excitatory entorhinal cortical neurons projecting to the distal regions of CA1 dendrites, while the SR contains axons from CA3 neurons projecting to more proximal CA1 regions (this is known as the Schaffer collateral pathway). In this experimental design, the electrophysiologist has no control over the membrane potential of postsynaptic neurons. Therefore, synaptic stimulation alone has to provide both the synaptic depolarization and

more global dendritic depolarization, which coincide to trigger higher cytosolic calcium accumulations leading to LTP (section 1.2.1). Only higher stimulation frequencies (~100Hz) can provide sufficiently strong activation of synaptic inputs.

To study postsynaptic factors contributing to plasticity in brain slices, field stimulation techniques have been combined with single cell intracellular recordings (Gustafsson *et al.*, 1987) and somatic voltage-clamp experiments (Malinow, 1991). Using the voltage-clamp approach, somatic depolarization of a single CA1 neuron to the reversal potential for EPSCs (~0mV) is paired to low frequency stimulation of incoming fibres (Perkel *et al.*, 1993; Chen *et al.*, 1999). In these experiments, sufficiently long depolarization times are more important than high stimulation frequencies (Chen *et al.*, 1999). In addition, cesium is typically chosen over potassium as the principle cation in the pipette solution. Cesium is a non-specific blocker of potassium channels and thereby increases the surface area of plasma membrane that will be held at the command voltage (Chen *et al.*, 1999). An important limitation with this technique is that approximately 20 minutes after establishing whole cell configuration cytosolic components important for LTP induction are washed out by the relatively large volume of solution in the recording pipette (Bekkers & Stevens, 1990; Tanaka *et al.*, 2008).

(4.3.5) LTP induction: minimal stimulation

Another approach to studying LTP in hippocampal brain slices again involves whole cell patch-clamp of CA1 neurons, but with minimal stimulation of projecting axons. These experiments have been applied by a number of different groups during the 1980s and 1990s in an attempt to resolve questions concerning the locus of LTP expression at the synapse (Bliss & Collingridge, 2013). Some of these attempts involved applying quantal analysis, but achieved limited success due to the difficulties of applying this technique to CNS synapses (Bliss & Collingridge, 2013).

Quantal analysis is derived from the classic studies by Bernard Katz at the frog neuromuscular junction (Fatt & Katz, 1952; Del Castillo & Katz, 1954; Augustine & Kasai, 2007). These studies described synaptic transmission as being divisible into discrete packages of neurotransmitter – or “quanta” (Augustine & Kasai, 2007). Today, these quanta are known to be neurotransmitter-containing synaptic vesicles. The number of quantal events detected depends on three variables: N (for number of release sites), p (probability of release for a single event) and q (quantal size) (Bekkers & Stevens, 1990; Kerchner & Nicoll, 2008). These variables represent properties associated with both the presynaptic (N and p) and postsynaptic (q) side of the synapse (Kerchner & Nicoll, 2008). Kullmann & Nicoll (1992) applied quantal analysis to amplitude distributions of CA1 synaptic responses. These currents were evoked by minimal stimulation of Schaffer collateral

projections. By measuring changes in the pattern of amplitude distributions following LTP induction, Kullmann & Nicoll (1992) attempted to assess the likely contribution from pre- and postsynaptic compartments to LTP expression at Schaffer collateral-CA1 synapses. Quantal analysis assumes that a single synaptic site is being stimulated, but very few CNS projections are monosynaptic. Very often a single fibre will form multiple synapses on the same postsynaptic neuron (Bekkers & Stevens, 1990; Kerchner & Nicoll, 2008). This is one factor making results from studies such as Kullmann & Nicoll (1992) difficult to interpret. Furthermore, quantal analysis does not account for variance caused by cable filtering (Bekkers & Stevens, 1990) and, since hippocampal synaptic vesicle fusion may not be an all-or-nothing event (Rizzoli, 2014), the application of a binomial analytical approach such as quantal analysis may not be appropriate (Kerchner & Nicoll, 2008). Despite the drawbacks of quantal analysis, a highly consistent finding emerged from studies inducing LTP in the hippocampus through minimal stimulation: LTP induction leads to a decrease in the number of apparent 'failures' (Malinow & Tsien, 1990; Bekkers & Stevens, 1990; Stevens & Wang, 1994). In quantal analysis, this finding is interpreted as an increase in p, which means there is a higher probability for action potential propagation to the axon terminal to trigger vesicle fusion (Kerchner & Nicoll, 2008).

The consistent finding that LTP induction leads to a decrease in failure rate with minimal stimulation suggested that the locus of plasticity expression lies on the presynaptic side. However, other results complicated this interpretation. In whole cell SC-CA1 stimulation experiments, AMPAR-mediated EPSCs can be measured near the resting membrane potential (-60 to -70mV), while at positive command potentials (e.g. +55mV), NMDAR-mediated EPSCs are detected with the same stimulation. After LTP induction, failure rate for AMPAR-mediated EPSCs changed, while the failure rate for NMDAR-mediated EPSCs remained constant (Kullmann, 1994). It was also found that paired pulse facilitation for AMPAR-mediated EPSCs remained constant after LTP induction (Manabe *et al.*, 1993). If release probability increased following LTP induction, a decrease in failure rate should be detected at both command potentials and the paired pulse ratio (EPSC2/EPSC1 = PPR) should decrease.

In two studies (Liao *et al.*, 1995; Isaac *et al.*, 1995), a slightly different version of the minimal stimulation paradigm. Typically, a stimulus is applied to the Schaffer collateral fibres with decreasing intensity until no EPSC can be detected or until the EPSC matches the kinetic profile of miniature EPSCs (Raastad *et al.*, 1992). In these two studies, a similar approach was taken, but the stimulation intensity was decreased until 100 consecutive sweeps failed to evoke an AMPAR-mediated EPSC. Using this weaker stimulation, the authors showed that a NMDAR-mediated EPSC could be detected by changing the command potential to +55mV. Applying the same type of paired stimulation protocol that triggered an apparent decrease in failures (Bekkers & Stevens,

1990; Malinow & Tsien, 1990; Stevens & Wang, 1994), these later studies (Liao *et al.*, 1995; Isaac *et al.*, 1995) found that pairing triggered an emergence of an AMPAR-mediated EPSC with weak stimulation.

An increase in AMPAR conductance and/or AMPAR density in the postsynaptic membrane (section 1.1.3), is a major form of postsynaptic LTP expression. Clearly then, minimal stimulation experiments that probably activate only single fibres can induce typical forms of LTP. One common feature between all studies discussed above is that the experimental design involved minimal stimulation of the Schaffer collateral fibres in the SR. Inputs to the CA1, within the SR, target proximal sites along the main apical branch and oblique apical dendrites (AppFig3A). These proximal inputs may lie within range of bAPs and thus depend on bAPs in their plasticity induction rules. As recent findings have suggested (Froemke *et al.*, 2005; Sjöström & Häusser, 2006; Letzkus *et al.*, 2006), more distal inputs may depend on different induction rules.

(4.3.6) LTP induction: Importance of cooperativity between individual synapses

No study has explicitly applied minimal stimulation to distal synapses of the dendritic tuft in CA1 neurons (which can be targeted by stimulating fibres in the SLM). Spruston and colleagues applied weak stimulation to SLM bundles paired with appropriately timed bursts of three action potentials, which failed to induce LTP (Golding *et al.*, 2002). The same stimulation applied to axon bundles of the SR triggered LTP lasting for at least 30 minutes. In contrast, stronger stimulation in the SLM (with local application of 5µM TTX to the soma to block bAPs) induced LTP. This LTP was sensitive to both 50µM AP5 and a combination of 50µM nickel and 10µM nimodipine. Golding et al showed that local application of high TTX concentration to the soma blocks bAPs suggesting the LTP they measured depends on local events within the tuft dendrites. They also showed that the same bAP-independent LTP occurs at inputs in the SR, suggesting that bAP-independent LTP is not a feature found only in distal tuft dendrites. In a later study, the Spruston lab provided direct evidence that local depolarization in tuft dendrites is necessary for potentiation of perforant path – CA1(tuft) synapses (Kim *et al.*, 2015). Using a similar experimental design as in the earlier study (Golding *et al.*, 2002), Kim *et al.*, (2015) blocked dendritic voltage-gated sodium channels (VGSCs) with a low concentration (20nM) of TTX. 20nM TTX did not block somatic spikes because, as the authors reasoned, VGSCs are expressed at higher densities at the axon initial segment and along the axon than in dendrites. This makes VGSCs mediating somatic spikes less sensitive to low concentrations of TTX compared to dendritic VGSCs. As before, high concentrations of TTX could be locally applied to the cell body to block somatic action potentials. With this slightly modified experimental approach, Kim et al showed that bath-applied 20nM TTX completely abolished LTP in the perforant path – CA1(tuft) pathway. As in their previous study, 50µM AP5 and 10µM

nimodipine partially inhibited LTP. 50µM AP5 and 10µM nimodipine applied together completely abolished LTP.

Although no study has explicitly applied the minimal stimulation paradigm to distal SLM inputs of hippocampal pyramidal neurons, Spruston's teams came close to it by applying 'weak' stimulation. They could not induce LTP with the same weak stimulation protocol at distal (tuft) synapses that could induce LTP at more proximal inputs in SR. In their later study, they provide direct evidence for dendritic sodium spikes being necessary and sufficient for LTP induction at SLM inputs, while at proximal SR inputs, LTP is induced by dendritic sodium spikes or bAPs (Kim *et al.*, 2015). Together, these findings indicate that distal inputs are insensitive to bAPs presumably because of bAP attenuation at these locations (Golding *et al.*, 2001).

(4.3.7) Integration zones beyond the somatic compartment

Calcium spikes are known to occur in CA1 neurons (Takahashi & Magee, 2009) and in L5 pyramidal neurons there appears to be a calcium "hotspot" representing a distal integration zone (Larkum *et al.*, 2009). Activation of multiple distal, tuft dendrites in L5 pyramidal neurons leads to a calcium spike (Larkum *et al.*, 2009). If these synapses are beyond the effective range of bAPs, the main bifurcation zone (AppFig3A) of pyramidal neurons may be the critical integration zone for distal synapses rather than the soma. VGCCs seem to support calcium spike initiation (Larkum *et al.*, 2009; Almog & Korngreen, 2016) while making no contribution to calcium events in the distal tuft dendrites (Larkum *et al.*, 2009). My findings indicate that SSCTs at distal synapses are not substantially supported by CaV2.3 or CaV3 channels – the VGCC subtypes contributing to detectable calcium influx in spines (Fig10C,D; Fig11). 10µM nimodipine decreased SSCT amplitude at distal sites, suggesting CaV1 subtypes are activated by strong synaptic activity in these locations. However, CaV2.3 and CaV3 channels are implicated in driving measurable calcium influx into spines, while CaV1-mediated calcium influx is weak (Yasuda *et al.*, 2003; Bloodgood & Sabatini, 2007) and maybe tightly coupled to downstream signalling molecules such as calmodulin (Dolmetsch *et al.*, 2001). Tight coupling between channels and signalling molecules may limit contribution to total calcium ion concentration by CaV1 channels (Yasuda et al, 2003), unless experimental conditions – such as 0 magnesium – increase spine depolarization and thus activation of HVA channels, including CaV1 subtypes. The absence of CaV2.3 and CaV3 at distal dendrites may reflect a pattern of VGCC expression – an intrinsic property of the pyramidal neuron class (and possibly others) needed to support distance-dependent learning rules across the dendritic tree.

Input cooperativity is a mechanism for LTP induction across many synapses and perhaps the only mechanism for more distal synapses (Kim *et al.*, 2015). Due to the cable filtering properties and leak currents that exist in dendrites (Judkewitz *et al.*, 2006), input cooperativity is likely to be more efficient between single synapses if inputs coding for related signals cluster throughout the dendritic tree.

(4.3.8) Input cooperativity in single dendrites: an under-estimated role in LTP induction?

Input cooperativity is an essential property of functional synaptic connectivity, which supports induction of LTP in multiple experimental paradigms. Input cooperativity can mean cooperativity between inputs on the same branch (Golding *et al.*, 2002; Losonczy & Magee, 2006; Losonczy *et al.*, 2008; Kim *et al.*, 2015; Weber *et al.*, 2016) or between different dendritic compartments (Larkum *et al.*, 1999; Dudman *et al.*, 2007; Takahashi & Magee, 2009). Given that potentials arising from single inputs are detected only as very small voltage fluctuations in the cell body – particularly from distal synapses (Williams & Stuart, 2002) – it seems unlikely that integration of single inputs across dendritic compartments would be an effective mechanism underlying single-cell information processing. Intuitively, a more effective mechanism would be for neurons to integrate synaptic signals before further integration takes place beyond the dendrite in a clustered integration model – similar to that described by (Govindarajan *et al.*, 2006).

Despite the weight of evidence and opinion leaning towards a clustered integration model (Schiller *et al.*, 2000; Golding *et al.*, 2002; Losonczy & Magee, 2006; Govindarajan *et al.*, 2006; Losonczy *et al.*, 2008; Branco & Häusser, 2010; Weber *et al.*, 2016; Gökçe *et al.*, 2016), it has been suggested that linear, rather than supralinear, integration may be the essential mechanism underlying a neuron's capacity to process incoming inputs (Yuste, 2011). According to the distributed (Yuste, 2011) or dispersed (Govindarajan *et al.*, 2006) integration model, electrical compartmentalization of the spine exists to prevent shunting of synaptic potentials, which can integrate (as individual inputs) across the entire extent of the dendritic tree – not just a single dendrite. Yuste (2011) also suggests that spine neck resistances help to avoid supralinear integration – which implies supralinear measurements reported by others (Schiller *et al.*, 2000; Golding *et al.*, 2002; Larkum *et al.*, 2009) were artifacts of experimental manipulations.

A major advance in studying supralinear summation in dendrites came with the development of synchronous, multisite two photon glutamate uncaging (Judkewitz *et al.*, 2006). Supralinear summation in dendrites could be studied up to this point only with stimulation electrodes (e.g. Sjöström & Häusser, 2006) or uncaging with confocal laser scanning (Schiller *et al.*, 2000). A clear supralinear summation of EPSPs, with increasing current amplitude or laser power, could be

detected with these approaches, but the recruitment of multiple input sites had to be assumed and the exact number could not be controlled (Judkewitz *et al.*, 2006). Two-photon uncaging of glutamate closely mimics physiological glutamate release at synaptic sites, while synchronous multisite uncaging enables precise and flexible examination of supralinear summation of synaptic signals. In the first study to apply synchronous two photon glutamate uncaging, Losonczy & Magee (2006) delivered uncaging pulses at 0.1ms intervals across the length of a single apical oblique branch belonging to a CA1 pyramidal neuron. Their findings suggest that ~20 inputs must arrive within ~6ms to trigger supralinear summation. If the delay between the activation of inputs is too great (2-5ms) then summation proceeds linearly. Summation could be measured according to three variables: 1) EPSP amplitude, 2) EPSP rate of rise and 3) the amplitude of the dendritic calcium transient. 1µM TTX completely abolished supralinear summation, while blocking NMDARs limited the EPSP amplitude, but left the rate of rise unaffected. A cocktail of VGCC blockers (0.5µM SNX-482, 1µM conotoxin-MVIIC and 20µM nimodipine) linearized the summation of dendritic calcium transients and left other variables unaltered. From these results, Losonczy & Magee (2006) inferred that activation of VGSCs relieved magnesium block on activated NMDAR receptors and the conductance through NMDAR pores largely accounts for supralinear summation of EPSPs that can be measured with a patch pipette at the soma. Finally, one of their most interesting findings suggested that dendrites function as single computational units. Losonczy & Magee (2006) showed that both 20 spines spread across either ~20µm or ~60µm performed similarly well in reaching supralinear summation thresholds. This suggests temporally clustered inputs can be spread widely across the dendrite, but nevertheless sum to supralinear amplitudes.

Multiple groups of investigators using different techniques have found evidence for supralinear dendritic integration of synaptic potentials (Schiller *et al.*, 2000; Golding *et al.*, 2002; Losonczy & Magee, 2006; Losonczy *et al.*, 2008; Weber *et al.*, 2016). Moreover, two photon glutamate uncaging exposes the synapse to near-physiological patterns of stimulation making it difficult to imagine how supralinear potentials could be an experimental artifact.

(4.3.9) Functional synaptic clustering in vitro

If input cooperativity occurs along single dendrites, as findings discussed above suggest, then neighboring inputs should show a closer functional relationship than inputs located on distant branches. Evidence for such a type of functional synaptic clustering has been detected in cultured hippocampal slices (Harvey *et al.*, 2008; Murakoshi *et al.*, 2011; Kleindienst *et al.*, 2011; Takahashi *et al.*, 2012).

Kleindienst *et al.* (2011) imaged spontaneous synaptic calcium transients in CA3 neurons (DIV2-4) filled with a synthetic calcium indicator and held at -30mV command voltage to maximize detection of synaptic calcium transients mediated by NMDARs. They found pairs of synapses were more likely to have correlated transients when located less than 20µm from each other. If slices were incubated for 3-4 days in 1µM TTX or 50µM AP5, functional clustering was absent. Takahashi *et al.* (2012) also found evidence for functional synaptic clustering in cultured CA3 neurons arising from spontaneous activity amongst neighboring (<10µm) spines. Although this was after a longer incubation period (DIV12-19) and, in contrast to Kleindienst *et al.* (2011), they did not detect functional clustering in more immature networks (DIV3-4). Takahashi and colleagues reasoned that apparent functional clustering in cultured brain slices could be accounted for by several possible factors: 1) convergent afferents from a population of spontaneously spiking presynaptic neurons, 2) inputs arising from a single presynaptic neuron, 3) spillover of glutamate, 4) segregation of single inputs by inhibition, or 5) local depolarization inducing calcium transients in neighboring spines. Possibilities 2, 3 and 5 seemed unlikely after the authors induced synchronized network activity (triggering at least 400pA compound EPSCs in patched neurons) and found no evidence for functional clustering. Possibility 2 could be further ruled out by a set of experiments showing that more than 90% of contacts between two biocytin labelled neurons were single putative synapses within a cluster (from a total of 12 cell pairs). The fourth possibility seemed highly unlikely because spine activation remained clustered even in the presence of 1mM picrotoxin. Thus, as other possibilities seemed unlikely, Takahashi et al suggested that clustering of spontaneous activity arises due to converging afferents from multiple, spontaneously spiking presynaptic partners.

These in vitro studies have provided compelling evidence that synapses are organized along single dendritic branches in an optimal arrangement for supporting input cooperativity between single synapses on the same branch. In vivo, there are conflicting reports, but these inconsistent conclusions may arise due to different preconceptions of the organizational rules determining functional synaptic clustering in the intact brain.

(4.3.10) Functional synaptic clustering in vivo

In addition to their slice studies, Takahashi et al measured spontaneous synaptic calcium transients from layer 2/3 pyramidal neurons of the somatosensory cortex in anaesthetized mice. Consistent with their slice culture experiments, these authors again found that spines situated within 10µm of each other showed clustered activation. Other efforts to map functional synaptic clusters in vivo have not found evidence for functional synaptic clustering (Jia *et al.*, 2010; Chen *et al.*, 2011). Hubel and Wiesel's experiments in cat visual cortex showed that neurons of the primary

visual cortex (V1) preferentially spike in response to drifting rectangular light spots of a specific orientation presented within the cell's receptive field (Hubel & Wiesel, 1959). Jia *et al.*, (2010) measured the orientation selectivity of single spines in patched layer 2/3 neurons of the mouse V1 cortex. They found that spines with similar orientation preferences did not cluster. A study using similar methods (Chen *et al.*, 2011) testing spines in the auditory cortex A1 for functional clustering also found an apparent absence of clusters based on sound frequency preferences. However, a more recent study has found evidence for functional synaptic clustering in layer 2/3 mouse V1 neurons based on receptive field characteristics (Iacaruso *et al.*, 2017). This study showed that neighboring spines were more likely to have correlated receptive field maps than spines further apart. Consistent with Jia *et al.* (2010), Iacaruso and colleagues found no evidence for clustering based on orientation selectivity. Verifying what, if any, functional clustering exists in the other cortices may prove more challenging. The A1 cortex is more multimodal than V1 and may even be more equivalent to higher cortical areas in the visual system (such as the inferior temporal cortex) rather than V1 (King & Nelken, 2009). Even if sound frequency preferences contribute to organizational principles underlying functional synaptic clustering, they may overlap with others.

(4.3.11) Secrets of LTP induction and dissociated cultures

As has been previously noted (Schiller *et al.*, 2000; Golding *et al.*, 2002; Williams *et al.*, 2007; Kim *et al.*, 2015), carefully timed somatic depolarization is not always sufficient or necessary to induce LTP. Robust LTP can be induced in hippocampal brain slices and this is aided by bundles of axons projecting to distal (within the SLM) or proximal (within the SR) compartments, which can be selectively stimulated depending on experimental requirements. LTP can be induced in both distal and proximal compartments of hippocampal CA1 neurons with input cooperativity alone (Golding *et al.*, 2002; Kim *et al.*, 2015; Weber *et al.*, 2016). Back propagating spikes, on the other hand, can at least reach proximal regions of the dendritic tree (Koester & Sakmann, 1998; Golding *et al.*, 2001; Losonczy & Magee, 2006), but in distal regions of CA1 pyramidal neurons – the tuft dendrites – bAPs are not necessary for LTP induction (Golding *et al.*, 2002; Kim *et al.*, 2015; Weber *et al.*, 2016). In layer 5 pyramidal neurons, bAP involvement is more complex with LTP induction following anti-Hebbian rules (Sjöström & Häusser, 2006).

The role of bAPs in LTP induction needs to be re-evaluated. In cases where bAPs or voltage steps are applied to depolarize dendrites and relieve magnesium block of activated NMDARs, investigators may be using somatic depolarization where, under physiological conditions, input cooperativity within single dendrites is an equally if not more effective mechanism for removing magnesium from NMDAR pores. However, determining the exact role of bAPs in LTP induction is a difficult proposition for several important reasons. 1) It is likely to vary with cell type. I have

focused my discussion almost exclusively on synaptic transmission involving CA1 hippocampal neurons and layer 5 pyramidal neurons, but the extent to which bAPs are attenuated at the most distal input sites could vary considerably across the many morphological classes of CNS excitatory neurons. 2) bAPs might be involved only in specific forms of LTP. Ideally, variables used to readout late forms of LTP (L-LTP) expression should be monitored for more than two hours following application of an induction protocol. Studies testing involvement of bAPs in LTP rely on whole cell patch-clamp recordings, which can be maintained for little more than one hour the best cases. A backpropagating spike might participate differently in E-LTP and L-LTP (see section 1.2.2), but this cannot be tested when relying on whole cell patch-clamp recordings. I have found cells held with perforated-patch clamp to be stable for several hours. With optimized extracellular preparation and recording solutions, perforated patches should be stable for the required lengths of time for measuring L-LTP.

I believe that the main difficulty with routinely inducing stable LTP in high-density dissociated cultures lies not with technical challenges such as finding connected presynaptic partners or avoiding cytosolic washout. Input cooperativity between functionally clustered synapses on single dendrites is absent when paired stimulation is applied to two synaptically connected dissociated neurons prepared at the cell densities I used. This input cooperativity can be rescued in low density cultures because, in most instances, any given neuron will receive inputs from the same neuron on a single dendritic branch when there are very low numbers of possible presynaptic partners (AppFig3B). Thus, the chance of input cooperativity occurring by stimulating only a single presynaptic partner is substantially increased under low density conditions. Without adequate input cooperativity at synaptic clusters on single branches, inducing LTP depends on input location being sufficiently proximal to the recording location such that the synapse will be sensitive to current injections or voltage steps delivered through the pipette. In high-density dissociated cultures, inputs are most probably distributed across the dendritic tree at both proximal and distal locations (AppFig3C). Any potentiation at proximal synapses will be read out along with non-potentiating distal synapses, which would reduce detection of stable LTP.

(4.4) Unresolved issues and caveats

(4.4.1) AARG analysis

Combining electrophysiology and imaging of synaptic calcium transients has been a critical development in understanding synaptic function. However, when activation of more than a small number of synapses is studied, analyses quickly become difficult to manage. AARG analysis enables automated analysis from a large number of synapses while preserving spatial information

that links each event to the input site it originated from. By selectively blocking VGCCs, I have applied AARG analysis to SSCTs in primary cell culture neurons. The results from this analysis are consistent with previous findings suggesting that channels supporting N-type currents (CaV2.2 channels) are not strongly expressed in dendrites of hippocampal neurons (Magee & Johnston, 1995*a*; Bloodgood & Sabatini, 2007). Expression of channels mediating L-type currents might be more uniform than originally thought, while CaV2.3 and CaV3 channels are expressed more heterogeneously. CaV2.3 and CaV3 channels mediate R-type and T-type currents, respectively. These channels are thought to contribute to spine calcium transients (Sabatini & Svoboda, 2000; Bloodgood & Sabatini, 2007), but AARG analysis indicates that this may not apply to more distal synapses. The sensitivity of SSCTs in secondary branches to both SNX and TTA-P2 reflects the presence of high CaV2.3 and CaV3 expression, which may support activation of non-linear summation events such as dendritic calcium spikes.

(4.4.2) AARG analysis: caveats in dissociated cultures

Despite the advantages AARG analysis brings to the study of synaptic function, several important caveats in the current experiments should be highlighted. I carried out these experiments exclusively in dissociated neuronal cultures at room temperature, which can never emulate the natural development of these neurons in the living brain. The preparation of dissociated cultures from embryonic-day-19 rats or newborn mouse pups requires mechanical extraction of growing neurons embedded within a developing network of other cells. Inevitably, each cell incurs some damage during this procedure and it is unclear how much mature neurons in culture, developing from a regenerated form, can truly represent mature neurons in vivo. Furthermore, temperature can influence the activation properties of several VGCC subtypes (Iftinca *et al.*, 2006; Peloquin *et al.*, 2008), which underlines the need to verify results acquired under non-physiological conditions by carrying out experiments in the intact brain or at least in acute brain slices with temperature controls set within physiological ranges.

I have also analysed SSCTs detected in ACSF lacking magnesium and containing 0.5-1µM TTX to block somatic spiking. The relief of magnesium blockade from NMDAR pores is a central theme in Hebbian plasticity, but it is unlikely that relief is regularly so complete and persistent that the NMDAR pore is as unimpeded as it is in zero magnesium ACSF. With no magnesium in the extracellular space, NMDAR activation may depolarize the spine to far greater extents than can be expected to occur under more physiologically relevant conditions. This could mean that NMDAR activation at a single spine is frequently insufficient to trigger activation of VGCCs and the current experiments overestimate VGCC contribution to spine calcium transients. Experimentally, this issue could be addressed by using zero magnesium to collect discrete compartmentalized SSCTs,

which enables AARG analysis to generate ROIs (in the same manner as for a subset of the rBDNF application experiments – Fig4). Measurement of spine calcium transients could then be applied to data acquired with 1mM magnesium and no TTX present in the bath solution. A small modification in the analysis procedure would be needed to exclude large calcium events triggered by spontaneous spiking, but this would be a minor undertaking.

A final caveat that needs to be considered is the dendrite classification scheme I followed. My experiments were restricted to the excitatory neuron population of dissociated hippocampal cultures. The majority of these neurons would have developed into pyramidal neurons, but a significant proportion can be expected to have been nascent granule neurons from the developing dentate gyrus region when the culture was prepared. Granule neurons lack main apical dendrites (Spruston & McBain, 2006) giving these neurons a very different morphology compared to pyramidal neurons. I classified dendrite branch points according to the number of branch points between a given branch and the soma. Primary branches are connected directly to the soma, while secondary branches have one branch point and more than secondary branch points have two. This classification scheme treats individual branches as single computational units. This may be a reasonable assumption because there are some results that are consistent with dendrites acting as single computational units. For example, single inputs can sum across long stretches of individual branches with the resulting calcium transient consistently initiating at points equidistant from the two most distant inputs (Losonczy & Magee, 2006). However, this classification scheme has assumed that branch point number is more critical than absolute distance to the soma. For example, on a pyramidal neuron, an apical oblique and distal tuft dendrite would both be classified as secondary dendrites. If distance-dependent learning rules for layer 5 pyramidal neurons (Sjöström & Häusser, 2006; Letzkus *et al.*, 2006) apply to hippocampal pyramidal neurons, then pooling of these dendrites might not be appropriate. Other than providing a more physiologically relevant setting, measuring spine calcium transients from hippocampal neurons in acute brain slices would also facilitate sampling from a more homogenous cell population. A classification scheme could then be applied, which is appropriate to the specific cell population being sampled.

(4.4.3) LTP: Unresolved issues

Attenuation of bAPs reduces the efficacy of somatic depolarization as a coincident event that drives LTP at distal synapses (Golding *et al.*, 2002; Sjöström & Häusser, 2006; Kim *et al.*, 2015). This lends support to the clustered integration model (Govindarajan *et al.*, 2006), where coincidence detection depends on the functional clustering of dendritic spines. However, once a dendritic spike has been triggered, it seems necessary that this potential will propagate to the soma or a local integration zone and sum with other dendritic spikes. This means we can expect

dendritic spikes to be attenuated by the same features of the dendritic tree that attenuate bAPs. Indeed, dendritic spikes reportedly propagate poorly through dendrites (Stuart *et al.*, 1997; Schiller *et al.*, 1997) with the extent of their attenuation being partly determined by dendritic potassium channels (Golding *et al.*, 1999; Losonczy *et al.*, 2008; Larkum *et al.*, 2009).

As with other voltage-gated ion channels, voltage-gated potassium channels have been organized according to sequence homology of their alpha 1, pore-forming subunits of which there are 12 (Vacher *et al.*, 2008; Jan & Jan, 2012). The first four members of this potassium channel family (Kv1-Kv4) are expressed across the dendrites, cell bodies and axons of CNS neurons (Vacher *et al.*, 2008). Kv4.2 channels were shown to be expressed in the soma and dendrites of hippocampal pyramidal neurons (Sheng *et al.*, 1992), which makes this channel type a possible mediator of A-type potassium currents detected along apical dendrites of CA1 neurons (Hoffman *et al.*, 1997). Channels mediating A-type currents in hippocampal pyramidal neurons are inactivated by relatively depolarized voltages (-50mV) and activated by hyperpolarized command potentials (-110mV) (Klee *et al.*, 1995). This property can be used to isolate and study the transient (A-type) current responses overlapping with sustained potassium conductance (Klee *et al.*, 1995; Hoffman *et al.*, 1997).

Hoffman *et al.* (1997) showed that A-type current amplitude increases with increasing distance from the soma along main apical dendrites of CA1 neurons. The isolated transient component was much more sensitive to 10mM 4-aminopyridine (4-AP) compared to the sustained current component (80% reduction versus 20%). Application of 8mM 4-AP prevented action potential attenuation (usually apparent at distal dendritic recording sites) in the main apical dendrite. More recent findings suggest that expression of auxiliary subunits is necessary for changing A-type current amplitudes with distance from the soma (Sun *et al.*, 2011) and others have speculated that NMDARs can modulate expression levels of channels mediating the A-type currents (Jan & Jan, 2012). If true, this could mean that some synapses can, to some extent, determine their own sensitivity to bAPs.

Cai *et al.* (2004) showed that A-type currents may not only attenuate somatic action potential backpropagation into dendrites, but also plateau potentials. These authors showed that 5mM 4-AP increases the duration of plateau potentials triggered by uncaging of glutamate. They showed a similar broadening of plateau potentials by transfecting neurons with a construct for a dominant negative variant of Kv4.2. These findings and those from other groups (e.g. Yang *et al.*, 2015), show that A-type potassium currents do not just limit bAP entry to dendritic regions, they also weaken summation of local dendritic potentials.

A-type currents may promote compartmentalization of the dendritic tree (Hoffman, 2013), but these currents must be overcome in order for local potentials to successfully propagate towards the soma. It is currently unclear what mechanisms, if any, are in place to facilitate feedforward propagation of dendritic spikes. If such mechanisms are found, it must then be determined, which model – the clustered or dispersed integration model – is best suited to accommodate these mechanisms.

References

Akopian AN, Sivilotti L & Wood JN (1996). A tetrodotoxin-resistant voltage-gated sodium channel expressed by sensory neurons. *Nature* **379,** 257–262.

Albert AP (2011). Gating mechanisms of canonical transient receptor potential channel proteins: role of phosphoinositols and diacylglycerol. *Adv Exp Med Biol* **704,** 391–411.

Almog M & Korngreen A (2016). Is realistic neuronal modeling realistic? *J Neurophysiol* **116,** 2180–2209.

Amaral MD & Pozzo-Miller L (2007). TRPC3 channels are necessary for brain-derived neurotrophic factor to activate a nonselective cationic current and to induce dendritic spine formation. *J Neurosci Off J Soc Neurosci* **27,** 5179–5189.

Amaral MD & Pozzo-Miller L (2012). Intracellular Ca2+ stores and Ca2+ influx are both required for BDNF to rapidly increase quantal vesicular transmitter release. *Neural Plast* **2012,** 203536.

Arancio O, Kandel ER & Hawkins RD (1995). Activity-dependent long-term enhancement of transmitter release by presynaptic 3',5'-cyclic GMP in cultured hippocampal neurons. *Nature* **376,** 74–80.

Assaife-Lopes N, Sousa VC, Pereira DB, Ribeiro JA & Sebastião AM (2014). Regulation of TrkB receptor translocation to lipid rafts by adenosine A(2A) receptors and its functional implications for BDNF-induced regulation of synaptic plasticity. *Purinergic Signal* **10,** 251–267.

Atlas D (2001). Functional and physical coupling of voltage-sensitive calcium channels with exocytotic proteins: ramifications for the secretion mechanism. *J Neurochem* **77,** 972–985.

Augustine GJ & Kasai H (2007). Bernard Katz, quantal transmitter release and the foundations of presynaptic physiology. *J Physiol* **578,** 623–625.

Banker GA (1980). Trophic interactions between astroglial cells and hippocampal neurons in culture. *Science* **209,** 809–810.

Barrionuevo G & Brown TH (1983). Associative long-term potentiation in hippocampal slices. *Proc Natl Acad Sci U S A* **80,** 7347–7351.

Bats C, Groc L & Choquet D (2007). The interaction between Stargazin and PSD-95 regulates AMPA receptor surface trafficking. *Neuron* **53,** 719–734.

Bean BP (2007). The action potential in mammalian central neurons. *Nat Rev Neurosci* **8,** 451–465.

Bekkers JM & Stevens CF (1990). Presynaptic mechanism for long-term potentiation in the hippocampus. *Nature* **346,** 724–729.

Berridge MJ & Irvine RF (1989). Inositol phosphates and cell signalling. *Nature* **341,** 197–205.

Bi GQ & Poo MM (1998). Synaptic modifications in cultured hippocampal neurons: dependence on spike timing, synaptic strength, and postsynaptic cell type. *J Neurosci Off J Soc Neurosci* **18,** 10464–10472.

Bliss T, Collingridge G & Morris R (2006). Synaptic Plasticity in the Hippocampus. In *The Hippocampus Book*, ed. Andersen P, Morris R, Amaral D, Bliss T & O'Keefe J, pp. 343–474. Oxford University Press. Available at: http://www.oxfordscholarship.com/view/10.1093/acprof:oso/9780195100273.001.0001/acprof-9780195100273-chapter-10 [Accessed September 11, 2016].

Bliss TV & Collingridge GL (1993). A synaptic model of memory: long-term potentiation in the hippocampus. *Nature* **361,** 31–39.

Bliss TV & Lomo T (1973). Long-lasting potentiation of synaptic transmission in the dentate area of the anaesthetized rabbit following stimulation of the perforant path. *J Physiol* **232,** 331–356.

Bliss TVP & Collingridge GL (2013). Expression of NMDA receptor-dependent LTP in the hippocampus: bridging the divide. *Mol Brain* **6,** 5.

Bloodgood BL & Sabatini BL (2005). Neuronal activity regulates diffusion across the neck of dendritic spines. *Science* **310,** 866–869.

Bloodgood BL & Sabatini BL (2007). Nonlinear regulation of unitary synaptic signals by CaV(2.3) voltage-sensitive calcium channels located in dendritic spines. *Neuron* **53,** 249–260.

Blum R, Kafitz KW & Konnerth A (2002). Neurotrophin-evoked depolarization requires the sodium channel Na(V)1.9. *Nature* **419,** 687–693.

Bock T & Stuart GJ (2016). Impact of calcium-activated potassium channels on NMDA spikes in cortical layer 5 pyramidal neurons. *J Neurophysiol* **115,** 1740–1748.

Bonnet SAD, Akad DS, Samaddar T, Liu Y, Huang X, Dong Y & Schlüter OM (2013). Synaptic State-Dependent Functional Interplay between Postsynaptic Density-95 and Synapse-Associated Protein 102. *J Neurosci* **33,** 13398–13409.

Bourne JN & Harris KM (2008). Balancing structure and function at hippocampal dendritic spines. *Annu Rev Neurosci* **31,** 47–67.

Branco T & Häusser M (2010). The single dendritic branch as a fundamental functional unit in the nervous system. *Curr Opin Neurobiol* **20,** 494–502.

Brewer GJ, Torricelli JR, Evege EK & Price PJ (1993). Optimized survival of hippocampal neurons in B27-supplemented neurobasal™, a new serum-free medium combination. *J Neurosci Res* **35,** 567–576.

Bywalez WG, Patirniche D, Rupprecht V, Stemmler M, Herz AVM, Pálfi D, Rózsa B & Egger V (2015). Local Postsynaptic Voltage-Gated Sodium Channel Activation in Dendritic Spines of Olfactory Bulb Granule Cells. *Neuron* **85,** 590–601.

Cai X, Liang CW, Muralidharan S, Muralidharan S, Kao JPY, Tang C-M & Thompson SM (2004). Unique roles of SK and Kv4.2 potassium channels in dendritic integration. *Neuron* **44,** 351–364.

Catterall WA (1999). Interactions of presynaptic Ca2+ channels and snare proteins in neurotransmitter release. *Ann N Y Acad Sci* **868,** 144–159.

Catterall WA (2011). Voltage-gated calcium channels. *Cold Spring Harb Perspect Biol* **3,** a003947.

Chamberland S & Tóth K (2016). Functionally heterogeneous synaptic vesicle pools support diverse synaptic signalling. *J Physiol* **594,** 825–835.

Chen HX, Otmakhov N & Lisman J (1999). Requirements for LTP induction by pairing in hippocampal CA1 pyramidal cells. *J Neurophysiol* **82,** 526–532.

Chen T-W, Wardill TJ, Sun Y, Pulver SR, Renninger SL, Baohan A, Schreiter ER, Kerr RA, Orger MB, Jayaraman V, Looger LL, Svoboda K & Kim DS (2013). Ultrasensitive fluorescent proteins for imaging neuronal activity. *Nature* **499,** 295–300.

Chen X, Leischner U, Rochefort NL, Nelken I & Konnerth A (2011). Functional mapping of single spines in cortical neurons in vivo. *Nature* **475,** 501–505.

Chen X, Ye H, Kuruvilla R, Ramanan N, Scangos KW, Zhang C, Johnson NM, England PM, Shokat KM & Ginty DD (2005). A chemical-genetic approach to studying neurotrophin signaling. *Neuron* **46,** 13–21.

Chen Y & Sabatini BL (2012). Signaling in dendritic spines and spine microdomains. *Curr Opin Neurobiol* **22,** 389–396.

Choe W, Messinger RB, Leach E, Eckle V-S, Obradovic A, Salajegheh R, Jevtovic-Todorovic V & Todorovic SM (2011). TTA-P2 is a potent and selective blocker of T-type calcium channels in rat sensory neurons and a novel antinociceptive agent. *Mol Pharmacol* **80,** 900–910.

Clark KA & Collingridge GL (1996). Evidence that heterosynaptic depolarization underlies associativity of long-term potentiation in rat hippocampus. *J Physiol* **490,** 455–462.

Clausen MV, Hilbers F & Poulsen H (2017). The Structure and Function of the Na,K-ATPase Isoforms in Health and Disease. *Front Physiol*; DOI: 10.3389/fphys.2017.00371.

Cohen LD, Zuchman R, Sorokina O, Müller A, Dieterich DC, Armstrong JD, Ziv T & Ziv NE (2013). Metabolic Turnover of Synaptic Proteins: Kinetics, Interdependencies and Implications for Synaptic Maintenance. *PLOS ONE* **8,** e63191.

Collingridge G (1987). Synaptic plasticity. The role of NMDA receptors in learning and memory. *Nature* **330,** 604–605.

Constals A, Penn AC, Compans B, Toulmé E, Phillipat A, Marais S, Retailleau N, Hafner A-S, Coussen F, Hosy E & Choquet D (2015). Glutamate-induced AMPA receptor desensitization increases their mobility and modulates short-term plasticity through unbinding from Stargazin. *Neuron* **85,** 787–803.

Coulson EJ, May LM, Osborne SL, Reid K, Underwood CK, Meunier FA, Bartlett PF & Sah P (2008). p75 neurotrophin receptor mediates neuronal cell death by activating GIRK channels through phosphatidylinositol 4,5-bisphosphate. *J Neurosci Off J Soc Neurosci* **28,** 315–324.

Cull-Candy S, Brickley S & Farrant M (2001). NMDA receptor subunits: diversity, development and disease. *Curr Opin Neurobiol* **11,** 327–335.

Dechant G & Barde Y-A (2002). The neurotrophin receptor p75(NTR): novel functions and implications for diseases of the nervous system. *Nat Neurosci* **5,** 1131–1136.

Del Castillo J & Katz B (1954). Quantal components of the end-plate potential. *J Physiol* **124,** 560–573.

Dingledine R, Borges K, Bowie D & Traynelis SF (1999). The Glutamate Receptor Ion Channels. *Pharmacol Rev* **51,** 7–62.

Dolmetsch RE, Pajvani U, Fife K, Spotts JM & Greenberg ME (2001). Signaling to the nucleus by an L-type calcium channel-calmodulin complex through the MAP kinase pathway. *Science* **294,** 333–339.

Dolphin AC (2016). Voltage-gated calcium channels and their auxiliary subunits: physiology and pathophysiology and pharmacology. *J Physiol* **594,** 5369–5390.

Dresbach T, Hempelmann A, Spilker C, tom Dieck S, Altrock WD, Zuschratter W, Garner CC & Gundelfinger ED (2003). Functional regions of the presynaptic cytomatrix protein bassoon: significance for synaptic targeting and cytomatrix anchoring. *Mol Cell Neurosci* **23,** 279–291.

Dudman JT, Tsay D & Siegelbaum SA (2007). A novel role for synaptic inputs at distal dendrites: instructive signals for hippocampal long-term plasticity. *Neuron* **56,** 866–879.

Dulubova I, Sugita S, Hill S, Hosaka M, Fernandez I, Südhof TC & Rizo J (1999). A conformational switch in syntaxin during exocytosis: role of munc18. *EMBO J* **18,** 4372–4382.

Ehlers MD (2000). Reinsertion or degradation of AMPA receptors determined by activity-dependent endocytic sorting. *Neuron* **28,** 511–525.

Ellefsen K, Settle B, Parker I & Smith I (2014). An algorithm for automated detection, localization and measurement of local calcium signals from camera-based imaging. *Cell Calcium* **56,** 147–156.

Emptage N, Bliss TV & Fine A (1999). Single synaptic events evoke NMDA receptor-mediated release of calcium from internal stores in hippocampal dendritic spines. *Neuron* **22,** 115–124.

Enoki R, Hu Y-L, Hamilton D & Fine A (2009). Expression of long-term plasticity at individual synapses in hippocampus is graded, bidirectional, and mainly presynaptic: optical quantal analysis. *Neuron* **62,** 242–253.

Fatt P & Katz B (1952). Spontaneous subthreshold activity at motor nerve endings. *J Physiol* **117,** 109–128.

Feldman DE (2012). The spike-timing dependence of plasticity. *Neuron* **75,** 556–571.

Fenno L, Yizhar O & Deisseroth K (2011). The development and application of optogenetics. *Annu Rev Neurosci* **34,** 389–412.

Figurov A, Pozzo-Miller LD, Olafsson P, Wang T & Lu B (1996). Regulation of synaptic responses to high-frequency stimulation and LTP by neurotrophins in the hippocampus. *Nature* **381,** 706–709.

Francis M, Qian X, Charbel C, Ledoux J, Parker JC & Taylor MS (2012). Automated region of interest analysis of dynamic Ca^{2}+ signals in image sequences. *Am J Physiol Cell Physiol* **303,** C236-243.

Frey U, Krug M, Reymann KG & Matthies H (1988). Anisomycin, an inhibitor of protein synthesis, blocks late phases of LTP phenomena in the hippocampal CA1 region in vitro. *Brain Res* **452,** 57–65.

Frey U & Morris RG (1997). Synaptic tagging and long-term potentiation. *Nature* **385,** 533–536.

Froemke RC, Poo M-M & Dan Y (2005). Spike-timing-dependent synaptic plasticity depends on dendritic location. *Nature* **434,** 221–225.

Giessel AJ & Sabatini BL (2010). M1 muscarinic receptors boost synaptic potentials and calcium influx in dendritic spines by inhibiting postsynaptic SK channels. *Neuron* **68,** 936–947.

Gökçe O, Bonhoeffer T & Scheuss V (2016). Clusters of synaptic inputs on dendrites of layer 5 pyramidal cells in mouse visual cortex. *eLife*; DOI: 10.7554/eLife.09222.

Golding NL, Jung HY, Mickus T & Spruston N (1999). Dendritic calcium spike initiation and repolarization are controlled by distinct potassium channel subtypes in CA1 pyramidal neurons. *J Neurosci Off J Soc Neurosci* **19,** 8789–8798.

Golding NL, Kath WL & Spruston N (2001). Dichotomy of action-potential backpropagation in CA1 pyramidal neuron dendrites. *J Neurophysiol* **86,** 2998–3010.

Golding NL & Spruston N (1998). Dendritic Sodium Spikes Are Variable Triggers of Axonal Action Potentials in Hippocampal CA1 Pyramidal Neurons. *Neuron* **21,** 1189–1200.

Golding NL, Staff NP & Spruston N (2002). Dendritic spikes as a mechanism for cooperative long-term potentiation. *Nature* **418,** 326–331.

Gomora JC, Enyeart JA & Enyeart JJ (1999). Mibefradil potently blocks ATP-activated K(+) channels in adrenal cells. *Mol Pharmacol* **56,** 1192–1197.

Goslin, Asmussen (second) & Banker (last) (1998). Rat hippocampal neurons in low density culture. In *Culturing Nerve Cells*, 2nd edn., pp. 339–370. The MIT Press.

Govindarajan A, Kelleher RJ & Tonegawa S (2006). A clustered plasticity model of long-term memory engrams. *Nat Rev Neurosci* **7,** 575–583.

Grienberger C & Konnerth A (2012). Imaging Calcium in Neurons. *Neuron* **73,** 862–885.

Grinvald A (2005). Imaging input and output dynamics of neocortical networks in vivo: exciting times ahead. *Proc Natl Acad Sci U S A* **102,** 14125–14126.

Grunditz Å, Holbro N, Tian L, Zuo Y & Oertner TG (2008). Spine Neck Plasticity Controls Postsynaptic Calcium Signals through Electrical Compartmentalization. *J Neurosci* **28,** 13457–13466.

Gustafsson B, Wigström H, Abraham WC & Huang YY (1987). Long-term potentiation in the hippocampus using depolarizing current pulses as the conditioning stimulus to single volley synaptic potentials. *J Neurosci Off J Soc Neurosci* **7,** 774–780.

Harnett MT, Makara JK, Spruston N, Kath WL & Magee JC (2012). Synaptic amplification by dendritic spines enhances input cooperativity. *Nature* **491,** 599–602.

Harvey CD, Yasuda R, Zhong H & Svoboda K (2008). The spread of Ras activity triggered by activation of a single dendritic spine. *Science* **321,** 136–140.

Hayashi Y, Shi SH, Esteban JA, Piccini A, Poncer JC & Malinow R (2000). Driving AMPA receptors into synapses by LTP and CaMKII: requirement for GluR1 and PDZ domain interaction. *Science* **287,** 2262–2267.

Hell JW, Westenbroek RE, Warner C, Ahlijanian MK, Prystay W, Gilbert MM, Snutch TP & Catterall WA (1993). Identification and differential subcellular localization of the neuronal class C and class D L-type calcium channel alpha 1 subunits. *J Cell Biol* **123,** 949–962.

Hille B (2001). *Ion Channels of Excitable Membranes, Third Edition*, 3rd Edition edition. Sinauer Associates, Sunderland, Mass.

Hochbaum DR et al. (2014). All-optical electrophysiology in mammalian neurons using engineered microbial rhodopsins. *Nat Methods* **11,** 825–833.

Hoffman DA (2013). K+ channel regulation of multicompartmental signal integration. *Neuron* **79,** 403–405.

Hoffman DA, Magee JC, Colbert CM & Johnston D (1997). K+ channel regulation of signal propagation in dendrites of hippocampal pyramidal neurons. *Nature* **387,** 869–875.

Holbro N, Grunditz A, Wiegert JS & Oertner TG (2010). AMPA receptors gate spine Ca(2+) transients and spike-timing-dependent potentiation. *Proc Natl Acad Sci U S A* **107,** 15975–15980.

Huang CL, Feng S & Hilgemann DW (1998). Direct activation of inward rectifier potassium channels by PIP2 and its stabilization by Gbetagamma. *Nature* **391,** 803–806.

Hubel DH & Wiesel TN (1959). Receptive fields of single neurones in the cat's striate cortex. *J Physiol* **148,** 574–591.

Huettner JE & Baughman RW (1986). Primary culture of identified neurons from the visual cortex of postnatal rats. *J Neurosci Off J Soc Neurosci* **6,** 3044–3060.

Iacaruso MF, Gasler IT & Hofer SB (2017). Synaptic organization of visual space in primary visual cortex. *Nature* **547,** 449–452.

Iftinca M, McKay BE, Snutch TP, McRory JE, Turner RW & Zamponi GW (2006). Temperature dependence of T-type calcium channel gating. *Neuroscience* **142,** 1031–1042.

Impey S, Mark M, Villacres EC, Poser S, Chavkin C & Storm DR (1996). Induction of CRE-mediated gene expression by stimuli that generate long-lasting LTP in area CA1 of the hippocampus. *Neuron* **16,** 973–982.

Ireland DR, Guevremont D, Williams JM & Abraham WC (2004). Metabotropic glutamate receptor-mediated depression of the slow afterhyperpolarization is gated by tyrosine phosphatases in hippocampal CA1 pyramidal neurons. *J Neurophysiol* **92,** 2811–2819.

Isaac JT, Nicoll RA & Malenka RC (1995). Evidence for silent synapses: implications for the expression of LTP. *Neuron* **15,** 427–434.

Isaac JTR, Ashby MC & McBain CJ (2007). The role of the GluR2 subunit in AMPA receptor function and synaptic plasticity. *Neuron* **54,** 859–871.

Jaafari N, De Waard M & Canepari M (2014). Imaging Fast Calcium Currents beyond the Limitations of Electrode Techniques. *Biophys J* **107,** 1280–1288.

Jahr CE & Stevens CF (1990). Voltage dependence of NMDA-activated macroscopic conductances predicted by single-channel kinetics. *J Neurosci Off J Soc Neurosci* **10,** 3178–3182.

Jan LY & Jan YN (2012). Voltage-gated potassium channels and the diversity of electrical signalling. *J Physiol* **590,** 2591–2599.

Jia H, Rochefort NL, Chen X & Konnerth A (2010). Dendritic organization of sensory input to cortical neurons in vivo. *Nature* **464,** 1307–1312.

Jiang M & Chen G (2006). High Ca2+-phosphate transfection efficiency in low-density neuronal cultures. *Nat Protoc* **1,** 695–700.

Jiménez C, Bourinet E, Leuranguer V, Richard S, Snutch TP & Nargeot J (2000). Determinants of voltage-dependent inactivation affect Mibefradil block of calcium channels. *Neuropharmacology* **39,** 1–10.

Judkewitz B, Roth A & Häusser M (2006). Dendritic Enlightenment: Using Patterned Two-Photon Uncaging to Reveal the Secrets of the Brain's Smallest Dendrites. *Neuron* **50,** 180–183.

Junek S, Chen T-W, Alevra M & Schild D (2009). Activity correlation imaging: visualizing function and structure of neuronal populations. *Biophys J* **96,** 3801–3809.

Kampa BM, Clements J, Jonas P & Stuart GJ (2004). Kinetics of Mg2+ unblock of NMDA receptors: implications for spike-timing dependent synaptic plasticity. *J Physiol* **556,** 337–345.

Kampa BM, Letzkus JJ & Stuart GJ (2006). Requirement of dendritic calcium spikes for induction of spike-timing-dependent synaptic plasticity. *J Physiol* **574,** 283–290.

Katz Y, Menon V, Nicholson DA, Geinisman Y, Kath WL & Spruston N (2009). Synapse distribution suggests a two-stage model of dendritic integration in CA1 pyramidal neurons. *Neuron* **63,** 171–177.

Kerchner GA & Nicoll RA (2008). Silent synapses and the emergence of a postsynaptic mechanism for LTP. *Nat Rev Neurosci* **9,** 813–825.

Kim E & Sheng M (2004). PDZ domain proteins of synapses. *Nat Rev Neurosci* **5,** 771–781.

Kim Y, Hsu C-L, Cembrowski MS, Mensh BD & Spruston N (2015). Dendritic sodium spikes are required for long-term potentiation at distal synapses on hippocampal pyramidal neurons. *eLife* **4,** e06414.

King AJ & Nelken I (2009). Unraveling the principles of auditory cortical processing: can we learn from the visual system? *Nat Neurosci* **12,** 698–701.

Klee R, Ficker E & Heinemann U (1995). Comparison of voltage-dependent potassium currents in rat pyramidal neurons acutely isolated from hippocampal regions CA1 and CA3. *J Neurophysiol* **74,** 1982–1995.

Kleindienst T, Winnubst J, Roth-Alpermann C, Bonhoeffer T & Lohmann C (2011). Activity-dependent clustering of functional synaptic inputs on developing hippocampal dendrites. *Neuron* **72,** 1012–1024.

Kniss DA & Burry RW (1988). Serum and fibroblast growth factor stimulate quiescent astrocytes to re-enter the cell cycle. *Brain Res* **439,** 281–288.

Kobrinsky E, Mirshahi T, Zhang H, Jin T & Logothetis DE (2000). Receptor-mediated hydrolysis of plasma membrane messenger PIP2 leads to K+-current desensitization. *Nat Cell Biol* **2,** 507–514.

Koester HJ & Sakmann B (1998). Calcium dynamics in single spines during coincident pre- and postsynaptic activity depend on relative timing of back-propagating action potentials and subthreshold excitatory postsynaptic potentials. *Proc Natl Acad Sci U S A* **95,** 9596–9601.

Korte M, Griesbeck O, Gravel C, Carroll P, Staiger V, Thoenen H & Bonhoeffer T (1996). Virus-mediated gene transfer into hippocampal CA1 region restores long-term potentiation in brain-derived neurotrophic factor mutant mice. *Proc Natl Acad Sci U S A* **93,** 12547–12552.

Kovalchuk Y, Eilers J, Lisman J & Konnerth A (2000). NMDA receptor-mediated subthreshold Ca(2+) signals in spines of hippocampal neurons. *J Neurosci Off J Soc Neurosci* **20,** 1791–1799.

Kullmann DM (1994). Amplitude fluctuations of dual-component EPSCs in hippocampal pyramidal cells: implications for long-term potentiation. *Neuron* **12,** 1111–1120.

Kullmann DM & Nicoll RA (1992). Long-term potentiation is associated with increases in quantal content and quantal amplitude. *Nature* **357,** 240–244.

Lambert RC, Bessaïh T, Crunelli V & Leresche N (2014). The many faces of T-type calcium channels. *Pflüg Arch - Eur J Physiol* **466,** 415–423.

Larkum ME, Nevian T, Sandler M, Polsky A & Schiller J (2009). Synaptic integration in tuft dendrites of layer 5 pyramidal neurons: a new unifying principle. *Science* **325,** 756–760.

Larkum ME, Zhu JJ & Sakmann B (1999). A new cellular mechanism for coupling inputs arriving at different cortical layers. *Nature* **398,** 338–341.

Larson J & Munkácsy E (2015). Theta-burst LTP. *Brain Res* **1621,** 38–50.

Lee FS & Chao MV (2001). Activation of Trk neurotrophin receptors in the absence of neurotrophins. *Proc Natl Acad Sci U S A* **98,** 3555–3560.

Lee HK, Barbarosie M, Kameyama K, Bear MF & Huganir RL (2000). Regulation of distinct AMPA receptor phosphorylation sites during bidirectional synaptic plasticity. *Nature* **405,** 955–959.

Lee H-K, Takamiya K, He K, Song L & Huganir RL (2010). Specific Roles of AMPA Receptor Subunit GluR1 (GluA1) Phosphorylation Sites in Regulating Synaptic Plasticity in the CA1 Region of Hippocampus. *J Neurophysiol* **103,** 479–489.

Lee JH, Gomora JC, Cribbs LL & Perez-Reyes E (1999). Nickel block of three cloned T-type calcium channels: low concentrations selectively block alpha1H. *Biophys J* **77,** 3034–3042.

Letzkus JJ, Kampa BM & Stuart GJ (2006). Learning rules for spike timing-dependent plasticity depend on dendritic synapse location. *J Neurosci Off J Soc Neurosci* **26,** 10420–10429.

Li HS, Xu XZ & Montell C (1999). Activation of a TRPC3-dependent cation current through the neurotrophin BDNF. *Neuron* **24,** 261–273.

Li Y, Calfa G, Inoue T, Amaral MD & Pozzo-Miller L (2010). Activity-dependent release of endogenous BDNF from mossy fibers evokes a TRPC3 current and Ca2+ elevations in CA3 pyramidal neurons. *J Neurophysiol* **103,** 2846–2856.

Liao D, Hessler NA & Malinow R (1995). Activation of postsynaptically silent synapses during pairing-induced LTP in CA1 region of hippocampal slice. *Nature* **375,** 400–404.

Lohmann C & Kessels HW (2014). The developmental stages of synaptic plasticity. *J Physiol* **592,** 13–31.

Lohof AM, Ip NY & Poo MM (1993). Potentiation of developing neuromuscular synapses by the neurotrophins NT-3 and BDNF. *Nature* **363,** 350–353.

Losonczy A & Magee JC (2006). Integrative Properties of Radial Oblique Dendrites in Hippocampal CA1 Pyramidal Neurons. *Neuron* **50,** 291–307.

Losonczy A, Makara JK & Magee JC (2008). Compartmentalized dendritic plasticity and input feature storage in neurons. *Nature* **452,** 436–441.

Lu B (2003). BDNF and Activity-Dependent Synaptic Modulation. *Learn Mem* **10,** 86–98.

Lu W, Man H, Ju W, Trimble WS, MacDonald JF & Wang YT (2001). Activation of synaptic NMDA receptors induces membrane insertion of new AMPA receptors and LTP in cultured hippocampal neurons. *Neuron* **29,** 243–254.

Lu Y, Christian K & Lu B (2008). BDNF: A Key Regulator for Protein-synthesis Dependent LTP and Long-term Memory? *Neurobiol Learn Mem* **89,** 312–323.

Lu Y, Ji Y, Ganesan S, Schloesser R, Martinowich K, Sun M, Mei F, Chao MV & Lu B (2011). TrkB as a Potential Synaptic and Behavioral Tag. *J Neurosci* **31,** 11762–11771.

Lüscher C, Jan LY, Stoffel M, Malenka RC & Nicoll RA (1997). G protein-coupled inwardly rectifying K+ channels (GIRKs) mediate postsynaptic but not presynaptic transmitter actions in hippocampal neurons. *Neuron* **19,** 687–695.

Magby JP, Bi C, Chen Z-Y, Lee FS & Plummer MR (2006). Single-cell characterization of retrograde signaling by brain-derived neurotrophic factor. *J Neurosci Off J Soc Neurosci* **26,** 13531–13536.

Magee JC (2000). Dendritic integration of excitatory synaptic input. *Nat Rev Neurosci* **1,** 181–190.

Magee JC & Carruth M (1999). Dendritic voltage-gated ion channels regulate the action potential firing mode of hippocampal CA1 pyramidal neurons. *J Neurophysiol* **82,** 1895–1901.

Magee JC & Cook EP (2000). Somatic EPSP amplitude is independent of synapse location in hippocampal pyramidal neurons. *Nat Neurosci* **3,** 895–903.

Magee JC & Johnston D (1995*a*). Characterization of single voltage-gated Na+ and Ca2+ channels in apical dendrites of rat CA1 pyramidal neurons. *J Physiol* **487,** 67–90.

Magee JC & Johnston D (1995*b*). Synaptic activation of voltage-gated channels in the dendrites of hippocampal pyramidal neurons. *Science* **268,** 301–304.

Magee JC & Johnston D (1997). A Synaptically Controlled, Associative Signal for Hebbian Plasticity in Hippocampal Neurons. *Science* **275,** 209–213.

Major G, Larkum ME & Schiller J (2013). Active properties of neocortical pyramidal neuron dendrites. *Annu Rev Neurosci* **36,** 1–24.

Malenka RC & Bear MF (2004). LTP and LTD: An Embarrassment of Riches. *Neuron* **44,** 5–21.

Malenka RC, Kauer JA, Perkel DJ, Mauk MD, Kelly PT, Nicoll RA & Waxham MN (1989). An essential role for postsynaptic calmodulin and protein kinase activity in long-term potentiation. *Nature* **340,** 554–557.

Malinow R (1991). Transmission between pairs of hippocampal slice neurons: quantal levels, oscillations, and LTP. *Science* **252,** 722–724.

Malinow R, Madison DV & Tsien RW (1988). Persistent protein kinase activity underlying long-term potentiation. *Nature* **335,** 820–824.

Malinow R & Tsien RW (1990). Presynaptic enhancement shown by whole-cell recordings of long-term potentiation in hippocampal slices. *Nature* **346,** 177–180.

Manabe T, Wyllie DJ, Perkel DJ & Nicoll RA (1993). Modulation of synaptic transmission and long-term potentiation: effects on paired pulse facilitation and EPSC variance in the CA1 region of the hippocampus. *J Neurophysiol* **70,** 1451–1459.

Markram H, Lübke J, Frotscher M & Sakmann B (1997). Regulation of synaptic efficacy by coincidence of postsynaptic APs and EPSPs. *Science* **275,** 213–215.

Marty A & Neher E (1995). Tight-Seal Whole-Cell Recording. In *Single-Channel Recording*, ed. Sakmann B & Neher E, pp. 31–52. Springer US, Boston, MA. Available at: http://link.springer.com/10.1007/978-1-4419-1229-9_2 [Accessed November 26, 2017].

McDonald TF, Pelzer S, Trautwein W & Pelzer DJ (1994). Regulation and modulation of calcium channels in cardiac, skeletal, and smooth muscle cells. *Physiol Rev* **74,** 365–507.

Menon V, Musial TF, Liu A, Katz Y, Kath WL, Spruston N & Nicholson DA (2013). Balanced Synaptic Impact via Distance-Dependent Synapse Distribution and Complementary Expression of AMPARs and NMDARs in Hippocampal Dendrites. *Neuron*; DOI: 10.1016/j.neuron.2013.09.027.

Metz AE, Jarsky T, Martina M & Spruston N (2005). R-Type Calcium Channels Contribute to Afterdepolarization and Bursting in Hippocampal CA1 Pyramidal Neurons. *J Neurosci* **25,** 5763–5773.

Michler-Stuke A, Wolff JR & Bottenstein JE (1984). Factors influencing astrocyte growth and development in defined media. *Int J Dev Neurosci Off J Int Soc Dev Neurosci* **2,** 575–584.

Minichiello L, Calella AM, Medina DL, Bonhoeffer T, Klein R & Korte M (2002). Mechanism of TrkB-mediated hippocampal long-term potentiation. *Neuron* **36,** 121–137.

Miyawaki A, Llopis J, Heim R, McCaffery JM, Adams JA, Ikura M & Tsien RY (1997). Fluorescent indicators for Ca2+ based on green fluorescent proteins and calmodulin. *Nature* **388,** 882–887.

Molnár E (2011). Long-term potentiation in cultured hippocampal neurons. *Semin Cell Dev Biol* **22,** 506–513.

Morgan SL & Teyler TJ (2001). Electrical stimuli patterned after the theta-rhythm induce multiple forms of LTP. *J Neurophysiol* **86,** 1289–1296.

Mukamel EA, Nimmerjahn A & Schnitzer MJ (2009). Automated analysis of cellular signals from large-scale calcium imaging data. *Neuron* **63,** 747–760.

Murakoshi H, Wang H & Yasuda R (2011). Local, persistent activation of Rho GTPases during plasticity of single dendritic spines. *Nature* **472,** 100–104.

Nguyen PV, Abel T & Kandel ER (1994). Requirement of a critical period of transcription for induction of a late phase of LTP. *Science* **265,** 1104–1107.

Nishiyama J & Yasuda R (2015). Biochemical Computation for Spine Structural Plasticity. *Neuron* **87,** 63–75.

O'Brien RJ, Kamboj S, Ehlers MD, Rosen KR, Fischbach GD & Huganir RL (1998). Activity-dependent modulation of synaptic AMPA receptor accumulation. *Neuron* **21,** 1067–1078.

Pakkenberg B, Pelvig D, Marner L, Bundgaard MJ, Gundersen HJG, Nyengaard JR & Regeur L (2003). Aging and the human neocortex. *Exp Gerontol* **38,** 95–99.

Park J-Y, Remy S, Varela J, Cooper DC, Chung S, Kang H-W, Lee J-H & Spruston N (2010). A Post-Burst Afterdepolarization Is Mediated by Group I Metabotropic Glutamate Receptor-Dependent Upregulation of Cav2.3 R-Type Calcium Channels in CA1 Pyramidal Neurons. *PLOS Biol* **8,** e1000534.

Park M, Penick EC, Edwards JG, Kauer JA & Ehlers MD (2004). Recycling endosomes supply AMPA receptors for LTP. *Science* **305,** 1972–1975.

Patterson SL, Abel T, Deuel TA, Martin KC, Rose JC & Kandel ER (1996). Recombinant BDNF rescues deficits in basal synaptic transmission and hippocampal LTP in BDNF knockout mice. *Neuron* **16,** 1137–1145.

Peloquin JB, Doering CJ, Rehak R & McRory JE (2008). Temperature dependence of Cav1.4 calcium channel gating. *Neuroscience* **151,** 1066–1083.

Perez-Reyes E (2003). Molecular physiology of low-voltage-activated t-type calcium channels. *Physiol Rev* **83,** 117–161.

Perkel DJ, Petrozzino JJ, Nicoll RA & Connor JA (1993). The role of Ca2+ entry via synaptically activated NMDA receptors in the induction of long-term potentiation. *Neuron* **11,** 817–823.

Petrini EM, Lu J, Cognet L, Lounis B, Ehlers MD & Choquet D (2009). Endocytic Trafficking and Recycling Maintain a Pool of Mobile Surface AMPA Receptors Required for Synaptic Potentiation. *Neuron* **63,** 92–105.

Puehringer D, Orel N, Lüningschrör P, Subramanian N, Herrmann T, Chao MV & Sendtner M (2013). EGF transactivation of Trk receptors regulates the migration of newborn cortical neurons. *Nat Neurosci* **16,** 407–415.

Raastad M, Storm JF & Andersen P (1992). Putative Single Quantum and Single Fibre Excitatory Postsynaptic Currents Show Similar Amplitude Range and Variability in Rat Hippocampal Slices. *Eur J Neurosci* **4,** 113–117.

Rae J, Cooper K, Gates P & Watsky M (1991). Low access resistance perforated patch recordings using amphotericin B. *J Neurosci Methods* **37,** 15–26.

Rall W (1967). Distinguishing theoretical synaptic potentials computed for different soma-dendritic distributions of synaptic input. *J Neurophysiol* **30,** 1138–1168.

Randall A & Tsien RW (1995). Pharmacological dissection of multiple types of Ca2+ channel currents in rat cerebellar granule neurons. *J Neurosci Off J Soc Neurosci* **15,** 2995–3012.

Randall AD & Tsien RW (1997). Contrasting biophysical and pharmacological properties of T-type and R-type calcium channels. *Neuropharmacology* **36,** 879–893.

Rasband MN & Shrager P (2000). Ion channel sequestration in central nervous system axons. *J Physiol* **525 Pt 1,** 63–73.

Rasnik I, French T, Jacobson K & Berland K (2013). Electronic cameras for low-light microscopy. *Methods Cell Biol* **114,** 211–241.

Raymond CR & Redman SJ (2002). Different calcium sources are narrowly tuned to the induction of different forms of LTP. *J Neurophysiol* **88,** 249–255.

Redondo RL & Morris RGM (2011). Making memories last: the synaptic tagging and capture hypothesis. *Nat Rev Neurosci* **12,** 17–30.

Reese AL & Kavalali ET (2015). Spontaneous neurotransmission signals through store-driven Ca2+ transients to maintain synaptic homeostasis. *eLife* **4,** e09262.

Remondes M & Schuman EM (2003). Molecular mechanisms contributing to long-lasting synaptic plasticity at the temporoammonic-CA1 synapse. *Learn Mem Cold Spring Harb N* **10,** 247–252.

Rizzoli SO (2014). Synaptic vesicle recycling: steps and principles. *EMBO J* **33,** 788–822.

Russell JT (2011). Imaging calcium signals in vivo: a powerful tool in physiology and pharmacology. *Br J Pharmacol* **163,** 1605–1625.

Sabatini BL, Oertner TG & Svoboda K (2002). The Life Cycle of Ca2+ Ions in Dendritic Spines. *Neuron* **33,** 439–452.

Sabatini BL & Svoboda K (2000). Analysis of calcium channels in single spines using optical fluctuation analysis. *Nature* **408,** 589–593.

Sadja R, Alagem N & Reuveny E (2002). Graded contribution of the Gβγ binding domains to GIRK channel activation. *Proc Natl Acad Sci* **99,** 10783–10788.

Sakmann B & Neher E eds. (1995). *Single-Channel Recording*. Springer US, Boston, MA. Available at: http://link.springer.com/10.1007/978-1-4419-1229-9 [Accessed July 20, 2016].

Schiller J, Major G, Koester HJ & Schiller Y (2000). NMDA spikes in basal dendrites of cortical pyramidal neurons. *Nature* **404,** 285–289.

Schiller J, Schiller Y & Clapham DE (1998). NMDA receptors amplify calcium influx into dendritic spines during associative pre- and postsynaptic activation. *Nat Neurosci* **1,** 114–118.

Schiller J, Schiller Y, Stuart G & Sakmann B (1997). Calcium action potentials restricted to distal apical dendrites of rat neocortical pyramidal neurons. *J Physiol* **505 (Pt 3),** 605–616.

Segev I & London M (2000). Untangling dendrites with quantitative models. *Science* **290,** 744–750.

Sharp AA, O'Neil MB, Abbott LF & Marder E (1993). Dynamic clamp: computer-generated conductances in real neurons. *J Neurophysiol* **69,** 992–995.

Sheng M, Tsaur ML, Jan YN & Jan LY (1992). Subcellular segregation of two A-type K+ channel proteins in rat central neurons. *Neuron* **9,** 271–284.

Shipe WD et al. (2008). Design, synthesis, and evaluation of a novel 4-aminomethyl-4-fluoropiperidine as a T-type Ca2+ channel antagonist. *J Med Chem* **51,** 3692–3695.

Shipman SL, Herring BE, Suh YH, Roche KW & Nicoll RA (2013). Distance-dependent scaling of AMPARs is cell-autonomous and GluA2 dependent. *J Neurosci Off J Soc Neurosci* **33,** 13312–13319.

Silver RA (2010). Neuronal arithmetic. *Nat Rev Neurosci* **11,** 474–489.

Simms BA & Zamponi GW (2014). Neuronal Voltage-Gated Calcium Channels: Structure, Function, and Dysfunction. *Neuron* **82,** 24–45.

Sjöström PJ & Häusser M (2006). A Cooperative Switch Determines the Sign of Synaptic Plasticity in Distal Dendrites of Neocortical Pyramidal Neurons. *Neuron* **51,** 227–238.

Sjöström PJ, Rancz EA, Roth A & Häusser M (2008). Dendritic excitability and synaptic plasticity. *Physiol Rev* **88,** 769–840.

Sjöström PJ, Turrigiano GG & Nelson SB (2001). Rate, timing, and cooperativity jointly determine cortical synaptic plasticity. *Neuron* **32,** 1149–1164.

Smith MA, Ellis-Davies GCR & Magee JC (2003). Mechanism of the distance-dependent scaling of Schaffer collateral synapses in rat CA1 pyramidal neurons. *J Physiol* **548,** 245–258.

Snutch TP, Peloquin J, Mathews E & McRory JE (2013). *Molecular Properties of Voltage-Gated Calcium Channels*. Landes Bioscience. Available at: https://www.ncbi.nlm.nih.gov/books/NBK6181/ [Accessed November 1, 2017].

Spruston N (2000). Distant synapses raise their voices. *Nat Neurosci* **3,** 849–851.

Spruston N, Jaffe DB & Johnston D (1994). Dendritic attenuation of synaptic potentials and currents: the role of passive membrane properties. *Trends Neurosci* **17,** 161–166.

Spruston N & Johnston D (2008). Out of control in the dendrites. *Nat Neurosci* **11,** 733–734.

Spruston N & McBain C (2006). Structural and Functional Properties of Hippocampal Neurons. In *The Hippocampus Book*, ed. Andersen P, Morris R, Amaral D, Bliss T & O'Keefe J, pp. 133–202. Oxford University Press. Available at: http://www.oxfordscholarship.com/view/10.1093/acprof:oso/9780195100273.001.0001/acprof-9780195100273-chapter-5 [Accessed November 25, 2017].

Stevens CF & Wang Y (1994). Changes in reliability of synaptic function as a mechanism for plasticity. *Nature* **371,** 704–707.

Stuart G, Spruston N, Sakmann B & Häusser M (1997). Action potential initiation and backpropagation in neurons of the mammalian CNS. *Trends Neurosci* **20,** 125–131.

Stuart GJ & Häusser M (2001). Dendritic coincidence detection of EPSPs and action potentials. *Nat Neurosci* **4,** 63–71.

Stuart GJ & Sakmann B (1994). Active propagation of somatic action potentials into neocortical pyramidal cell dendrites. *Nature* **367,** 69–72.

Sturgill JF, Steiner P, Czervionke BL & Sabatini BL (2009). Distinct domains within PSD-95 mediate synaptic incorporation, stabilization, and activity-dependent trafficking. *J Neurosci Off J Soc Neurosci* **29,** 12845–12854.

Südhof TC (2013). Neurotransmitter Release: The Last Millisecond in the Life of a Synaptic Vesicle. *Neuron* **80,** 675–690.

Südhof TC & Rothman JE (2009). Membrane Fusion: Grappling with SNARE and SM Proteins. *Science* **323,** 474–477.

Sun W, Maffie JK, Lin L, Petralia RS, Rudy B & Hoffman DA (2011). DPP6 establishes the A-type K(+) current gradient critical for the regulation of dendritic excitability in CA1 hippocampal neurons. *Neuron* **71,** 1102–1115.

Svoboda K (1998). Shining light on spiny matters. *Nat Neurosci* **1,** 93–94.

Svoboda K, Tank DW & Denk W (1996). Direct Measurement of Coupling Between Dendritic Spines and Shafts. *Science* **272,** 716–719.

Tabone CJ & Ramaswami M (2012). Is NMDA receptor-coincidence detection required for learning and memory? *Neuron* **74,** 767–769.

Tai C, Kuzmiski JB & MacVicar BA (2006). Muscarinic Enhancement of R-Type Calcium Currents in Hippocampal CA1 Pyramidal Neurons. *J Neurosci* **26,** 6249–6258.

Takahashi H & Magee JC (2009). Pathway Interactions and Synaptic Plasticity in the Dendritic Tuft Regions of CA1 Pyramidal Neurons. *Neuron* **62,** 102–111.

Takahashi N, Kitamura K, Matsuo N, Mayford M, Kano M, Matsuki N & Ikegaya Y (2012). Locally synchronized synaptic inputs. *Science* **335,** 353–356.

Tanaka J-I, Horiike Y, Matsuzaki M, Miyazaki T, Ellis-Davies GCR & Kasai H (2008). Protein synthesis and neurotrophin-dependent structural plasticity of single dendritic spines. *Science* **319,** 1683–1687.

Teles-Grilo Ruivo LM & Mellor JR (2013). Cholinergic modulation of hippocampal network function. *Front Synaptic Neurosci* **5,** 2.

Thomson AM & Bannister AP (1998). Postsynaptic pyramidal target selection by descending layer III pyramidal axons: dual intracellular recordings and biocytin filling in slices of rat neocortex. *Neuroscience* **84,** 669–683.

Tønnesen J, Katona G, Rózsa B & Nägerl UV (2014). Spine neck plasticity regulates compartmentalization of synapses. *Nat Neurosci* **17,** 678–685.

Tottene A, Volsen S & Pietrobon D (2000). alpha(1E) subunits form the pore of three cerebellar R-type calcium channels with different pharmacological and permeation properties. *J Neurosci Off J Soc Neurosci* **20,** 171–178.

Traynelis SF, Wollmuth LP, McBain CJ, Menniti FS, Vance KM, Ogden KK, Hansen KB, Yuan H, Myers SJ & Dingledine R (2010). Glutamate receptor ion channels: structure, regulation, and function. *Pharmacol Rev* **62,** 405–496.

Truckenbrodt S & Rizzoli SO (2014). Spontaneous vesicle recycling in the synaptic bouton. *Front Cell Neurosci*; DOI: 10.3389/fncel.2014.00409.

Tsien RY (1983). Intracellular measurements of ion activities. *Annu Rev Biophys Bioeng* **12,** 91–116.

Turrigiano G (2012). Homeostatic Synaptic Plasticity: Local and Global Mechanisms for Stabilizing Neuronal Function. *Cold Spring Harb Perspect Biol* **4,** a005736.

Turrigiano GG (2008). The self-tuning neuron: synaptic scaling of excitatory synapses. *Cell* **135,** 422–435.

Turrigiano GG, Leslie KR, Desai NS, Rutherford LC & Nelson SB (1998). Activity-dependent scaling of quantal amplitude in neocortical neurons. *Nature* **391,** 892–896.

Usai C, Barberis A, Moccagatta L & Marchetti C (1999). Pathways of cadmium influx in mammalian neurons. *J Neurochem* **72,** 2154–2161.

Vacher H, Mohapatra DP & Trimmer JS (2008). Localization and Targeting of Voltage-Gated Ion Channels in Mammalian Central Neurons. *Physiol Rev* **88,** 1407–1447.

Volianskis A, France G, Jensen MS, Bortolotto ZA, Jane DE & Collingridge GL (2015). Long-term potentiation and the role of N-methyl-D-aspartate receptors. *Brain Res* **1621,** 5–16.

Weber JP, Andrásfalvy BK, Polito M, Magó Á, Ujfalussy BB & Makara JK (2016). Location-dependent synaptic plasticity rules by dendritic spine cooperativity. *Nat Commun* **7,** ncomms11380.

Westenbroek RE, Sakurai T, Elliott EM, Hell JW, Starr TV, Snutch TP & Catterall WA (1995). Immunochemical identification and subcellular distribution of the alpha 1A subunits of brain calcium channels. *J Neurosci Off J Soc Neurosci* **15,** 6403–6418.

Williams SR & Mitchell SJ (2008). Direct measurement of somatic voltage clamp errors in central neurons. *Nat Neurosci* **11,** 790–798.

Williams SR & Stuart GJ (2002). Dependence of EPSP efficacy on synapse location in neocortical pyramidal neurons. *Science* **295,** 1907–1910.

Williams SR & Wozny C (2011). Errors in the measurement of voltage-activated ion channels in cell-attached patch-clamp recordings. *Nat Commun* **2,** 242.

Williams SR, Wozny C & Mitchell SJ (2007). The back and forth of dendritic plasticity. *Neuron* **56,** 947–953.

Wolfart J & Roeper J (2002). Selective coupling of T-type calcium channels to SK potassium channels prevents intrinsic bursting in dopaminergic midbrain neurons. *J Neurosci Off J Soc Neurosci* **22,** 3404–3413.

Yang S, Tang C-M & Yang S (2015). The Shaping of Two Distinct Dendritic Spikes by A-Type Voltage-Gated K+ Channels. *Front Cell Neurosci*; DOI: 10.3389/fncel.2015.00469.

Yasuda R, Sabatini BL & Svoboda K (2003). Plasticity of calcium channels in dendritic spines. *Nat Neurosci* **6,** 948–955.

Yuste R (2011). Dendritic spines and distributed circuits. *Neuron* **71,** 772–781.

Yuste R & Denk W (1995). Dendritic spines as basic functional units of neuronal integration. *Nature* **375,** 682–684.

Yuste R, Majewska A, Cash SS & Denk W (1999). Mechanisms of calcium influx into hippocampal spines: heterogeneity among spines, coincidence detection by NMDA receptors, and optical quantal analysis. *J Neurosci Off J Soc Neurosci* **19,** 1976–1987.

Acknowledgements

Through some of the more challenging phases of the years it has taken me to carry out this work, I have relied, more than anyone else, on the support of Anita Smarandache. Without her constant love and companionship, I doubt I would have found the strength to bring this thesis to completion. During my time in Göttingen I have forged new friendships with people who it has been a privilege to know. All of them have added colour to this challenging experience – whether through daily life in the lab, excursions into the wilder parts of this country or stress-busting evenings with games. These are memories I will cherish well into the future. Among these friends, I count my colleagues Ankit Awasthi and Markus Stahlberg. Both are talented scientists from whom I have gained much with regular journal clubs and general support in the lab.

Michael Siebrecht and Dr Guobin Bao are true experts in all things Matlab. Both these individuals have contributed immensely in helping me develop useful tools for the analysis of spine calcium transients. Both have been patient and readily available sources of help. I am particular grateful towards Dr Guobin Bao who assisted me in adapting my algorithm to tackle major parts of this thesis. I also want to thank Dr Oliver Schlüter and his lab members for material support and insightful discussions on various topics related to my thesis.

Finally, I would like to thank Dr Camin Dean who supervised me for the duration of my doctoral studies. Despite numerous errors I made along the way, she has continued to support my efforts to seek a doctoral degree. I am also thankful towards Gertrud Reemtsma Foundation for their generous financial support.

Abbreviations

AARG	Activity-based automatic ROI generation
AMPAR	α-amino-3-hydroxy-5-methyl-4-isoxazolepropionic acid receptors
AP5	D-(-)-2-Amino-5-phosphonopentanoic acid
bAP	Backpropagating action potential
BDNF	Brain-derived neurotrophic factor
CICR	Calcium-induced calcium release
CNS	Central nervous system
EPSC	Excitatory postsynaptic current
GABA	γ-aminobutyric acid
GIRK	G-protein coupled inwardly rectifying potassium (channel)
GluA	AMPAR subunit
IPSC	Inhibitory postsynaptic current
mEPSC	Miniature excitatory postsynaptic current
mGluR	Metabotropic glutamate receptor
NMDAR	N-methyl-D-aspartate receptor
NR	NMDAR subunit
PSD-95	Postsynaptic density (protein) 95
p75	Pan neurotrophin receptor 75
rBDNF	Recombinant brain-derived neurotrophic factor
ROI	Region of interest
SLM	Stratum lacunosum-moleculare
SM	Sec1/munc18-like proteins
SNARE	Soluble NSF attachment receptor proteins
SR	Stratum radiatum
SSCT	Spontaneous synaptic calcium transient
SV	Synaptic vesicle
TrkB	Tyrosine kinase B receptor
TTX	Tetrodotoxin
tSSCT	Suprathreshold spontaneous synaptic calcium transient
VGCC	Voltage-gated calcium channel
VGSC	Voltage-gated sodium channel